Lateral heterostructures, alloys, and the Kirkendall effect in transition metal dichalcogenide monolayers

DISSERTATION
zu Erlangung des Grades eines Doktors
der Naturwissenschaften

vorgelegt von
M.Sc. Kai Mehlich

eingereicht bei der Naturwissenschaftlich-Technischen Fakultät
der Universität Siegen
Siegen 2026

Betreuer und erster Gutachter
Prof. Dr. rer. nat. Carsten Busse
Universität Siegen

Zweiter Gutachter
Prof. Dr. rer. nat. Thomas Michely
Universität zu Köln

Tag der mündlichen Prüfung
09. Juli 2026

Abstract

This dissertation analyzes two-dimensional structures and effects involving Mo, Ta, and S on Au(111), using scanning tunneling microscopy (STM). The structures presented include monolayer dislocation-free concentric lateral heterostructures (CLHs) between MoS_2 and TaS_2, alloys and a kagome structure. All of these are created utilizing epitaxial growth methods, including a mix of physical vapor and chemical vapor deposition. Physical vapor deposition supplies the transition metals Ta and Mo, and chemical vapor deposition using H_2S, supplies the S components. By fine tuning of the growth parameters the differing structures could be realized with precision and consistency.

The analyzed CLHs consist of a core of MoS_2 and a surrounding envelope of TaS_2, which represents a Schottky contact with maximally reduced dimensionality in the z-direction. Structures of this kind are of great interest as model systems for device manufacturing with reduced dimensionalities. While a growth process was already established in previous works, the nature of the interconnection of these two materials, which exhibit a lattice constant mismatch of $\sim$4.5 %, was left unresolved. This thesis shows that each CLHs presents two types of dislocation-free interfaces, compensating lattice constant mismatch not via dislocations but interface-type dependent deformations. The interface types have been identified from the perviously unknown stacking registries of the CLH with the substrate. These were determined from the distribution of the orientations of CLHs within the hcp- and fcc-stacked areas of the Au(111) substrate, in comparison to free-standing islands of MoS_2. Additionally, the edge terminations of the CLHs could be determined from these results. The majority of the deformation was shown to accumulate in the TaS_2 envelope. This envelope contracted in both interfaces to match the MoS_2 core, which only showed little expansion. In one interface a relaxation of the envelope lattice constant with distance to the interface was observed. Notably, with significant distance, even an extension beyond the equilibrium lattice constant was detected. Empirical potentials and finite elements simulations were performed, showing that most of the effects were explainable by simple mechanics.

Modifying the growth process, originally designed to grow CLHs, $Mo_{(1-x)}Ta_xS_2$ alloys were observed. The dependence of alloy formation on the new growth parameters has been analyzed and, utilizing a combination of analysis methods, the ranges of mixtures inside alloys with different growth parameters were estimated.

A continuous change from CLHs to alloys with increase in annealing temperature has been found. The investigation of these alloys was further expanded upon by the alteration of the growth process, resulting in the observation of additional structures and variations.

Another new structure was discovered as a byproduct of various growth processes. A structure crystallizing in the distinctive kagome lattice, aptly called kagome structure. Topography analysis was used to calculate a first estimation of the lattice constant of the structure. Additionally, a synthesization method to grow large areas of the material was developed.

Lastly, Kirkendall holes, the 2D equivalent of the 3D Kirkendall voids, were discovered as a result of the Kirkendall effect. The detection took place after a special growth process which resulted in the formation of $Mo_{(1-x)}Ta_xS_2$ alloys with gradual rates of mixture. Local changes of alloy lattice constants and coverages rates of holes and alloys, in comparison to CLHs, were used to analyze the resulting structures. A model of the growth process was proposed with the help of DFT calculations and a Monte Carlo simulation, showing that the Kirkendall effect can be transferred from 3D to 2D applications.

Kurzzusammenfassung

In dieser Dissertation werden zweidimensionale Materialien und Effekte mit Mo, Ta und S auf Au(111)-Oberflächen behandelt. Das Hauptinstrument zur Untersuchung ist dabei das Rastertunnelmikroskop. Zu den hier betrachteten Strukturen und Phänomenen zählen konzentrisch-laterale Heterostrukturen (KLH) zwischen MoS_2 und TaS_2, deren Schnittstellen fehlstellenfrei sind, Legierungen, der Kirkendall Effekt im zweidimensionalen Raum und eine Kagome-Struktur. Alle dabei erzeugten Materialien wurden mit epitaktischen Wachstumsmethoden hergestellt. Hierzu wurde eine Mischung aus physikalischer und chemischer Gasphasenabscheidung verwendet. Die Übergangsmetalle Mo und Ta wurden dabei durch physikalische Gasphasenabscheidung zur Verfügung gestellt, während chemische Gasphasenabscheidung, unter Verwendung von H_2S-Gas den Schwefel bereitstellte. Durch präzises Einstellen der Wachstumsparameter konnten die verschiedenen Strukturen und Materialien mit großer Genauigkeit und Wiederholbarkeit erzeugt werden.

Die betrachteten KLH bestehen aus einem Kern aus MoS_2, welcher von einer Schale aus TaS_2 umgeben ist. Sie stellen dabei einen Schottky-Kontakt mit minimaler Ausdehnung in z-Richtung dar und sind deshalb von großem Interesse als Modellsystem für die Herstellung von industriellen Mikrostrukturen. Während ein Wachstumsprozess bereits etabliert war, blieb die Natur der Schnittstelle beider Materialien, welche eine Fehlpaarung von $\sim$4.5 % aufweisen, bisher ungeklärt. Es konnte gezeigt werden, dass zwei Arten fehlstellenfreier Schnittstellen innerhalb der KLH vorhanden sind und jegliche Fehlpaarungen durch schnittstellenabhängige Deformationen ausgeglichen werden. Die Fehlstellenarten konnten durch bisher unbekannte Stapelregister der KLH mit dem Substrat bestimmt werden. Diese wurden aus Vergleichen von Verteilungsanalysen der Orientierungen der KLHs und von freistehenden MoS_2-Inseln, innerhalb der hdp- und kfz-Domänen der Au(111)-Oberfläche hergeleitet. Dadurch konnten auch die Kantenterminierungen der KLH bestimmt werden. Die große Mehrheit der Deformation besteht dabei aus einem Zusammenziehen der TaS_2-Schale, während sich der MoS_2-Kern nur leicht ausdehnt. Während das Zusammenziehen der TaS_2-Schale Schnittstellenunabhängig beobachtet wurde, konnte an einer der beiden Schnittstellen eine Relaxion mit zunehmder Distanz beobachtet werden. Diese fand nicht nur bis zur Equilibriumsgitterkonstante statt, sondern auch über diese hinaus. Simulationen mittels finiter Elemente und periodischer Poten-

tiale konnten zeigen, dass das Deformationsverhalten grundsätzlich auf einfache Mechanik zurzuführen ist.

Durch Modifikation des Wachstumsprozesses für KLHs konnten Legierungen mit der Strukturformel $Mo_xTa_{(1-x)}S_2$ nachgewiesen werden. Die Abhängigkeit des Legierungswachstums von den Wachstumsparametern wurde untersucht und durch unterschiedliche Analysemethoden wurden die Mischungsverhältnisse bei diesen Parametern bestimmt. Ein kontiniuerlicher Übergang von KLH zu Legierung konnte mit steigender Wachstumstemperatur festgestellt werden. Nähere Untersuchungen, durch weitere Anpassung des Wachstumsprozesses, resultierten im Wachstum zusätzlicher Strukturen.

Ein Nebenprodukt diverser Wachstumsprozesse ist die Kagome-Struktur, benannt nach ihrer charakteristischen Gitterstruktur, dem Kagome-Gitter. Mittels topographischer Analysemethoden, konnte auch hier eine erste Gitterkonstante bestimmt werden. Auch eine Preparationsmethode für großflächige Kagome-Bedeckung wurde erfolgreich entwickelt.

Schlussendlich wurden, als Produkt des Kirkendall Effektes in 2D Materialen, Kirkendall-Löcher beobachtet. Diese zeichnen sich ebenfalls durch ihre reduzierte Dimensionalität aus. Entdeckt wurde dieser Effekt während eines alternativen Wachstumsprozesses zum herstellen von $Mo_xTa_{(1-x)}S_2$-Legierungen, welche ein graduelles Mischungsverältnis aufweisen. Diese Mischungsverhältnisse wurden durch Analyse der zugehörigen Gitterkonstanten und der Oberflächenbedeckungen, im Vergleich zu KLHs, bestimmt. Mithilfe von DFT-Berechnungen und einer Monte-Carlo Simulation konnte ein Wachstumsmodell für die Kirkendall-Löcher erstellt werden.

CONTENTS

1 Introduction **11**

2 Theoretical Background **13**

2.1 Scanning Tunneling Microscopy 13

2.1.1 Experimental Setup 13

2.1.2 Tunnel effect 16

2.2 Miller Indices 19

2.3 Au Single Crystal and Au(111) Surface 20

2.3.1 Crystal Structure and FCC(111) Stacking 21

2.3.2 Au(111) Surface Reconstruction 22

2.3.3 Steps in the Surface 24

2.4 Mismatch 25

2.4.1 Definition of Mismatch 25

2.5 Monolayer Transition Metal Dichalcogenides 28

2.5.1 General Description 28

2.5.2 TMDC Unit Cell and Lattice Constant 30

2.5.3 Stacking Registry of TMDCs on FCC- and HCP-Stacked Substrates 32

2.6 Transition Metal Dichalcogenide Heterostructures 34

2.6.1 Lateral Heterostructures and Concentric Lateral Heterostructures 34

2.6.2 Stacking Registries 37

2.7 Moiré Pattern 40

2.7.1 Hexagonal Patterns 43

2.7.2 Classical moiré formula 44

2.8 Kirkendall Effect 45

2.8.1 Kirkendall Voids 46

3 Prerequisites **47**
3.1 Variable Temperature UHV System TUMA III 47
3.2 Cyclical Preparation Process 49
3.3 Distortion Correction 51
3.3.1 Affine Distortion 51
3.4 Monte Carlo Simulation 53
3.4.1 Choice of Vacancy 53
3.4.2 Movement of the Vacancy 55
3.4.3 Periodic boundary conditions 56
3.5 Finite Elements and Empirical Potentials Simulation 59
3.5.1 Finite Elements Simulations 59
3.5.2 Empirical Potentials Simulations 61

4 Results and Discussion **63**
4.1 MoS_2-TaS_2 Concentric Lateral Heterostructures 63
4.1.1 Preparation and Resulting Structures 63
4.1.2 Interface Analysis by Orientation and Distribution of Islands 67
4.1.3 Interconnection at the Interface 71
4.1.4 Lattice Constant of TaS_2/Au(111) 75
4.1.5 Deformation Simulations 76
4.1.6 Conclusion 79
4.2 $Mo_{(1-x)}Ta_xS_2$ alloys 80
4.2.1 Preparation and Resulting Structures 80
4.2.2 Structure of the $Mo_{(1-x)}Ta_xS_2$ Alloy 84
4.2.3 Alternative Growth Process 91
4.2.4 Structural Analysis 95
4.2.5 Conclusion 100

4.3 Kirkendall Holes in Two-Dimensional $Mo_{(1-x)}Ta_xS_2$ Alloys 102
4.3.1 Preparation and Resulting Structures 102
4.3.2 Moiré Analysis 105
4.3.3 Surface Coverage 107
4.3.4 Theoretical Analysis and Proposed Model Growth Process . 111
4.3.5 Monte Carlo Simulation 116
4.3.6 Conclusion 120
4.4 Kagome Lattice 121
4.4.1 Preparation and Resulting Structures 121
4.4.2 Structure and Analysis 123
4.4.3 Conclusion 124

5 Summary **125**

6 Outlook **129**

7 Appendix **131**

8 Aknowledgements **173**

List of Abbreviations

2D	Two Dimensional
CLH	Concentric Lateral Heterostructure
CU	Copper
DFT	Density Functional Theory
FCC	Face-Centered Cubic
HCP	Hexagonal Close Packed
ML	Monolayer
MO	Molybdenum
RT	Room Temperature
S	Sulfur
SPM	Scanning Probe Microscopy
STM	Scanning Tunneling Microscopy/Scanning Tunneling Microscope
TA	Tantalum
TMDC	Transition Metal Dichalcogenide
UHV	Ultra-High Vacuum
ZN	Zinc

CHAPTER 1

INTRODUCTION

Since the advent of graphene, due to the work of Novoselov and Geim [1], two-dimensional (2D) materials have grown into a wide field of research, which has branched into many more types of materials [2]. One of these emergent groups are monolayer transition metal dichalcogenides (TMDCs).

TMDCs follow the general formula of MX_2, containing one metal atom (M) and two chalcogenes (X_2) in their unit cell [3]. Depending on these chalcogenes and metals, they vary in structure, electronic, and optical properties [4, 5, 6]. The fact that these are monolayer versions of their stacked counterparts reduces the degrees of freedom to two dimensions and often sets their properties apart from their three dimensional cousins [7]. Their maximally reduced size and rich landscape of characteristics opens up the opportunity for monolayer TMDCs to be part of micro- and nanoscale device manufacturing processes, where space optimization plays an ever more important role in the prospects of pushing the boundaries of Moore's law [8, 9]. It is therefore of great importance to understand the growth processes and structural morphologies of these materials to enable them to become reliable building blocks in any designers vision. As complex devices tend to consist of many materials working in unison, a foundational building block is the combination of two materials. Doing so in-plane preserves the reduced height which makes monolayer TMDCs special.

An insightful example of such a combination is the growth of concentric lateral heterostructures (CLHs), which are in-plane heterostructures containing one TMDC in the center and another surrounding it. From these combinations further changes in electronic properties can arise [10]. Moreover TMDCs and therefore CLHs of sufficiently small size (< 15 nm of diameter) can be categorized as quantum dots, as additional in-plane confinement is applied to the materials, further enhancing electronic band structure, resulting in atom-like states [11, 12, 13]. CLHs with MoS_2 and TaS_2, as presented in this thesis, already constitute a Schot-

tky contact due to the metallic and semiconducting nature of their constituents [14, 15]. This dissertation discusses results, such as the, hitherto unknown, nature of the interfaces connecting the two materials, their mismatch compensation mechanisms, their preferred stacking registries with the chosen substrate, as well as their edge terminations. Knowledge of these quantities is essential for implementation in more complex systems and gives insight in the foundational processes possible for different classes CLHs.

Literature has already established that, depending on growth parameters such as temperature, the types of resulting materials and their morphology can vary dramatically [16, 17, 18]. This included the prediction of monolayer alloys between MoS_2 and TaS_2 [19]. Alloys are known to exhibit electronic, and structural properties of their own, which can differ significantly from non-alloyed TMDCs and therefore extend the possibility for manufacturing processes further [20, 21, 22]. This dissertation shows methods for synthesization of these predicted alloys and investigates their growth parameter dependency. A continuous change from CLHs to alloys has been achieved, resulting in the ability to engineer desired solutions while also analyzing structural information of the respective materials.

These studies also unveiled new structures including a monolayer material crystallizing in the kagome lattice and Kirkendall holes, as the 2D equivalent of the 3D Kirkendall voids. A growth model for these Kirkendall holes was proposed with the support DFT calculations and a Monte Carlo simulation, shedding further light on the growth processes of 2D alloys.

The thesis is divided into seven chapters. The chapter *Theoretical Background* explains the theoretical background of the instruments, materials, and physical effects involved to describe the results. This is followed by the chapter *Prerequisites*, containing a description of the experimental setup and its usage to perform the growth processes in this thesis. Additionally measures taken to evaluate and calibrate results are discussed, as well as the fundamentals of the simulations presented in this dissertation are shown. In *Results and Discussions* the results of the various experiments are shown, analyzed and contextualized. This includes CLHs, alloys, Kirkendall holes, the kagome lattice and other structures. At the end a *Summary* and an *Outlook* chapter can be found, followed by an *Appendix* with additional information.

CHAPTER 2

THEORETICAL BACKGROUND

2.1 Scanning Tunneling Microscopy

Scanning tunneling microscopy (STM) is a measurement technique in the family of scanning probe microscopies (SPMs) and is the main technique utilized for imaging in this thesis. Originally invented by Gerd Binnig and Heinrich Rohrer in 1982 [23], their work awarded them the Nobel Prize in Physics in 1986 [24]. The following sections give a brief overview of experimental setups and explain the quantum mechanics enabling the system to measure data.

2.1.1 Experimental Setup

As all Scanning Probe Microscopy techniques, STM uses a tip moving over a surface to acquire data. To facilitate this process several components are necessary as illustrated in figure 2.1.

Firstly, the tip needs to be able to move, which is accomplished by connecting it to a set of piezo-units, which in turn are connected to a control unit. By utilizing several piezo-units at once, movement in the x-y- and z-direction can be accomplished.

A bias voltage is applied between the tip and the sample, leading to the flow of a current between the two, due to the quantum mechanical tunneling effect (see subsection 2.1.2). This current is amplified by a current amplifier, changed to a voltage signal and send to the control unit. As the current depends on the distance to the sample, the control unit can be used to set the tip to a desired height relative to the sample. A setup like this can generally be used in two modes

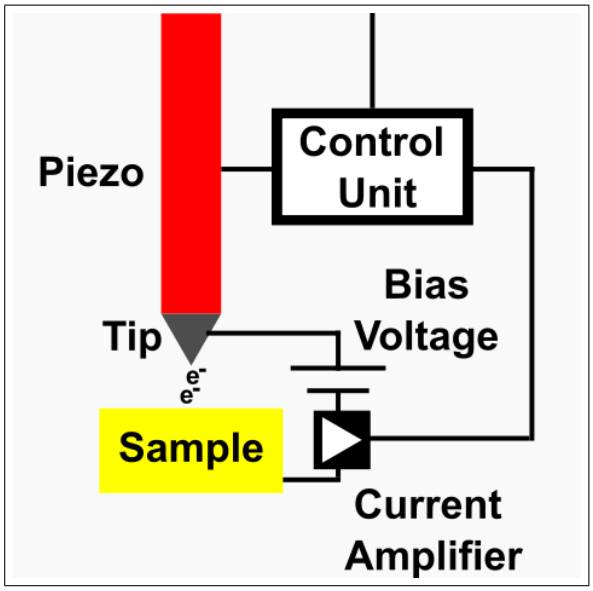


Figure 2.1: Schematics of a scanning tunneling microscope, wherein a tip is brought in close proximity with a conductive sample. A bias voltage is applied causing a tunneling current, which is amplified by a current amplifier to be processed for tip movement by a control unit.

of operation, known as constant current mode and constant height mode [25]. In constant height mode, the tip of the STM is fixed to a certain height z and scans over the surface. Due to the possible height and material differences exhibited by the sample, the resulting distance to the tip, and therefore the current, will vary. The current variation is then evaluated as image data. This is a quick and easy way to operate an STM, as no complex regulatory circuit is necessary. However if protrusions on the surface are higher than the set distance, the tip might collide with them, resulting in damage to the tip.

The other mode of operation is the constant current mode. Here the goal is to keep the amount of current flowing through the tip constant by use of the regulatory circuit. Whenever a change in current is detected, the regulatory circuit will increase or decrease the height of the tip to mitigate this change. The resulting changes in height, necessary to keep the current constant, can then be evaluated as data to create an STM image. This process, however, might need a lot of fine tuning and depending on the speed of the components, might also necessitate a slower process of measurement. All measurements in this thesis have taken place in constant-current mode. Illustrations of these two techniques can be seen in figure 2.2 a) and b), respectively.

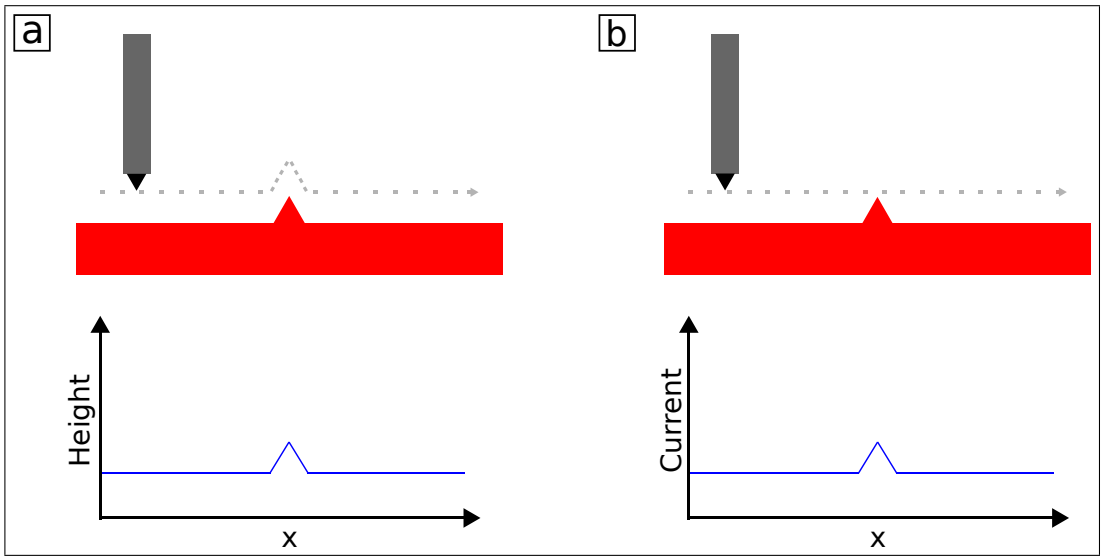


Figure 2.2: Scanning modes in STM: a) constant current mode; b) constant height mode. Modified from [26].

2.1.2 Tunnel effect

As mentioned before, data acquisition is based on the flow of a current between the sample and the tip. This current is possible due to the quantum mechanical tunneling effect. The following description will give a short summary based on [27]. The behavior of the an electron in a potential is known to be described by the Schrödinger equation

$$i\hbar\frac{\partial}{\partial t}\psi(x,t) = \left[-\frac{\hbar^2}{2m}\frac{\partial^2}{\partial x^2} + V(x,t)\right]\psi(x,t), \quad [28] \tag{2.1}$$

which simplifies for time independent approaches to

$$-\frac{\hbar^2}{2m}\frac{\partial^2}{\partial x^2}\psi(x) + V(x)\psi(x) = E\psi(x). \quad [29] \tag{2.2}$$

Solutions of the equations show that the probability density $\psi^*\psi$ of an electron at fermi energy in the tip extends even beyond the discontinuity of the potential environment representing the end of the tip, resulting in a chance to find the electron outside of it. A situation that would be forbidden for particles according to classical mechanics. Outside of the tip, this probability density decays exponentially at a rate of

$$e^{-\kappa x}, \tag{2.3}$$

with

$$\kappa \cong \sqrt{2m\phi/\hbar^2}. \tag{2.4}$$

The rate at which tunneling occurs is directly proportional to this exponential decay in the classically forbidden region. Not all potential environments for the Schrödinger equation have analytical solutions, yet most cases can be reasonably described by the Wentzel-Kramers-Brillouin approximation. Given a probability current of

$$j = \frac{i\hbar}{2m}(\psi\frac{\partial\psi^*}{\partial x} - \psi^*\frac{\partial\psi}{\partial x}), \tag{2.5}$$

the fraction $\hbar k/m$ from an incident wave e^{ikx}, which then passes through a barrier $V(x) > E_{\mathrm{x}}$ to the classically forbidden area is defined as

$$D = e^{-2K}, \tag{2.6}$$

with

$$K = \int_{x_1(E_x)}^{x_2(E_x)} \kappa(x, E_x), \tag{2.7}$$

and

$$\kappa(x, E_x) = \sqrt{\frac{2m^*(V(x) - E_x)}{\hbar^2}}. \tag{2.8}$$

Here m^* denotes the electron mass, V(x) the potential energy, E_x the kinetic energy of the electron, and x_1 and x_2 the classical turning points of the potential.

Bardeen Theory of Tunneling

To more fully describe the tunneling current between two electrodes the Bardeen Theory of Tunneling can be used. This summary is based on [30]. Here the tunneling current is given as

$$I = \frac{4\pi e}{\hbar} \int_{-\infty}^{\infty} [f(E_F - eV + \epsilon) - f(E_F - \epsilon)] \times \rho_A(E_F - eV + \epsilon)\rho_B(E_F + \epsilon)|M|^2 d\epsilon \tag{2.9}$$

with the Fermi distribution function

$$f(E) = \frac{1}{1 + e^{\frac{E - E_F}{k_B T}}} \tag{2.10}$$

and the elements of the tunneling matrix given as

$$M_{\mu\nu} = \frac{\hbar^2}{2m} \int_{z=z_0} \left[\psi_\mu \frac{\partial \chi_\nu^*}{\partial z} - \chi_\nu^* \frac{\partial \psi_\mu}{\partial z} \right] dxdy \tag{2.11}$$

Additionally ρ_A and ρ_B describe the density of states of electrode A and B, respectively. The tunneling current is given by V and ϵ the energy. For low voltages this simplifies to

$$I = \frac{4\pi e}{\hbar} \int_0^{eV} \rho_A(E_F - eV + \epsilon)\rho_B(E_F - \epsilon)|M|^2 d\epsilon. \tag{2.12}$$

If the tunneling matrix also does not change significantly in the investigated energy interval, the equation further simplifies to be dominated by the convolution of the DOS of the two electrodes as

$$I \propto \int_0^{eV} \rho_A(E_F - eV - \epsilon)\rho_B(E_F - \epsilon) d\epsilon \tag{2.13}$$

Uneven Junction - General Case in STM

If a bias voltage is applied between two electrodes (e.g. sample and tip) the occupied states shift unevenly, causing an asymmetric junction, as can be seen in figure 2.3, where a negative voltage is applied, resulting in a current flow from the sample to the tip. This extended description is based on [31]. Taking the shifted

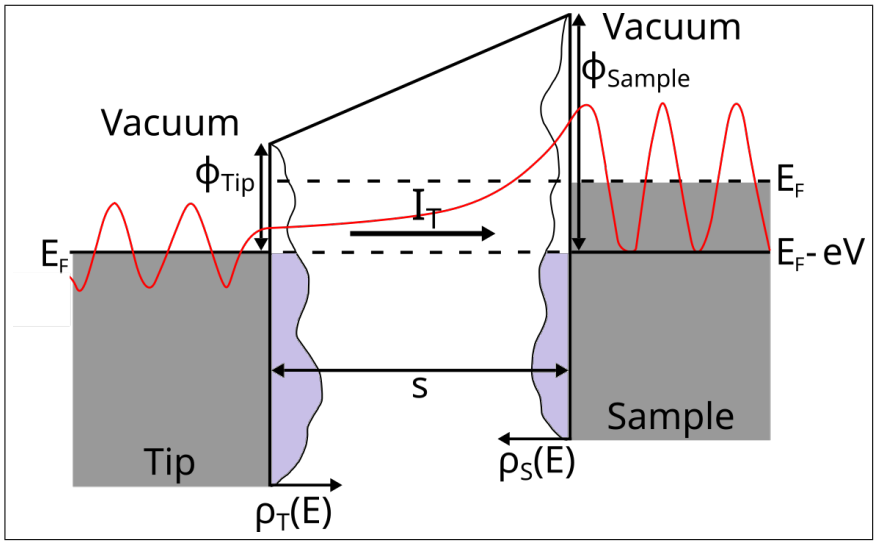


Figure 2.3: Asymmetric junction between STM tip and and sample. Due to a negative bias voltage, electrons tunnel predominantly from the sample to the tip.

energy levels into account, together with the fact that at higher bias voltages the tunneling matrix should not be assumed to be constant but energy dependent, as

$$M_{\mu\nu} = \left[\frac{\hbar^2}{2m}\int_{z=z_0} 2\kappa_\mu \psi_\mu(0)\chi_\nu(s)dxdy\right] e^{-\kappa_\mu s} = M(0)e^{\frac{\kappa_0 \epsilon s}{2\overline{\phi}}}, \tag{2.14}$$

a general more general form for the tunneling current between a tip and a sample can be approximated as

$$I = \int_{-\frac{1}{2}eV}^{\frac{1}{2}eV} \rho_{\text{Tip}}(E_\text{F} + \frac{1}{2}eV - \epsilon)\rho_{\text{Sample}}(E_\text{F} - \frac{1}{2}eV - \epsilon)|M(0)|^2 e^{\kappa_0 \epsilon s/\overline{\phi}} d\epsilon, \tag{2.15}$$

with

$$\kappa_0 = \frac{\sqrt{2m\overline{\phi}}}{\hbar}, \tag{2.16}$$

and

$$\overline{\phi} = \frac{\phi_{\text{Tip}} - \phi_{\text{Sample}}}{2}. \tag{2.17}$$

2.2 Miller Indices

To fully characterize the structure of the Au(111) surface utilized in this thesis, a foundational understanding of Miller indices is necessary and a short introduction shall be given in the following section based on [32].

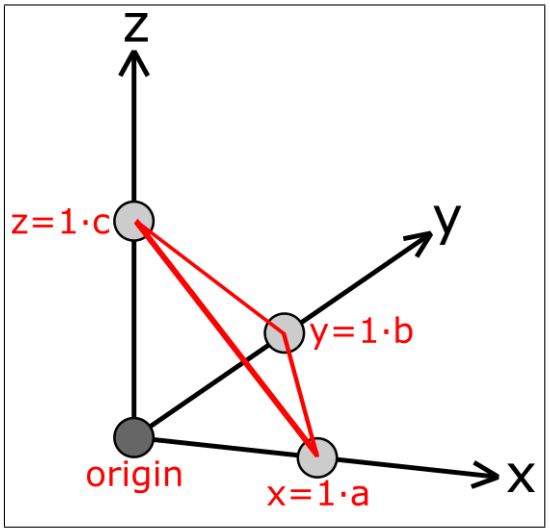


Figure 2.4: Simple three dimensional coordinate system with marked point of origin, as well as the points on x = a, y = b, and z = c where the respective axes are crossed by an arbitrary plane.

Miller indices are a way of describing planes and directions in crystal structures proposed by William Hallowes Miller [33]. Descriptions exist of cubic, hexagonal and rhombohedral structures. As only the cubic description is utilized in this thesis, the following summary is reduced to its explanation.

To describe a cubic crystal plane in Miller indices, take a three dimensional coordinate system and then mark all points $M = m \cdot a$, $N = n \cdot b$, $P = p \cdot c$, in which the described plane crosses the three axes in terms of lattice constants a, b and c in the corresponding direction. An example of this is shown in figure 2.4. In the next step the quotients of 1/m, 1/n, 1/p are calculated leading to:

$$(\frac{1}{m}, \frac{1}{n}, \frac{1}{p}). \tag{2.18}$$

As this can result in a set of rational numbers, all numbers are subsequently multiplied by their lowest common denominator r, leading to a set of whole numbers. This results in a description of the planes known as the Miller Indices

$$r \cdot [\frac{1}{m}, \frac{1}{n}, \frac{1}{q}] = (h\,k\,l). \tag{2.19}$$

A special case exists when an axis is not crossed. In that instance it can be assumed that the axis is crossed in infinity, leading to an equation like the following:

$$1 \cdot [\frac{1}{1}, \frac{1}{\infty}, \frac{1}{\infty}] = (1\,0\,0). \tag{2.20}$$

Should an axis be crossed in the origin, the Miller indices cannot be calculated but as a translated plane with the same orientation belongs to the same family of planes, having the same Miller indices, simply shifting the plane or the coordinate system solves this issue. In the case of a cubic crystal system; a set of Miller indices that describe a surface also describe the normal vector of said surface. As opposed to the notation for a surface, which uses "()", this vector can be written with the same indices using "[ ]".

As equal crystallographic surfaces are indistinguishable from each other, these surfaces can be summarized as families. To reference a family of equal surfaces the notation "{}" is used, while a family of directions can be represented using "<>".

2.3 Au Single Crystal and Au(111) Surface

Gold is generally known as a valuable and inert metal of high density (19.3 $\frac{g}{cm^3}$ [34]). It conducts both heat [35] and electricity [36] very well and has a moderately high melting point of 1337.33 K [34], which makes it a useful resource for electronic devices. The reason gold is utilized as a substrate in this thesis, however, is that its surfaces interaction with MoS_2 and TaS_2 is said to be dominated by van der Waals bonds, developing at most weak hybridizations [37, 38, 39, 40]. Moreover, growth of these TMDCs upon its Au(111) surface is proven to be a reliable possibility and conductivity requirements for STM measurements are met [17, 40]. As indicated by the mentioning of the Au(111) surface, not just any gold is used but a gold single crystal. In a single crystal the unit cell repeats in all three dimensions without interruption [41]. This in turn leads to a continuous lattice without grain boundaries and the defects which are associated with them [42]. Therefore single crystals approximate an idealized structure with a very predictable nature, making it the perfect substrate for epitaxial growth studies. This section gives a short description of gold's crystal structure and the stacking order of the single crystals $(1\,1\,1)$ surface, which has been used as a basis for deposition.

2.3.1 Crystal Structure and FCC(111) Stacking

The gold crystal has a face centered cubic (fcc) structure, as seen in figure 2.5 a) on the left, wherein the gold atoms are located on the edges of the cube and on the center of each side. Since the $(1\,1\,1)$ surface will become important later, special attention will be given to it here. First the ideal fcc$(1\,1\,1)$ surface is discussed.

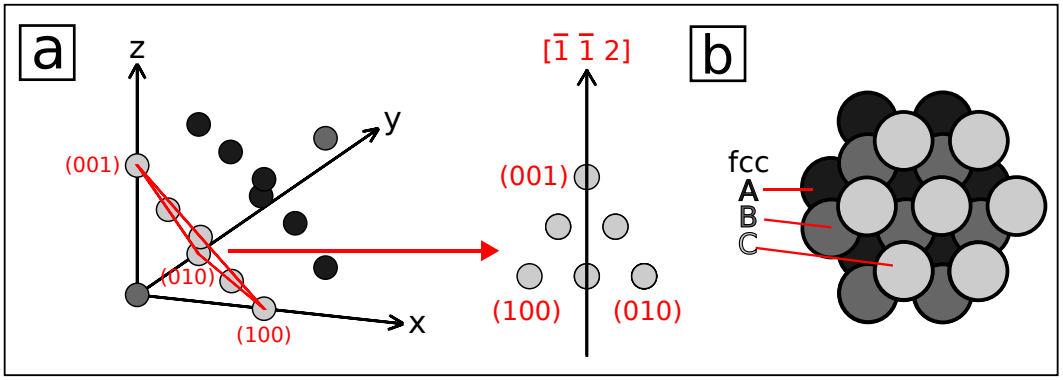


Figure 2.5: Schematics of fcc-stacked single crystal. Atoms of different atomic layers are indicated by varying grayscaled circles: a) Fcc-stacked cube of gold single crystal, with atoms on each edge and the centers of each face of the cube. The (111)-plane is highlighted on the left side and shown on the right side; b) Top view of the (111)-plane with its characteristic ABC-stacking.

Other cases like the Au(111) surface reconstruction have their own dedicated section later on. The unreconstructed surface shall be referenced as fcc(111) and Au$(1\,1\,1)$ will reference a surface with reconstruction. Figure 2.5 a) shows an fcc crystal with the $(1\,1\,1)$ plane marked (left) and separately presented (right). This plane takes the form of a hexagonal 2D-bravais lattice, meaning that the values of the unit cell vector $\vec{a}$ and $\vec{b}$ are the same and the unit cells have an angle of 120° to each other [43].

Figure 2.5 b) shows the stacking order, as seen in $[1\,1\,1]$ direction. This stacking is called fcc stacking and follows an *ABC* structure, meaning that for a pattern of three layers, each subsequent layer lies in the middle of the triangles formed by the atoms of the layer beneath it. Therefore no atom lies on top of an atom of up to two layers beneath it. In this stacking the structure repeats after three layers.

2.3.2 Au(111) Surface Reconstruction

As mentioned before, many crystal surfaces, like Ir(100), Pt(100), Mo(100), and of course Au(111), do not present an idealized surface but experience surface reconstruction [44, 45]. The surface represents a break in symmetry of the crystal, which leads to a lack of bonding partners in z-direction ([1 1 1]-direction for the Au(111) surface), for the atoms of the top layer. Therefore, a reconstruction minimizes the surface energy more effectively [46].

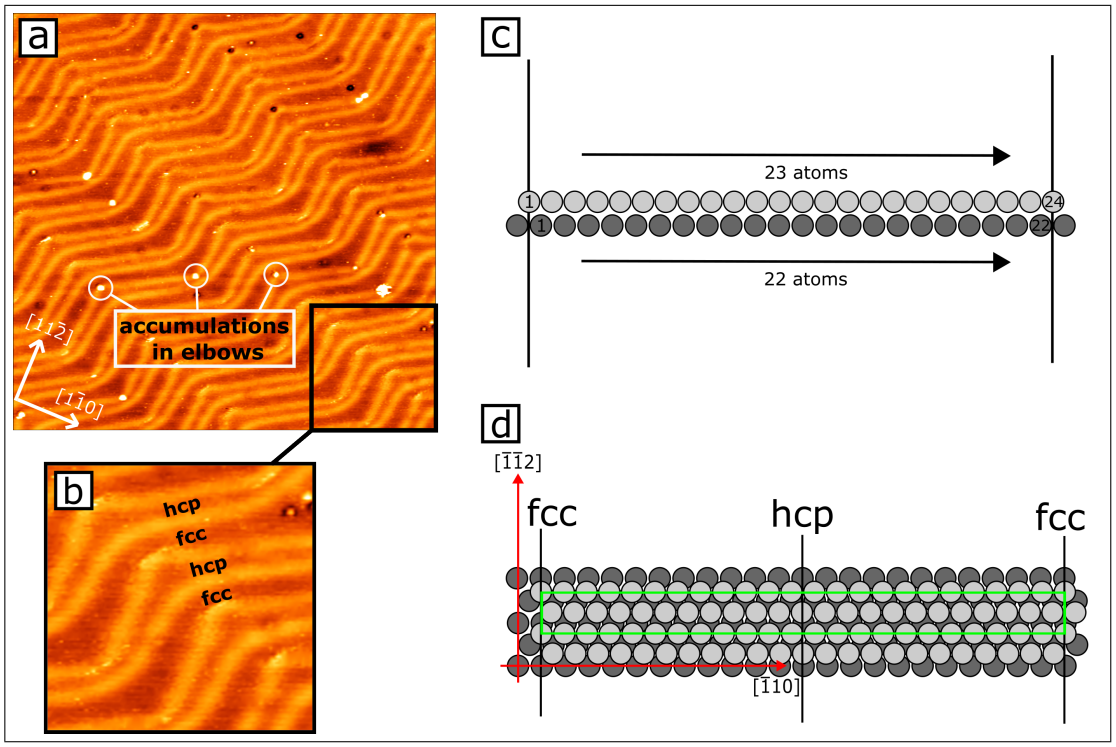


Figure 2.6: a) STM image of herringbone reconstruction on Au(111) surface with highlighted accumulations in the elbows of the herringbone and marked area for *b)*; $U_{\text{bias}} = -0.5$ V, $I = 3 \times 10^{-10}$ A, dimensions: 75 nm × 75 nm, scar corrections applied; b) expanded view of marked area in *a)*, showing the herringbone reconstruction with increased size and labeled areas of fcc and hcp stacking; c) Side view of first and second layer gold atoms in reconstructed Au(111) with 23 atoms in the first layer as opposed to 22 atoms in a same length second layer; d) Top view of situation in *c)* with fcc and hcp stacking marked, as well as the unit cell.

The Au(111) surface reconstruction exhibits a very characteristic wavelike structure and is therefore often called *herringbone reconstruction* (see figure 2.6 a)/b)) [47]. These waves terminate in an extension called *elbows* [47], which are especially reactive points on the Au(111) surface, often acting as nucleation sites [48, 49, 50]. This can be desirable for island growth or accumulate leftover materials from cleaning processes, as can be seen in figure 2.6 a).

Due to the lack of bonding partners above them, the atoms in the top layer move closer together and the space ideally occupied by 22 gold atoms is now occupied by 23 gold atoms [49]. This leads to a $(22 \times \sqrt{3})$-reconstruction on the surface, as seen in 2.6 c) and d). [51, 52, 53]. This 23 atoms periodic shift leads to the formation of fcc and hcp areas in the gold surface [51]. As shown in 2.6 b) the atoms start in line with the fcc stacking, sitting in an up-pointing triangle of the lower layers. This slowly shifts as one moves in the $[\bar{1}\,1\,0]$-direction and after 12 atoms the structure has changed to be in line with an hcp stacking order. This is followed by another slow shift, so that the 12th atom after that is again in line with the fcc stacking order. In $[\bar{1}\,\bar{1}\,2]$-direction the stacking order repeats each third atom. Figure 2.6 b) shows an excerpt from figure 2.6 a), where the resulting areas of fcc and hcp stacking are marked and can be seen in close-up. Generally speaking, the areas inside the herringbones are hcp stacked, while the areas between the herringbones are fcc stacked.

2.3.3 Steps in the Surface

A plane of atoms, which does not completely cover the surface of the plane beneath it, is often called a *terrace*. The ledges formed by the interface of the terrace and its underlayer are referenced as *steps*. To define a step properly, perspective has to be defined first. One can imagine standing on the lower plane and looking at a the edge of the step of the upper plane, so that your sightline is perpendicular to the wall formed by the step in front of you. From this perspective one can now evaluate how the first row of atoms, one can see from the upper plane, sit on the last row of atoms from the lower plane that are visible to you. If fcc stacking is present, this can be done from six directions and two types of steps will emerge, as shown in 2.7 a), labeled *A* and *B*. Step type *A*

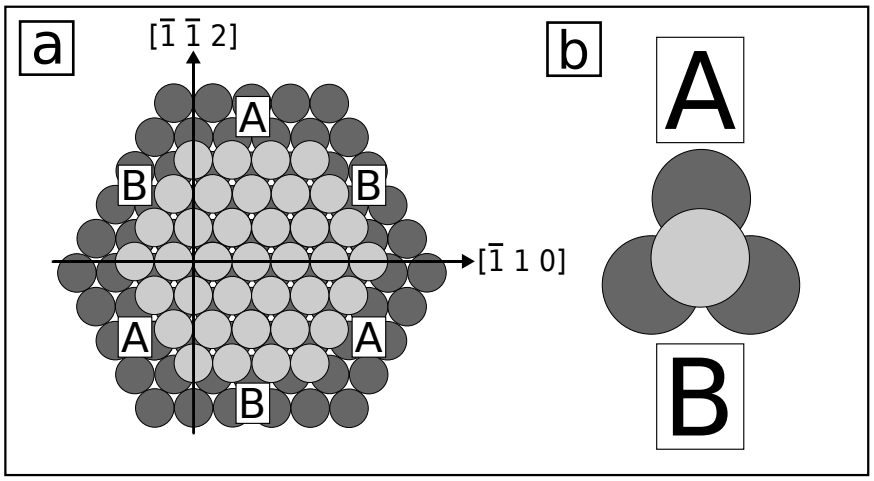


Figure 2.7: a) Two types of steps: *A* and *B*, with the three possible directions they can each point in; b) close up of the stacking structure of the two types of steps on an fcc stacked surface.

is characterized by the atom of the top layer sitting atop just one atom of the lower layer, while step type *B* has one atom of the top layer sitting in between two atoms of the layer underneath, as shown in figure 2.7 b) [54].

2.4 Mismatch

The work with heterostructures expects a knowledge of definitions of mismatch and their compensation. This chapter is going to go into detail about these principles based on the work of [55].

2.4.1 Definition of Mismatch

The definitions developed for substrate-material mismatches of stacked materials can be applied for in-plane heterostructures as well. Here the mismatch is defined as:

$$f = \frac{a_s - a_e}{a_e}. \tag{2.21}$$

In a substrate material interaction a_s represents the relaxed lattice constant of the substrate and a_e the relaxed lattice constant of the surface material. In the case of in-plane heterostructures we set a_s to the relaxed lattice constant of one material and a_e to the relaxed lattice constant of the second material. Alternative definitions are possible by the exchange of a_s and a_e in the numerator and the material chosen for a_s and a_e. In this work we will keep the definition in equation 2.21 and define a_s to be the material with the larger relaxed lattice constant and a_e as the material with the smaller relaxed lattice constant. In substrate-epitaxial layer conditions with low mismatches ($|f| < 1\%$), the initial growth is predicted to be coherent because of the relative thickness of the substrate to the growth layer atop it. A similar situation for in-plane heterostructures would constitute the growth of a thin layer of material around an existing core. Such a deformed layer is known as pseudomorphic. The resulting strain experienced by such a thin layer, be it for a heterostructure or a thin layer atop a substrate, can be defined by the lattice mismatch as

$$\varepsilon_{\parallel} = f \text{ (pseudomorphic)}. \tag{2.22}$$

With increasing thickness of the originally pseudomorphic layer, the strain energy increases until it is not favorable to simply deform the layer anymore. At this stage the introduction of misfit dislocations to relax some of the strain becomes viable. The exact point at which this takes place is called the *critical layer thickness* h_c. Once this has taken place, part of the mismatch is compensated by

the partially relaxed layers as follows:

$$\varepsilon_{\parallel} = f - \delta \text{ (partially relaxed layer).} \tag{2.23}$$

Here δ is the amount of strain reduction caused by the misfit dislocations. The residual strain can be calculated at thermodynamic equilibrium, however, more complex factors exist. These include kinetic barriers to lattice relaxation, which are generally associated with generation, movement and interactions of dislocations. In these situations kinetic models must be applied, which predict residual strain to depend on parameters like mismatch, layer thickness, growth conditions and post-growth thermal cycling.

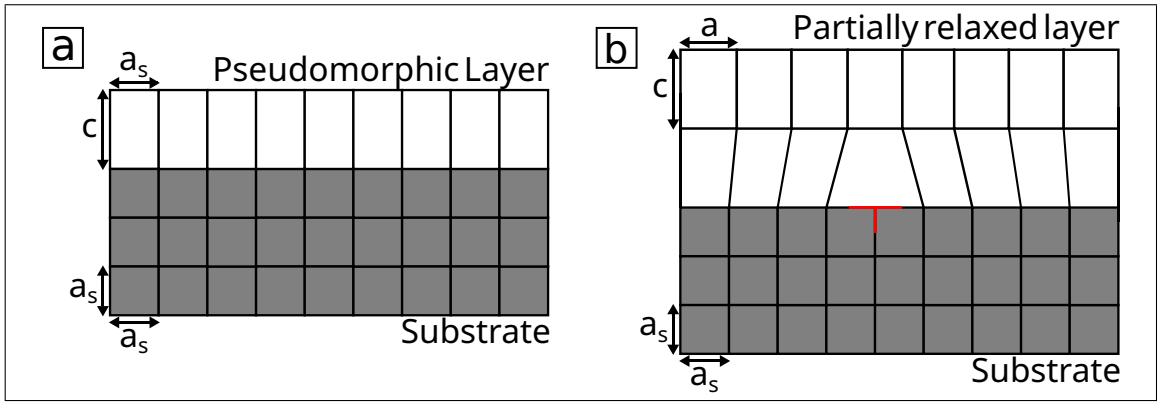


Figure 2.8: a) Representation of a pseudomorphic layer seamlessly connected to a substrate; b) A partially relaxed layer connected to a substrate by misfit dislocation. Image in reference to [56]

Vertical heteroepitaxy assumes that for small mismatches, and a layer by layer growth, the initial growth will be coherently strained to form a seamless connection with the substrate. This can be seen in figure 2.8 a). Here the substrate is assumed to be sufficiently thick in comparison to the added layer and has a cubic lattice with the lattice constant a_s. The epitaxial layer also has a cubic lattice in unstrained form, with a determining lattice constant of a_e. However, its unstrained lattice is bigger than the lattice of the substrate ($a_e > a_s$).

To facilitate a connection, the lattice constant of the epitaxial layer is compressed to a_s in all directions of connection. This leads to biaxial strain according to equation 2.23, with $\delta = 0$ and $\varepsilon_{\parallel} = f$, since no lattice relaxation is present. The out of plane strain $\epsilon_{\perp}$ is given as:

$$\epsilon_{\perp} = -R_B \epsilon_{\parallel} = -\frac{2C_{12}}{C_{11}} \epsilon_{\parallel}. \tag{2.24}$$

R_B is known as the biaxial relaxation constant of the grown epitaxial layer. It can also be expressed through the matrix elements C_{12} and C_{11} of the Cauchy stress tensor. Note that $\epsilon_\perp$ is negative in comparison to $\epsilon_\parallel$. The resulting distortion for the epitaxial layers is tetragonal and leads to a new, out of plane lattice constant c, with $c > a_e$.

When a certain thickness (critical layer thickness) is reached, the strain energy has risen to a point at which it is more favorable to include a misfit dislocation to partially relax the induced strain. The results of this can be seen in figure 2.8 b). Since the introduced defect only partially relaxes the lattice constant, some of the mismatch is still accommodated by strain in the material, therefore the lattice constant of this case is still higher than the lattice constant of the substrate but also lower than a case fully accommodated by strain ($a_e > a > a_s$). Different models exist to calculate the critical layer thickness but as this thesis utilizes computational approaches like DFT and empirical potentials to solve these questions, further details about these models will be omitted here.

2.5 Monolayer Transition Metal Dichalcogenides

The materials discussed in this dissertation belong to the family of transition metal dichalcogenides (TMDCs). This chapter is a short summary of their structure and properties, focusing especially on descriptions applicable to MoS_2 and TaS_2.

2.5.1 General Description

TMDCs follow the general formula MX_2, where M takes the place of a transition metal like Mo, Ta, or W and X is a chalcogen like S or Se or Te [3, 57]. A distinction needs to be made between bulk TMDCs and TMDC monolayers. Bulk TMDCs consist of many layers of TMDC monolayers. Within those layers the atoms are

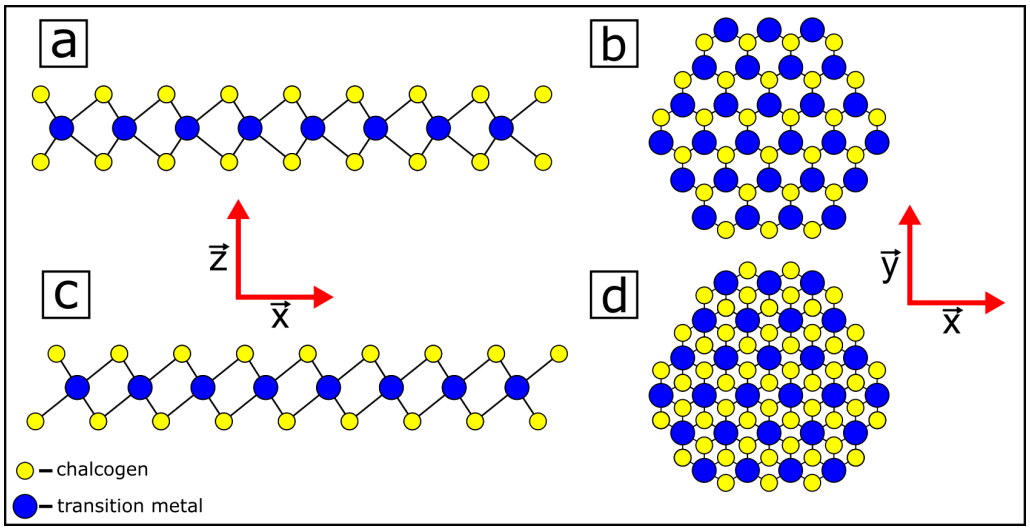


Figure 2.9: Schematics of generalised TMDC monolayers: a) side view of 2H phase; b) top view of 2H phase; c) side view of 1T phase, d) top view of 1T phase.

covalently bond according to the MX_2 formula forming a "sandwich" structure. The chalcogen atoms are located in the top and bottom row of the material, with the transition metal in the middle. Multiple layers form the bulk materials by bonding through van der Waals forces [58]. Therefore, TMDC monolayers represent a single (in theoretical description freestanding) layer, following the MX_2 description. The height of this layer is only one unit cell.

The presence of only a single layer can break the inversion symmetry of the material and create a quantum confinement, which in turn leads to the creation of effects like non-linear optical phenomena and changes the electronic band structure [59][60]. Depending on the chemical composition of the material (e.g. filling

state of the d-band of the metal element) and their structural composition, TMDC monolayers can be metallic, semimetallic, semiconducting, insulating, or superconducting [60].

Figure 2.9 shows the structures of the two main phases which this description will be focused on. These are the 2H phase (figure 2.9 a) and b)) and the 1T phase (figure 2.9 c) and d)). The 2H phase has a trigonal prismatic geometry. This means that the atoms in the top layer of chalcogens have the same position in the x-y-plane as the chalcogen atoms in the bottom layer. Within this plane the chalcogen atoms form a triangular structure and the metal atoms are not only located in the middle of the z-plane, between the top and bottom chalcogen layer, but also in the center of the triangular structure formed in the x-y-plane. In contrast to this, the 1T phase has an octahedral geometry. Therefore, the two layers of chalcogens have a 60°-rotation to each other and the chalcogen atoms do not sit atop each other [61]. This can be clearly seen in the side view in figure 2.9 c). Equally, when looking at the top view, the bottom layer becomes visible as shown in figure 2.9 d). However, it must be stated that this is only a geometric schematic and has no bearing on which row of atoms can be imaged with a given measurement technique. In STM measurements for example, only the top layer of sulfur is imaged, independent of the phase present [17, 62]. To determine the phases in a given STM image, secondary effects like apparent height or moiré patterns need to be used.

2.5.2 TMDC Unit Cell and Lattice Constant

The unit cell of a TMDC plays an important role in the structural analyses in chapters to come. Therefore, it shall be discussed here shortly for the involved materials (see also [63]). Many unit cells can be defined for the 2H phase and 1T phase

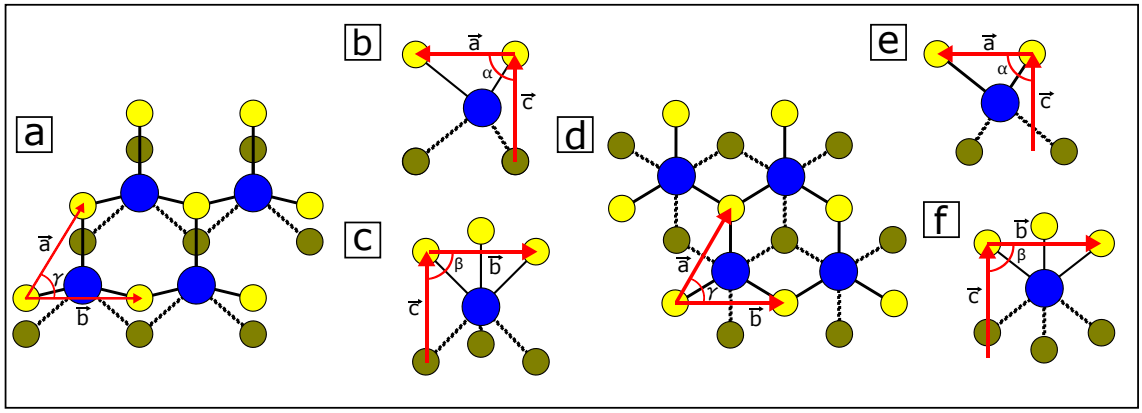


Figure 2.10: a)-c) Schematics of a generalized TMDC monolayer in 2H phase, in top view (a) and two side views (b, c); d)-f) Schematics of a generalized TMDC monolayer in 1T phase, in top view (d) and two side views (e, f). Unit cell vectors are marked with red arrows and labeled $\vec{a}$, $\vec{b}$ and $\vec{c}$ respectively. The angles between the unit cell vectors are given as α, β, and γ. Chalcogen atoms of the top layer are given in bright yellow and chalcogen atoms of the bottom layer in dark yellow. Transition metals are given in blue.

present in TMDC monolayers. Figure 2.10 lays out one example for each phase, defining their lattice vectors in three dimensions and marking them in red. Figure 2.10 a)-c) shows different perspectives of the 2H phase. With figure 2.10 a) showing the lattice almost from atop and figure 2.10 b) and c) showing perspectives from the side. The chosen unit cell is defined by three vectors $\vec{a}$, $\vec{b}$ and $\vec{c}$ as well as the angles α, β, and γ between them. The angles α and β beta are 90° and γ is a 60° angle. The transition metal is located between a layer of sulfur atop it and one beneath it.

The 1T phase is shown similarly in figure 2.10 d)-f). Figure 2.10 d) shows a view from the top and figure 2.10 e) and f) show views from the side. The unit cell is equally defined by three vectors $\vec{a}$, $\vec{b}$, $\vec{c}$ and the angles α, β, and γ between them. Again α and β are of 90° and γ is a 60° angle.

For both the 2H phase and the 1T phase $\vec{a}$, $\vec{b}$ lie in the x-y-plane while $\vec{c}$ is in z-direction. These two vectors describe the lattice constant which is evaluated in this thesis and since $|\vec{a}| = |\vec{b}|$ also describe any direction which might be measured. Since the subject is 2H- and 1T-phase monolayers, which repeat in the x-y-plane, $\vec{c}$ has only been defined for completeness sake and to define the full volume of the monolayer unit cell. In most cases only $\vec{a}$ or $\vec{b}$ are of interest and $\vec{c}$ is omitted, since a monolayer does not repeat in z-direction. The MoS_2 and TaS_2 presented in this thesis, freestanding and in CLH [26], are known to crystallize in the 2H phase with a x-y-plane lattice constants of a_{MoS_2} = (0.3157 $\pm$ 0.0003) nm [64] and a_{TaS_2} = (0.33 $\pm$ 0.001) nm [40] on Au(111).

2.5.3 Stacking Registry of TMDCs on FCC- and HCP-Stacked Substrates

To gain a full understanding of TMDC monolayers atop an Au(111) surface it is important to analyse the possible stacking registries and orienations of a generalised TMDC on an fcc- and an hcp-stacked substrate, since the Au(111) surface exhibits areas of both those stacking orders. For illustrative purposes such a TMDC can be reduced to its top view. In this case the 2H phase has been chosen. This means a hexagonal Bravais lattice with a two atomic basis is present, as only the top chalcogen layer and the transition metal layer in the middle can be seen. To further simplify, the discussion will take place for a

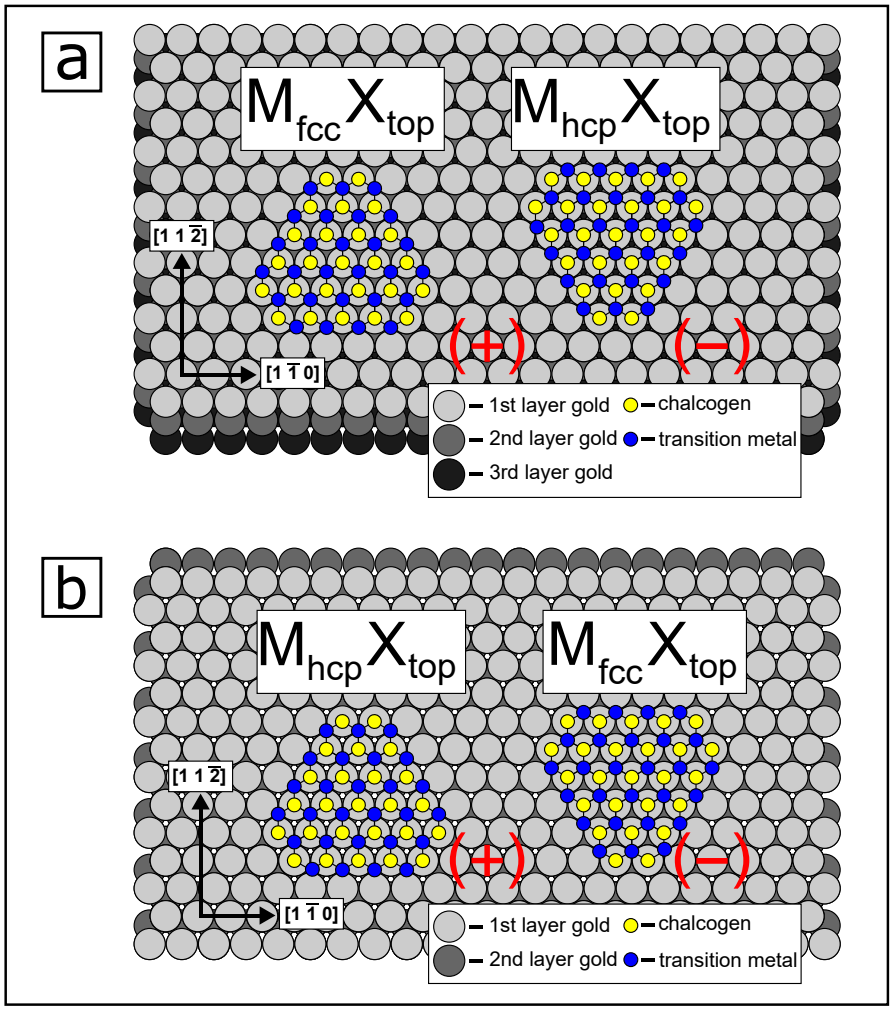


Figure 2.11: Stacking registries of 2H monolayer on fcc- and hcp-stacked substrate and example orientations; a) Stacking registries on fcc substrate. Left: $M_{fcc}X_{top}$, with (+)-orientation, Right: $M_{hcp}X_{top}$, with (-)-orienation; b) Stacking registries on hcp substrate. Left: $M_{hcp}X_{top}$, with (+)-orientation, Right: $M_{fcc}X_{top}$, with (-)-orientation.

state where the monolayer is commensurate with the substrate. In most realistic situations this is only periodically the case, as the lattice constant of most TMDC monolayers is either bigger or smaller than that of the Au(111) surface, leading to a moiré pattern (see chapter 2.7). It has been established in the past that two registries are common for TMDCs with the sixfold symmetric first layer of an fcc(111) surface [65, 66, 67, 68].

An illustration of these two commensurate stacking registries can be seen in figure 2.11. Figure 2.11 a) shows the registries of the 2H monolayer on an fcc-stacked substrate and figure 2.11 b) on an hcp-stacked substrate. Two registry variations are possible each and both are present on each type of substrate. One is $M_{fcc}X_{top}$, shown on the left side of figure 2.11 a) and the right side of figure 2.11 b) and the other is $M_{hcp}X_{top}$, seen on the right of figure 2.11 a) and the left of figure 2.11 b).

For $M_{fcc}X_{top}$ the metal atoms sit in the threefold-hollow sites of the fcc type and the chalcogen atoms sit directly on top of atoms of the surface layer. Similarly for $M_{hcp}X_{top}$ the metal atoms sit in the threefold hollow sites of the hcp type and the chalcogen atoms, again, sit atop the atoms of the surface layer.

In addition to the stacking registry, the orientation of the islands can be described in reference to their edge terminations. Each island exhibits two different types of edge terminations. Either metal atoms are present at the edge or chalcogen atoms. Due to the threefold symmetry of the structure, three edges terminate in metal atoms and three edges terminate in chalcogen atoms. The orientation of these edges is always 60°-rotated in comparison to each other.

For the case of perfect hexagons a geometric distinction would be impossible but as the islands that will be shown later in this thesis present a shape closer to truncated trigonal than hexagonal, we can define the following geometric identifiers: If a shorter edge is pointing in $[1\,1\,\bar{2}]$ direction, the island is denoted as having a (+)-orientation (see figure 2.11 a) left and b) left). Following this scheme, if a longer edge is pointing in $[1\,1\,\bar{2}]$ direction, the island is denoted as having (-)-orientation (see figure 2.11 a) right and b) right). Both the (+)- and (-)-orientation are possible for an $M_{fcc}X_{top}$ registry and an $M_{hcp}X_{top}$ registry on both a substrate of fcc and hcp stacking, leaving four options for a TMDC island to lay upon an each type of substrate stacking (for visual brevity only two options each are shown in figure 2.11).

2.6 Transition Metal Dichalcogenide Heterostructures

The world of TMDC structures encompasses more than just islands made from one type of TMDC. Heterostructures of two or more materials are not only imaginable but have been grown reliably in-plane [69, 70, 68] and out-of-plane [71]. This chapter will focus only on in-plane heterostructures, while explaining the general principle of a TMDC heterostructure, the concept of a concentric lateral heterostructure, and their interfaces. It is of note at this point that, in contrast to [68], the line of connection will be referred to as an *interface* instead of a *junction* throughout this dissertation, as only the geometric structure is of interest and no electronic effects or applications are discussed.

2.6.1 Lateral Heterostructures and Concentric Lateral Heterostructures

An in-plane TMDC heterostructure is defined by the fact that two or more differing TMDCs are connected to each other in the plane of their extension, rather than stacked on top of each other. This connection is facilitated by covalent bonds expanding the structure from one material to the other.

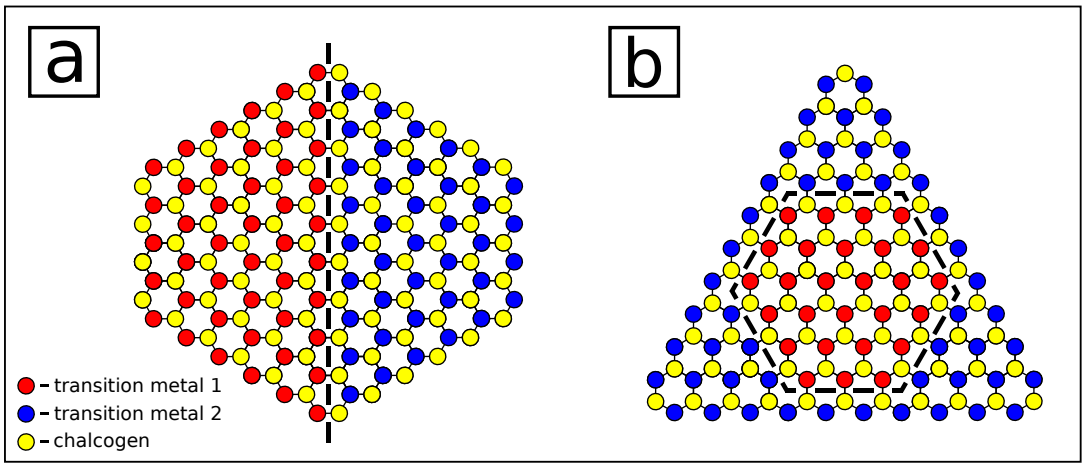


Figure 2.12: Examples of in-plane 2H-TMDC heterostructures in top view. Black dashed lines indicate the interfaces where the materials connect: a) Lateral heterostructure with one interface, connecting the material on the left to the material on the right; b) Concentric lateral heterostructure, where the material in the center is wholly encapsulated by the one surrounding it.

Figure 2.12 shows two examples of this, with one TMDC identified by a red transition metal and yellow chalcogen atoms and the other by blue transition metals and yellow chalcogen atoms. A black dashed line shows the location of the interfaces between the two materials. Both TMDCs are displayed in top view. In figure 2.12 a) two materials are connected along one direction only, forming a simple heterostructure. In figure 2.12 b) two materials are connected along lines in multiple directions, so that one material is completely encapsulated by the other, making this a concentric lateral heterostructure.

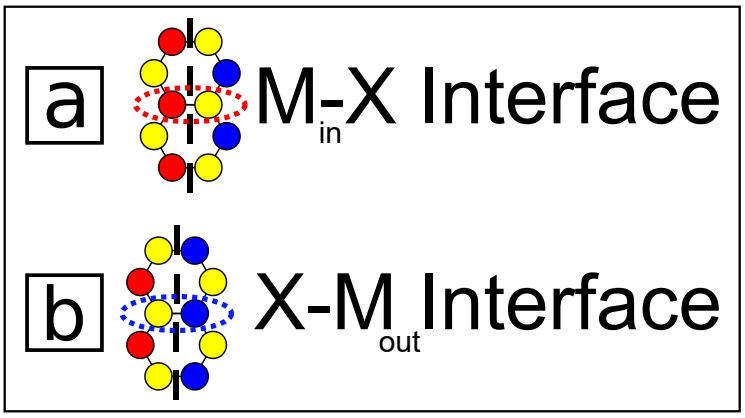


Figure 2.13: Illustration of the two types of interfaces which can present in CLHs: a) M_{in}-X interface; b) X-M_{out} interface; The transition metal on the defined inside is shown in red, the one on the outside in blue, and chalcogen atoms are given in yellow. A black dashed line separates the inside from the outside and a red or blue dashed oval marks the defining bonds crossing the interface.

Taking the example of two 2H TMDCs, a seamless connection can be achieved in two ways. Figure 2.13 shows these two options. The change from one TMDC to another is displayed, again, in top view, with the exact interface position also marked by a black dashed line. Additionally the signature part of the interface, the covalent bond crossing it, giving the interface its name, is marked with a red or blue dashed oval. In figure 2.13 a) an M_{in}-X interface is displayed. Within the red oval, it can be seen that the bond crossing the interface comes from the last atom of the TMDC on the left side, a metal atom, and connects to the first atom of the TMDC on the right side, a chalcogen atom.

Similarly figure 2.13 b) shows an M_{out}-X interface. Here the bond crossing the interface is starting at a chalcogen atom, as the last atom of the TMDC on the left side, and is connected to a metal atom, as the first atom on the right side of the interface. The defining characteristic is therefore which TMDC contributes a metal atom and which TMDC contributes a chalcogen atom to the bond crossing the interface.

Since CLHs have one TMDC on the inside and one TMDC surrounding it, a naming convention has been chosen to address this. Therefore, if the TMDC on the inside contributes the metal atom, it is an M_{in}-X interface and if the surrounding TMDC, which is on the outside, contributes the metal atom, it is an M_{out}-X interface. The CLH in figure 2.12 therefore exhibits both M_{in}-X interfaces and an M_{out}-X interfaces.

2.6.2 Stacking Registries

Building on the results from the previous subchapter, the stacking registries of CLHs with fcc- and hcp-stacked substrates as well as the location of the interfaces within them can be discussed. As mentioned before, a CLHs is a lateral heterostructure wherein one type of TMDC is fully surrounded by a differing type of TMDC.

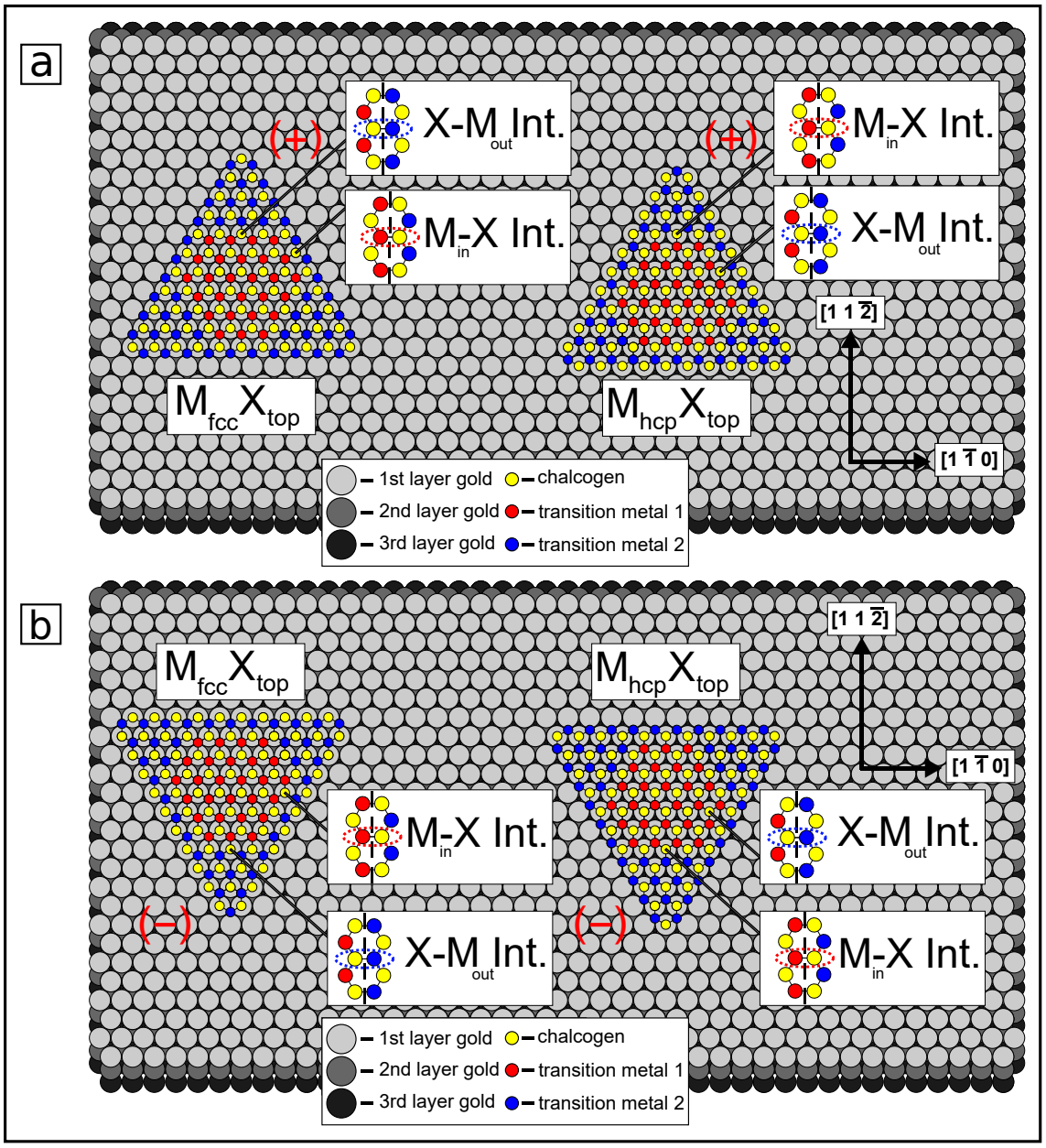


Figure 2.14: Stacking registries of CLHs on fcc-stacked substrate (gold as example) with different orientations and highlighted interface types; a) Left: $M_{fcc}X_{top}$, with (+)-orientation, Right: $M_{hcp}X_{top}$, with (+)-orientation; b) Left: $M_{fcc}X_{top}$, with (-)-orientation, Right: $M_{hcp}X_{top}$, with (-)-orientation.

Similarly to freestanding TMDC islands, it is useful to understand the possibilities for stacking registries and orientation of CLHs on fcc- and hcp-stacked substrates, as well as the relative location of the types of interfaces resulting from the connection of two TMDCs on these substrates. Analogue to chapter 2.5.3 the stacking orders are highlighted for the commensurate case between substrate and superlayer.

Figure 2.14 shows illustrations of the resulting registries, orientations, and interfaces on an fcc-stacked substrate. Again the two stacking registries are $M_{fcc}X_{top}$, with the metal atoms in the threefold-hollow sites of the fcc type of the top layer of the substrate and the chalcogen atoms directly atop the atoms of this top layer and $M_{hcp}X_{top}$, wherein the metal atoms sit in the threefold-hollow sites of the hcp type of the top layer and the chalcogen atoms, again, sit on top of the atoms of the top layer.

For the orientations, the already established naming scheme has also been followed. The islands with a shorter edge oriented in $[1\,1\,\overline{2}]$ direction are named (+)-oriented and islands where a long edge is oriented in $[1\,1\,\overline{2}]$ direction named (-)-oriented. But here a clarification has to be made, as in the chosen examples, the CLHs exhibit a triangular shape, instead of a truncated triangular or hexagonal shape, a quick definition for a long edge and a short edge is necessary. The long edges are represented by the (long) sides of the triangle, while the short edges are represented by the points of the triangles.

Similar possibilities emerge for the edge terminations. Either the long edges are metal terminated, or chalcogen terminated. For the (+)-orientation the $M_{fcc}X_{top}$ registry has metal-terminated long edges and chalcogen-terminated short edges, while $M_{hcp}X_{top}$ stacking exhibits chalcogen-terminated long edges and metal-terminated short edges. In the (-)-orientation this behavior inverts with $M_{fcc}X_{top}$ having chalcogen-terminated long edges and metal-terminated short edges, while $M_{hcp}X_{top}$ has metal-terminated long edges and chalcogen-terminated short edges.

Additionally, the interface types are marked. Each CLH exhibits three M_{in}-X interfaces and three M_{out}-X interfaces, for symmetry reasons. The interface type changes with every 60° rotation. In CLHs with $M_{fcc}X_{top}$ registry and the (+)-orientation, as well as $M_{hcp}X_{top}$ registry with (-)-orientation, an interface of type M_{out}-X is oriented in $[1\,1\,\overline{2}]$ direction. For CLH with $M_{hcp}X_{top}$ registry and (+)-orientation, as well as $M_{fcc}X_{top}$ registry with the (-)-orientation, an interface of the type M_{in}-X is oriented in the $[1\,1\,\overline{2}]$ direction.

Since the hcp region of Au(111), which is used as a substrate in this thesis, with respect to the first two substrate layers, is just an 180° rotation of the fcc region, all these description are inverted for its case. The results of this can be seen in figure 2.15.

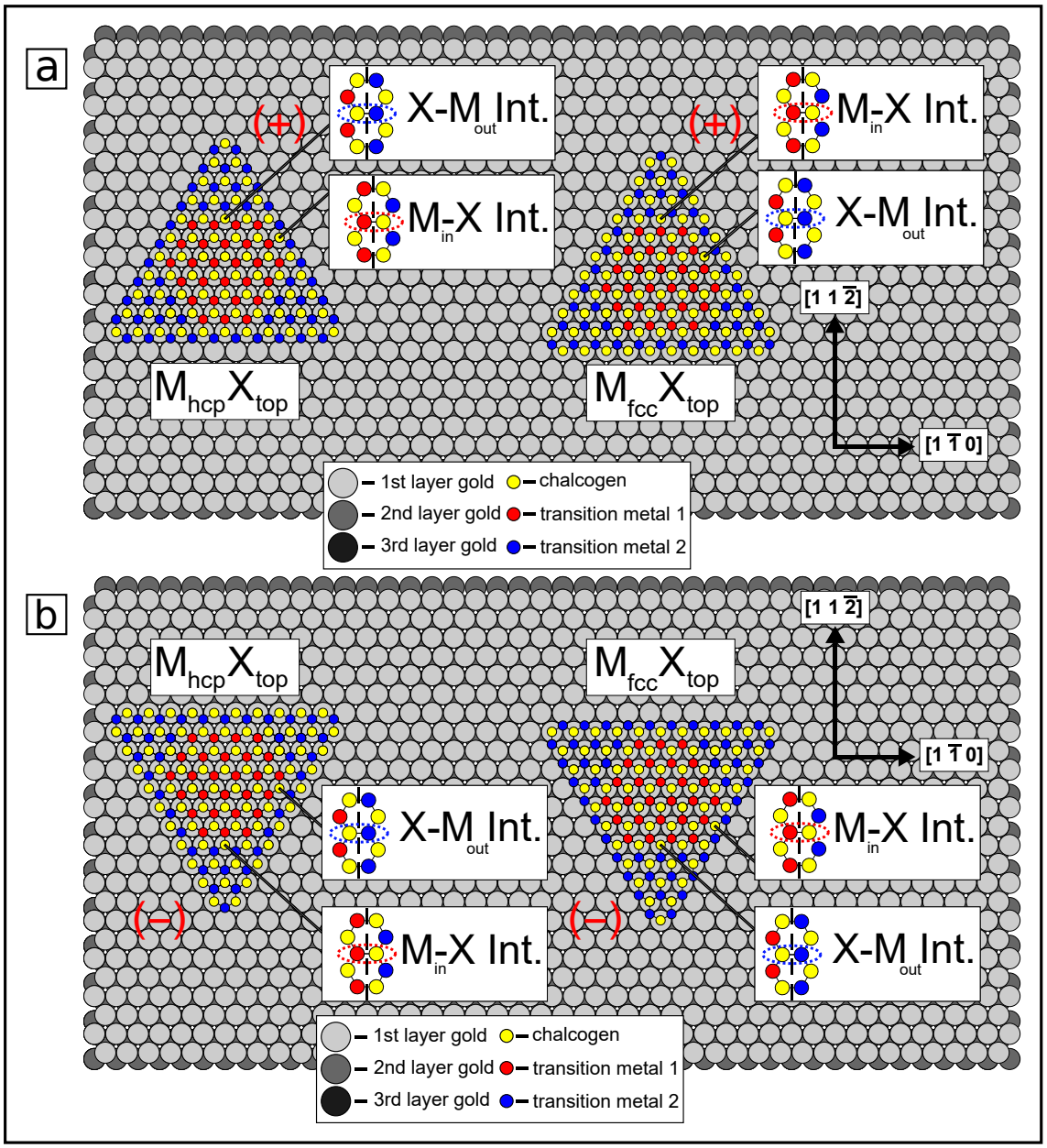


Figure 2.15: Stacking registries of CLHs on hcp-stacked substrate (gold as example) with different orientations and highlighted interface types; a) Left: $M_{hcp}X_{top}$, with (+)-orientation, Right: $M_{fcc}X_{top}$, with (+)-orientation; b) Left: $M_{hcp}X_{top}$, with (-)-orientation, Right: $M_{fcc}X_{top}$, with (-)-orientation.

2.7 Moiré Pattern

An effect repeatedly encountered in surface science, and especially in the investigation of TMDCs on various substrates, is the moiré effect. The effect describes the creation of a superlattice by the overlap of two lattices with a rotation between each other (see figure 2.16 a)) or of differing lattice constants (see figure 2.16 b)). Here the varying proximity of the motifs (e.g. atoms of group of atoms in the case of a moiré between two crystal lattices), create the appearance of the superlattice. In general terms this new lattice is not a real structure but emergent from the changing proximities of the two lattices. It can however have a tangible impact on the properties of two materials, both structurally or electronically [72, 73].

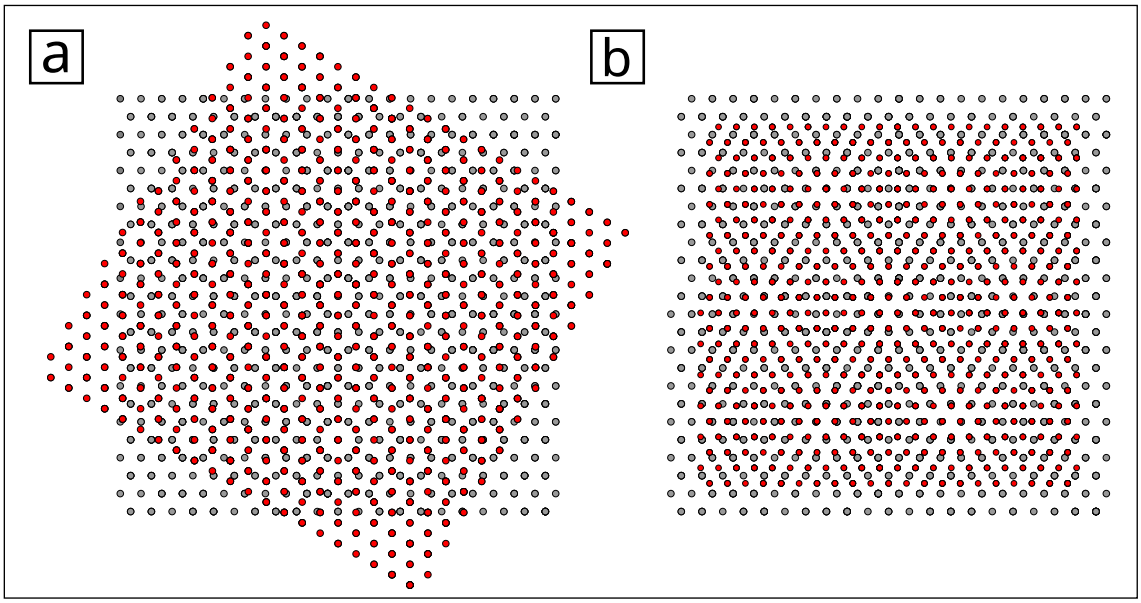


Figure 2.16: Illustrations of moiré patterns arising between two stacked layers, with the layer below in gray and the layer atop in red: a) Moiré pattern caused by rotation between two hexagonal lattices; b) Moiré pattern caused by two hexagonal lattices, with differing lattice constants.

Moreover, a moiré pattern is a useful effect in surface science to calculate the lattice constants of the underlying lattices, since it is often easier to measure a moiré pattern than an atomic lattice itself. Based on the work given in [74] a summary of the approach to moiré patterns shall be given in this chapter. To keep this summary to a reasonable length, the following will only focus on the overlap of reflective, monochromatic patterns, that are real valued, symmetric and not shifted. An approach that is sufficient to describe the moiré patterns observed in

this thesis.

Varying ways to calculate the moiré pattern from overlapping lattices and vice versa exist, being geometric approaches based on the properties of the superimposed layers, an initial approach based on algebra or theory of non standard analysis, which result in equations with more and less restrictions of application and power of prediction. Still, arguably the best approach to moiré patterns is a spectral approach based on Fourier theory. Accordingly, a moiré lattice can not only be described in real space and the x-y-plane by a function $f(x, y)$ but also by a function $F(u, v)$ in Fourier space and the u-v-plane. In both of these spaces polar coordinates also present an option, but this summary will focus on a description in Cartesian coordinates. In Fourier space the function is not described in terms of its values at a certain coordinate, but the presence of frequencies in the original image, meaning, that if a periodic structure appears in real space, the corresponding position in Fourier space will have a maximum. A pattern described by a function $f(x, y)$ in real-space can be transformed into a function $F(u, v)$ in Fourier-space and vice versa, without the gain or loss of information by the following transformations, known as Fourier transformation (FT):

$$F(u, v) = \int_{-\infty}^{\infty} \int_{-\infty}^{\infty} f(x, y) e^{-2i\pi(ux+vy)} dxdy, \tag{2.25}$$

$$f(x, y) = \int_{-\infty}^{\infty} \int_{-\infty}^{\infty} F(u, v) e^{-2i\pi(ux+vy)} dxdy. \tag{2.26}$$

A sufficient case for the description of moiré patterns in 2D materials is the overlap of monochrome images. Here an image of multiple overlapping patterns can be described in terms of a multiplication of the respective reflectivenesses:

$$r(x, y) = \prod_{i=1}^{m} r_i(x, y). \tag{2.27}$$

Following this, according to the convolution theorem, the FT of a function product is the convolution of the FT of the individual functions. Therefore we can define

$$R(u, v) = R_1(u, v) ** R_2(u, v) ... ** R_m(u, v), \tag{2.28}$$

with the capitalized functions $R(u, v)$ and $R_1(u, v)$-$R_m(u, v)$ as the Fourier transformed versions of their uncapitalized correspondents and "$**$" as a convolution operator. As a general rule, each frequency of the original image is represented

by a frequency vector **f** and a frequency vector **-f** in Fourier space. To illustrate the calculation and the emergence of a moiré pattern, a good example is the superposition of two cosinusoidal patterns:

$$r_1(x,y) = \frac{1}{2}cos(2\pi f_1 x) + \frac{1}{2}, \tag{2.29}$$

and

$$r_2(x,y) = \frac{1}{2}cos(2\pi f_2[xcos(\theta_2) + ysin(\theta_2)]) + \frac{1}{2}. \tag{2.30}$$

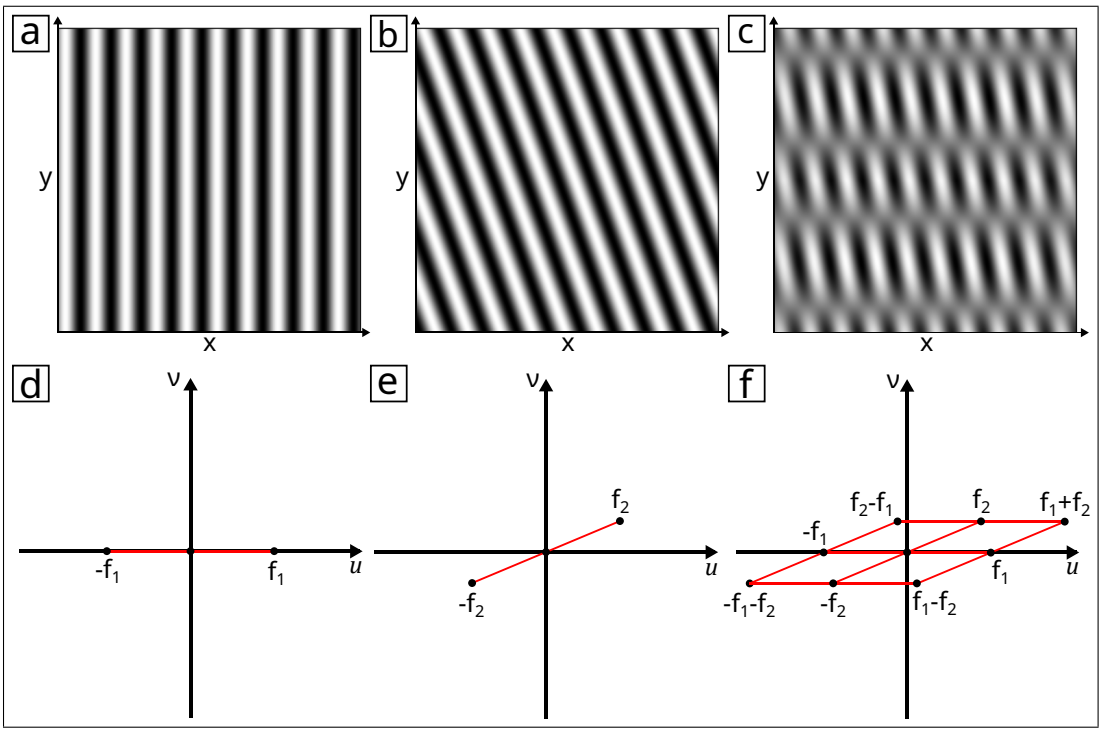


Figure 2.17: a) Cosinoidal grating from equation 2.29; b) Cosinoidal grating from equation 2.30; c) Convolution from the gratings in *a* and *b*, d) Expected Fourier transform of *a* with its frequency vectors $\mathbf{f_1}$ and -$\mathbf{f_1}$, e) Expected Fourier transform of *b* with its frequency vectors $\mathbf{f_2}$ and -$\mathbf{f_2}$, f) Expected Fourier transform of *c*, with all the resulting frequencies $\mathbf{f_1}$+$\mathbf{f_2}$, -$\mathbf{f_1}$-$\mathbf{f_2}$ and $\mathbf{f_1}$-$\mathbf{f_2}$, $\mathbf{f_2}$-$\mathbf{f_1}$. Image in reference to [75].

Figure 2.17 a) and b) show a representation of these two periodic gratings and figure 2.17 d) and c) show the Fourier transformations those two. Both of them exhibit impulses, located at two frequency vectors $\mathbf{f_1}$, **-f**$_1$ for the grating from a) and $\mathbf{f_2}$, **-f**$_2$ for the grating from b), representing the periodic components in the real space image. The impulses are marked with a dot. The intensity of the impulse, which is not shown here, represents the prevalence of the related periodic component in the original image. Since these are real-valued and symmetric gratings, each periodic component in the original image has two equal frequency compo-

nents with their impulses located in Fourier space at **f** and an equal impulse located at **-f** [76]. Additionally a zero impulse is located at the origin. This impulse corresponds to the constant component in the two images. In figure 2.17 d) the real space image, resulting from the superposition of the grating from a) and b), is shown. A prominent moiré can be seen.

According to equation 2.27 and equation 2.29 the convolution consists of nine frequencies. This means two new impulse pairs appear in the convoluted image. These are located at $\mathbf{f}_1$+$\mathbf{f}_2$, -$\mathbf{f}_1$-$\mathbf{f}_2$ and $\mathbf{f}_1$-$\mathbf{f}_2$, $\mathbf{f}_2$-$\mathbf{f}_1$, as can be seen in figure 2.17 f). The existence of these additional impulses in Fourier space and their connected periodicities in real space are the essence of the moiré effect.

The frequency vectors of the new impulses can be summarized as

$$g_{\mathrm{m,n}}(u,v) = g_{\mathrm{m}}(u,v) - g_{\mathrm{n}}(u,v). \tag{2.31}$$

Here m and n are the index of the available frequency vectors from the two grids. Again, this equation only describes first order impulses but can be extended by multiplying with whole numbers to get the higher order impulses. Since these are not presented here, this section will not go into detail about this topic.

While technically all these new frequencies are part of the moiré effect, it is often ascribed to the most visible new frequencies. Since the new impulse pairs located at $\mathbf{f}_1$-$\mathbf{f}_2$ and $\mathbf{f}_2$-$\mathbf{f}_1$ are the closest to the zero impulse and therefore have the lowest frequency, they will be most visible in the real space image. This leads to the general rule for moiré of:

$$g_{moire}(u,v) = g_1(u,v) - g_2(u,v). \tag{2.32}$$

2.7.1 Hexagonal Patterns

A reappearing pattern in this thesis is the hexagonal grid. This section will shortly explain the theory behind the overlap of two hexagonal grids based on [77, 78]. Let these two hexagonal grids be called $r_1(x,y)$ and $r_2(x,y)$ and their linear transformations be $g_1(x,y)$ and $g_2(x,y)$ given as follows:

$$g_1(x,y) = \begin{pmatrix} f_1 & 0 \\ 0 & f_1 \end{pmatrix} \begin{pmatrix} cos(\theta_1) & sin(\theta_1) \\ -sin(\theta_1) & cos(\theta_1) \end{pmatrix} \begin{pmatrix} 1 & -\frac{1}{\sqrt{3}} \\ 0 & \frac{2}{\sqrt{3}} \end{pmatrix} \begin{pmatrix} x \\ y \end{pmatrix}, \tag{2.33}$$

$$g_1(x,y) = \begin{pmatrix} f_2 & 0 \\ 0 & f_2 \end{pmatrix} \begin{pmatrix} cos(\theta_2) & sin(\theta_2) \\ -sin(\theta_2) & cos(\theta_2) \end{pmatrix} \begin{pmatrix} 1 & -\frac{1}{\sqrt{3}} \\ 0 & \frac{2}{\sqrt{3}} \end{pmatrix} \begin{pmatrix} x \\ y \end{pmatrix}. \tag{2.34}$$

Now applying equation 2.32 to this case:

$$g_{hexagonal}(x,y) = g_1(x,y) - g_2(x,y) =$$

$$\begin{pmatrix} f_1cos(\theta_1) - f_2cos(\theta_2) & f_1sin(\theta_1) - f_2sin(\theta_2) \\ -(f_1sin(\theta_1) - f_2sin(\theta_2)) & f_1cos(\theta_1) - f_2cos(\theta_2) \end{pmatrix} \begin{pmatrix} 1 & -\frac{1}{\sqrt{3}} \\ 0 & \frac{2}{\sqrt{3}} \end{pmatrix} \begin{pmatrix} x \\ y \end{pmatrix} \tag{2.35}$$

Since the first matrix in the result is a similarity matrix, it follows that the result of this equation is also a hexagonal grid, as the two underlying grids are.

2.7.2 Classical moiré formula

The simplest case of a moiré pattern is the overlap of two linear gratings. According to [79] a simple and useful approximation for this case can be described as follows, for $T_1 \approx T_2$:

$$T_{\mathbf{M}} = \frac{T_1 T_2}{\sqrt{T_1^2 + T_2^2 - 2T_1T_2cos(\alpha)}}, \tag{2.36}$$

with the T_1 and T_2 as the periods of the two gratings, α the angle between theses two gratings, and T_M the period of the resulting grating. The angle of the new grating is defined as:

$$\phi_M = arctan\left(\frac{T_2sin(\theta_1) - T_1sin(\theta_2)}{T_2cos(\theta_1) - T_1cos(\theta_2)}\right). \tag{2.37}$$

This means the moiré periodicity for two linear gratings can be easily calculated. Moreover, in the case of more complicated structures, only the periodicity for the most prominent motif might be of interest and not the overall structure. In those cases a reduction of the problem in the direction of that motif is useful because it can then be calculated using the classical moiré formula.

2.8 Kirkendall Effect

The Kirkendall effect named after Ernest Kirkendall (1914-2005), and discovered by Ernest Kirkendall and Alice Smigelskas, describes the movement of the interface between differing materials by imbalanced diffusion of holes between them [80]. This new description of diffusion by vacancy movement, in opposition to direct atomic exchange, proved controversial but has now been widely accepted [81]. Kirkendalls original experiment consisted of a bar of brass (70% Cu and 30% Zn) that had Mo wires stretched along its length. The Mo was chosen because of its insolubility in the brass which eliminates errors due to the diffusion of markers themselves. Afterwards the whole bar was coated in copper. In this

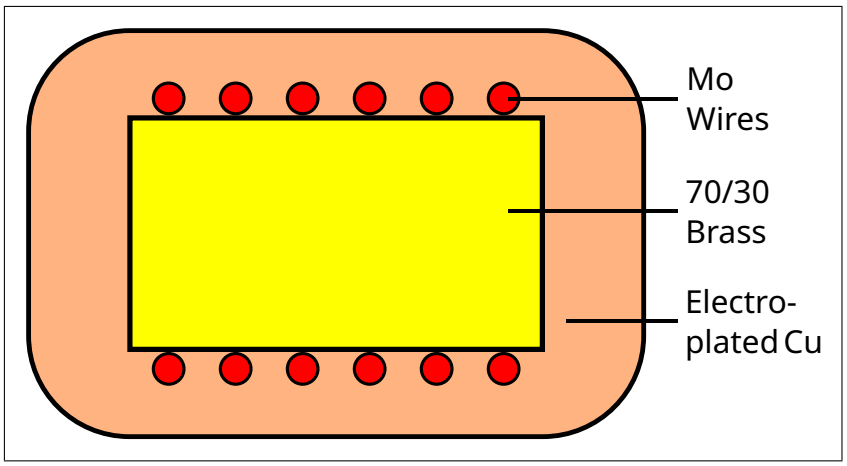


Figure 2.18: Schematic of the sample used in Kirkendalls experiments. Pictured is the brass core with 70% Cu and 30% Zn, with Mo wires along its length and surrounded by Cu. Image in reference to [82].

experiment diffusion took place over 56 days at a temperature of 785 °C. Six cross sections have been taken during this period, showing a movement of the interface. The compositional change was also confirmed by x-ray diffraction [83].

A schematic of this experiment can be seen in figure 2.18. The result showed a movement in marker positions, moving them closer together, as the zinc diffused out of the brass into the copper. The behavior can be explained by the Fick's first law, where

$$J = -D\frac{d\phi}{dx}, \quad [84] \tag{2.38}$$

with J the diffusion flux, D the diffusion coefficient, $\frac{d\phi}{dx}$ the concentration gradient which in turn consists of the concentration ϕ (for ideal mixtures) and the position

x. It states that the diffusion of the material with the higher diffusion coefficient will be net positive into the material with the lower coefficient.

Based on the observations of Kirkendall, the Darken-equations have been developed by Lawrence Stamper Darken in 1948 [85] as follows:

$$\theta = (D_1 - D_2)\frac{dN_1}{dx}. \tag{2.39}$$

Here D_1 and D_2 describe the diffusion coefficients of the two materials, N_1 the atomic fraction and θ the marker velocity. The second Darken-equation describes a combined chemical diffusion coefficient D as:

$$D = N_1 D_2 + N_2 D_1. \tag{2.40}$$

2.8.1 Kirkendall Voids

During the vacancy diffusion process, as described by Kirkendall, a particular effect, which will be of interest in the later chapters, can take place. This is the formation of Kirkendall holes. In the special case, where there is a significant difference in diffusion coefficients in two adjoint materials, vacancies from the material with high mobility are more likely to exit the material with a high vacancy mobility, than the other way around. This leads to an accumulation of vacancies in the material with low mobility close to the border region [86]. If these vacancies cannot be absorbed and distributed fast enough through the low mobility material, according to J.A. Brinkman [87], a threshold can be reached where a stable void is formed. This void can then grow, leading to material destabilization.

CHAPTER 3

PREREQUISITES

3.1 Variable Temperature UHV System TUMA III

The preparation and analysis of 2D materials brings with it its own set of challenges, as these structures present an area in the nm^2 range and a height often below 1 nm [2]. An accumulation of unwanted particles on a surface can very quickly overshadow any materials to be investigated. Additionally, the presence of contaminants during the chemical reactions of the formation process of the 2D materials might lead to impure results. Therefore the preparation and analy-

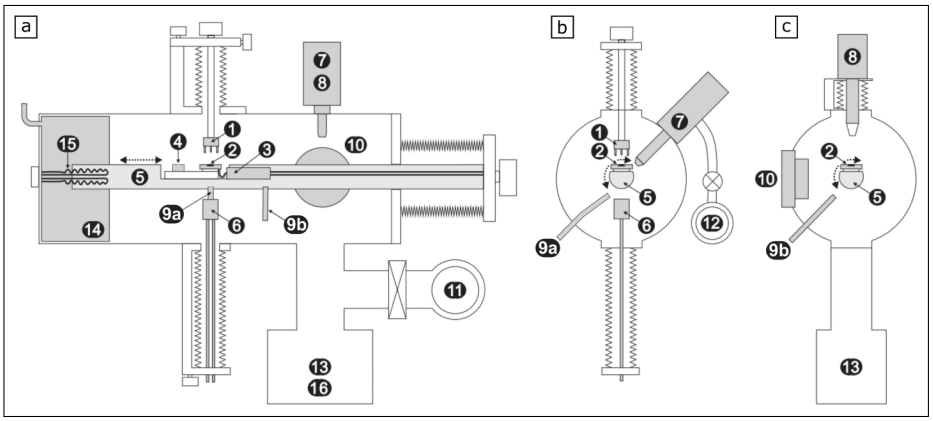


Figure 3.1: Schematic of variable temperature UHV-system TUMAIII with its varying components labeled as follows: 1) STM; 2) Au(111) substrate; 3) Cooling reservoir; 4) Farady cup; 5) Manipulator; 6) E-beam evaporator; 7) Sputter gun; 8) Quadrupol mass spectrometer; 9a) Gas inlet H_2S, 9b) Secondary gas inlet; 10) LEED, 11/12) Turbomolecular pump; 13) Ion pump; 14) Cooling trap, 15) Titanium sublimation pump, 16) Secondary cooling trap; Modified with authors permission from [88].

sis has to take place in an ultra-high vacuum (UHV) chamber. Additionally, any analysis tool has to be able to measure sufficiently small structures in the appropriate, optimally atomic, resolution. The tool of choice in this dissertation is a UHV system equipped with multiple instruments for preparation and analysis,

including a scanning tunneling microscope, called TUMA III.

Figure 3.1 shows three cross sections of this machine, in three different perspectives, while labeling the various components available for experimental needs. The system is equipped with a beetle-type STM (1) and has an integrated sample. In this thesis, a gold single crystal with an Au(111) surface (2) is used. The sample is connected to a high voltage heating system, as well as a cooling reservoir (3) and air cooling. Located next to the sample is a Faraday cup for calibration of the ion gun (4). The whole setup, of sample, Faraday cup, cooling, block, and electronics is located on a manipulator, allowing for movement in (horizontal) z-direction and rotation around the z-axis (5). Located underneath the manipulator and in line with the sample, when in preparation position, is an e-beam evaporator (EGCO4 Oxford Applied Research), equipped with several sublimation chambers (6). These chambers can be filled with an assortment of materials, such as Mo, Ta, W, and V. To the right of the STM and located at an angle, is an ion gun for sample cleaning purposes via Ar^+ (7). Atop the machine, in front of the ion gun, a quadrupole mass spectrometer is mounted (8). It can be used to assess the amount of water or other contaminants in the chamber and detect materials sublimating from the sample during annealing, optimally when placed underneath it. Next to the e-beam evaporator (9a) and in the middle between the e-beam and the ion gun (9b) are two gas inlets. This thesis utilizes inlet (9a) to supply H_2S during growth processes. Underneath the ion gun, a LEED system is located, which can assess sample purity after cleaning, as well as evaluate the presence of periodic structures on its surface (10). As tools of vacuum generation the system uses two turbomolecular pumps (11/12), located underneath the system as well as connected to the ion gun, an ion pump, also underneath the system (13), up to two cooling traps, located in the back of the machine (14) and in the ion pump (16), as well as a titanium sublimation pump (15), located inside the bigger cooling trap at the back. Not pictured are the pre-pump systems connected to the turbomolecular pumps. With this setup the UHV chamber is able to reach a base pressure of 3×10^{-11} mbar. This setup, with its assortment of tools, enables the preparation and analysis of various structures and, since no vacuum lock is present, the removal and cleanup for repeat preparations with different parameters. While low temperature measurements are technically possible, some modifications to the system would be necessary, so all measurements have taken place at room temperature.

3.2 Cyclical Preparation Process

All preparations presented in this thesis are based on a cyclical growth process developed in [26] to originally create TMDC heterostructures and has been modified on a case by case basis. A short description of this process will be given in this chapter, while the exact parameters and deviations will be listed in the chapters corresponding to each specific result. Each preparation starts with a clean

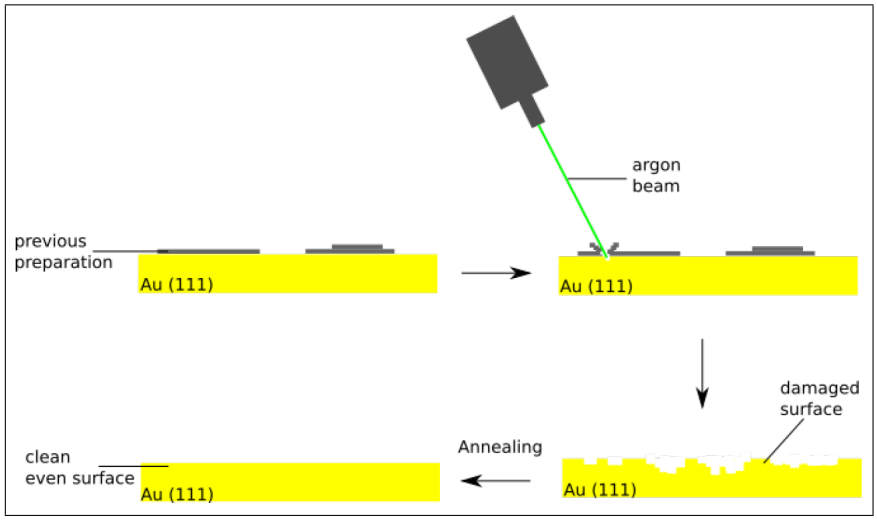


Figure 3.2: Schematic of the sputtering process performed to remove old preparations and create a clean and flat surface for repeat use. Taken with authors permission from [26].

Au(111) surface. This was achieved by two sets of sputtering with Ar^+ at 1.5 keV, first at room temperature (RT) for 30 min and then at 900 K for 30 min. This cleans but roughens the surface, which subsequently is annealed at 900 K for 10 min to restore an even plane. If the previous preparation on the substrate involved a temperature higher than 900 K, that temperature was used for both the high temperature sputtering and the annealing step instead. An overview of the sputtering process can be seen in figure 3.2.

With a clean substrate available, various methods to facilitate epitaxial growth are possible, yet all preparations presented are based on the earlier mentioned cyclical growth process, which itself is based on the process developed by Grønborg et al. to create TMDC monolayers [17].

Firstly, a transition metal is evaporated onto the substrate via e-beam evaporation. Then H_2S is introduced as a sulfur source. As energy is needed to facilitate a reaction with the transition metal, the sample is then heated. In this environment the H2S is broken into H_2 and S at the gold surface. This makes the S available to

the transition metal. A reaction between the transition metal and the S then takes place to form islands on the surface. After a desired annealing time is reached, the sample is cooled down. At an intermediate temperature the H_2S is removed. This finishes the formation process of TMDC islands and when room temperature is reached, a cycle is complete. From this point on the results can either be investigated, additional cycles can be added, or one can remove the results again.

All preparations in this thesis start with a preparation cycle creating MoS_2 is-

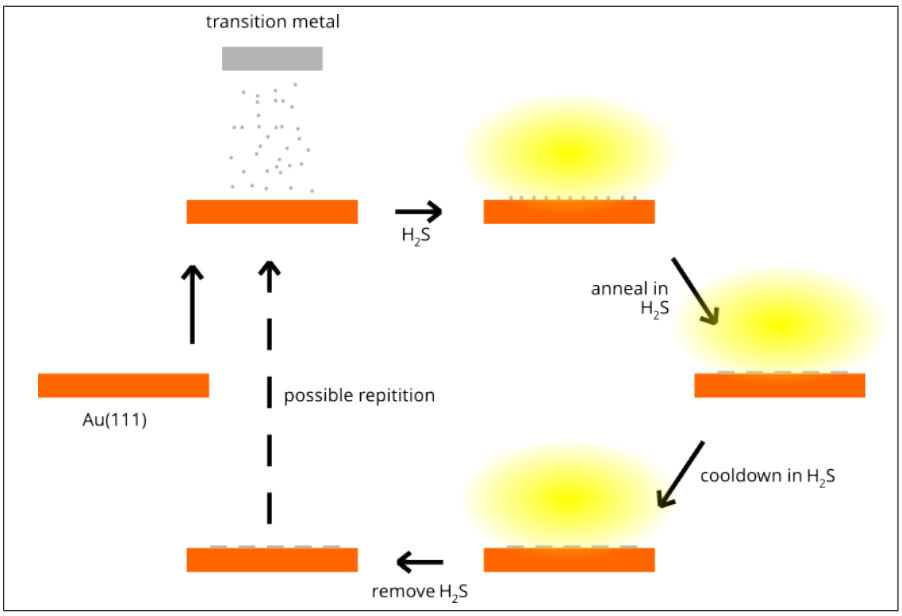


Figure 3.3: Generalized schematic of cyclical growth process, showing core principle to create TMDC. Modified with authors permission from [26].

lands. Therefore a reference recipe to prepare these islands is given as an example in the following.

First Mo is evaporated at RT at a rate of 0.007 monolayers/min. The time of evaporation can be varied to increase or decrease the size and number of MoS_2 islands present on the sample after the preparation is finished. Useful evaporation times are between (5-30) min. This is then followed by annealing in an H_2S atmosphere at a pressure of 1×10^{-5} mbar and at a temperature of 900 K. Afterwards the sample is cooled down, while the pressure of the H_2S is maintained. When the temperature reaches 450 K, the H_2S flow is stopped and the sample cooling is continued until RT is reached. With this MoS_2 islands are created on the surface and additional cycles can be added and tweaked to create MoS_2-TaS_2 heterostructures, alloys and more.

3.3 Distortion Correction

An important factor in STM measurements is the calibration and correction of possible distortions in the measured images. There are three major sources that might lead to an image receiving wrong dimensions. Firstly, the piezo constants need to have an appropriate calibration, so even if no other factors distort the images, results can be of the wrong order of magnitude without this. This is ideally done by measuring reference structures and scaling the constants accordingly.

The other two factors are piezo creep and thermal drift. Even if the piezo constants are generally calibrated correctly, an image might still be distorted, as these effects appear in different magnitudes at different times. Piezo creep, being the residual movement of the piezos after bigger movements, adds a continuous shift in the last used movement direction to the image. This effect can be mitigated by scanning an area of the sample for a long time, after the scanning tip has been moved with larger steps.

Thermal drift occurs due to temperature influence on the movement of the piezos. Similar to piezo creep, it adds an additional multiplier to the movement to capture the image, distorting it. Without any temperature control system for the piezos, recommended steps involve constant RT and letting any substrates fully cool down before taking measurements.

3.3.1 Affine Distortion

The main method used to mitigate linear distortions, resulting from imperfectly set piezo constants, or globally applying piezo creep and thermal drift, in STM images is the affine distortion function, in this case provided by the analysis tool Gwyddion [89]. The following mathematical description is based on [90]. Generally, affine transformations describe transformations that preserve collinearity and ratios of distance. An affine distortions is a composition of rotations, translations, shears and dilations. An adequate example is the combination of rotation and expansion:

$$\begin{bmatrix} x' \\ y' \end{bmatrix} = s \begin{bmatrix} cos(\alpha) & sin(\alpha) \\ -sin(\alpha) & cos(\alpha) \end{bmatrix} \begin{bmatrix} x - x_0 \\ y - y_0 \end{bmatrix}. \tag{3.1}$$

Here s is known as the scaling factor and α is the angle of rotation. To normalize an STM image with Gwyddion, areas of known periodicity are selected and a grid is applied to them. This grid defines the starting 2D unit cell vectors. Since

the periodic structure is known, the correct length of the vectors and the angle between them can be entered and an affine transformation is calculated and applied to the image, creating a corrected image. The values of this transformation can subsequently be applied to other STM images to prepare them with the same distortion correction.

If no known reference structure is present on the image, assumptions about the correct angles of structures and estimations of the lattice vectors, by analysis of directions usually least distorted, e.g. the scan direction of the tip, can be made but this is generally not recommended. If the image distortion is systematic, like wrongly set piezo constants or a temperature hike in the environment, best results can usually be achieved by applying a normalization acquired from a reference structure measured close in time to the current image.

3.4 Monte Carlo Simulation

In chapter 4.3, Kirkendall voids in transition metal dichalcogenide monolayers are observed. To further illustrate the process of vacancy diffusion, a Monte Carlo simulation has been constructed. While the whole code of the simulation can be found in chapter 7, the general working principles are summarized in this chapter.

A simplified system, taking place in the metal sublayer of the TMDCs has been chosen. This is analogue to representing individual unit cells. It displays and deals with the two types of metal atoms and metal vacancies. All three are of the same size and can occupy distinct places on a two dimensional plane. These distinct places are distributed in a hexagonal Bravais lattice to approximate the lattice structures of MoS_2 and TaS_2.

3.4.1 Choice of Vacancy

On each iteration of the simulation a vacancy is chosen as the main vector of change to facilitate the vacancy diffusion. To simulate the difference in vacancy mobility, depending on the surrounding material each vacancy is moving in, the ratio of the diffusion coefficients has been calculated. According to the Arrhenius equation, the coefficient follows as:

$$D = D_0 \cdot e^{-E_A/k_B T}. \quad [91] \tag{3.2}$$

Here D_0 denotes the maximal diffusion rate at infinite temperatures, E_A the activation energy for vacancy diffusion, k_B the Boltzmann constant and T the temperature of the process. With the two materials, MoS_2 and TaS_2, this results in the following ratio:

$$\frac{D_{TaS_2}}{D_{MoS_2}} = \frac{D_{0,TaS_2}}{D_{0,MoS_2}} \cdot \frac{e^{-E_{A,TaS_2}/k_B T}}{e^{-E_{A,MoS_2}/k_B T}}. \tag{3.3}$$

It is assumed that the diffusion rates at infinite temperatures are equal for both materials. Therefore the equation simplifies to

$$\frac{D_{TaS_2}}{D_{MoS_2}} = e^{-(E_{A,TaS_2} - E_{A,MoS_2})/k_B T}. \tag{3.4}$$

The activation energies can be gathered from the DFT results of figure 4.23. These result in

$$E_{\mathrm{A,TaS_2}} \approx 2.034\ eV, \tag{3.5}$$

and

$$E_{\mathrm{A,MoS_2}} \approx 2.925\ eV. \tag{3.6}$$

After inputting these values into equation 3.4, including a process temperature of 900 K, we get a ratio of

$$\frac{D_{\mathrm{TaS_2}}}{D_{\mathrm{MoS_2}}} = 97849. \tag{3.7}$$

This means, that the speed of the vacancy is 97849 times faster inside of TaS_2 than inside MoS_2. The simulation takes this into account by a weighted chance for a vacancy to be chosen to move, based on its surrounding material. During every iteration of the program a list of all vacancies and its six nearest neighbors is made. Then all vacancies that are surrounded by three or more other vacancies are removed from that list. For the remaining vacancies an average movement speed is calculated to weigh its chance of being chosen. The movement speed fully surrounded by TaS_2 is set as one and the movement speed fully surrounded by MoS_2 is assigned 1/97849. All nearest neighbor vacancies are excluded from these calculations beforehand. For example, a vacancy is surrounded by two other vacancies, two unit cells of MoS_2 and two unit cells of TaS_2. The two vacancies are excluded from the calculation. Then the average speed based on the remaining unit cells is calculated as

$$D_{\mathrm{average}} = \frac{(1 \cdot D_{\mathrm{TaS_2}} + 1 \cdot D_{\mathrm{TaS_2}} + \frac{1}{97849} \cdot D_{\mathrm{MoS_2}} + \frac{1}{97849} \cdot D_{\mathrm{MoS_2}})}{4}. \tag{3.8}$$

This can be generalised to

$$D_{\mathrm{average}} = \frac{a \cdot D_{\mathrm{TaS_2}} + b \cdot \frac{1}{97849} \cdot D_{\mathrm{MoS_2}}}{a+b}. \tag{3.9}$$

Here a denotes the number of TaS_2 unit cells as nearest neighbors and b the number of MoS_2 units cells as nearest neighbors. This average speed is then calculated for every vacancy in the list and subsequently used to make a weighted random choice of the next vacancy to move. The chance c_{i} for each vacancy to be chosen is therefore

$$c_{\mathrm{j}} = \frac{D_{\mathrm{average,i}}}{\sum_i D_{\mathrm{average,j}}}. \tag{3.10}$$

3.4.2 Movement of the Vacancy

A chosen vacany not located at the edge of the plane can switch with one of its six nearest neighbors. Due to the structure of the plane and the resulting indexing of the nearest neighbors, it has to be differentiated between two options for this type of movement, depending on the location of the vacancy in either an even numbered or odd numbered row (indexing starts at 0). Figure 3.4 shows the two options for general movement. In an even numbered row m, a vacancy located at

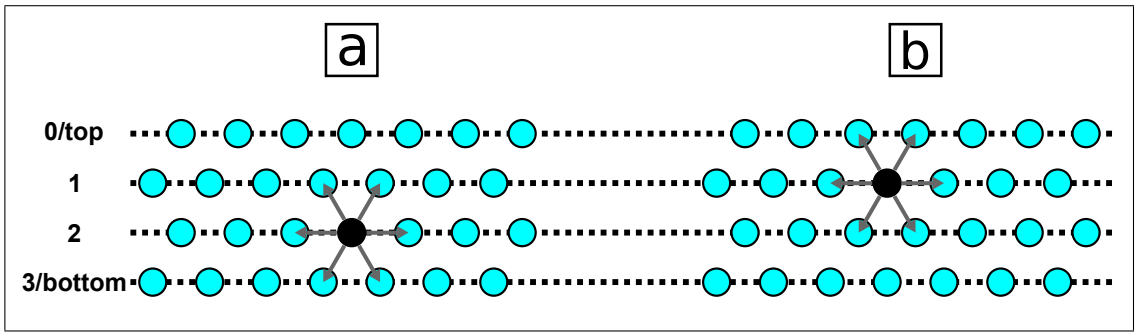


Figure 3.4: Schematic of movement options for vacancies in the simulated plane. Possible positions in blue, vacancy in black. Movement options as gray arrows. The rows are indexed on the left and a dashed line is given as visual aid for the index. a) Movement options for a vacancy in an even numbered row with position that does not trigger a boundary condition; b) Movement options for a vacancy in an uneven numbered row with position that does not trigger a boundary condition.

the coordinates (m, n) can move to: $(m-1, n)$, $(m-1, n+1)$, $(m, n-1)$, $(m, n+1)$, $(m+1, n)$, $(m+1, n+1)$. In an odd numbered row m, a vacancy located at the coordinates (m, n) can move to: $(m-1, n-1)$, $(m-1, n)$, $(m, n-1)$, $(m, n+1)$, $(m+1, n-1)$, $(m+1, n)$.

3.4.3 Periodic boundary conditions

A core principle of this type of simulation are the boundary conditions. Since the rules above only apply to the movement of vacancy which is not at any edge of the simulated plane, it has to be established what happens if one of the vacancies reaches said edge and tries to move off it. This is solved by implementing periodic

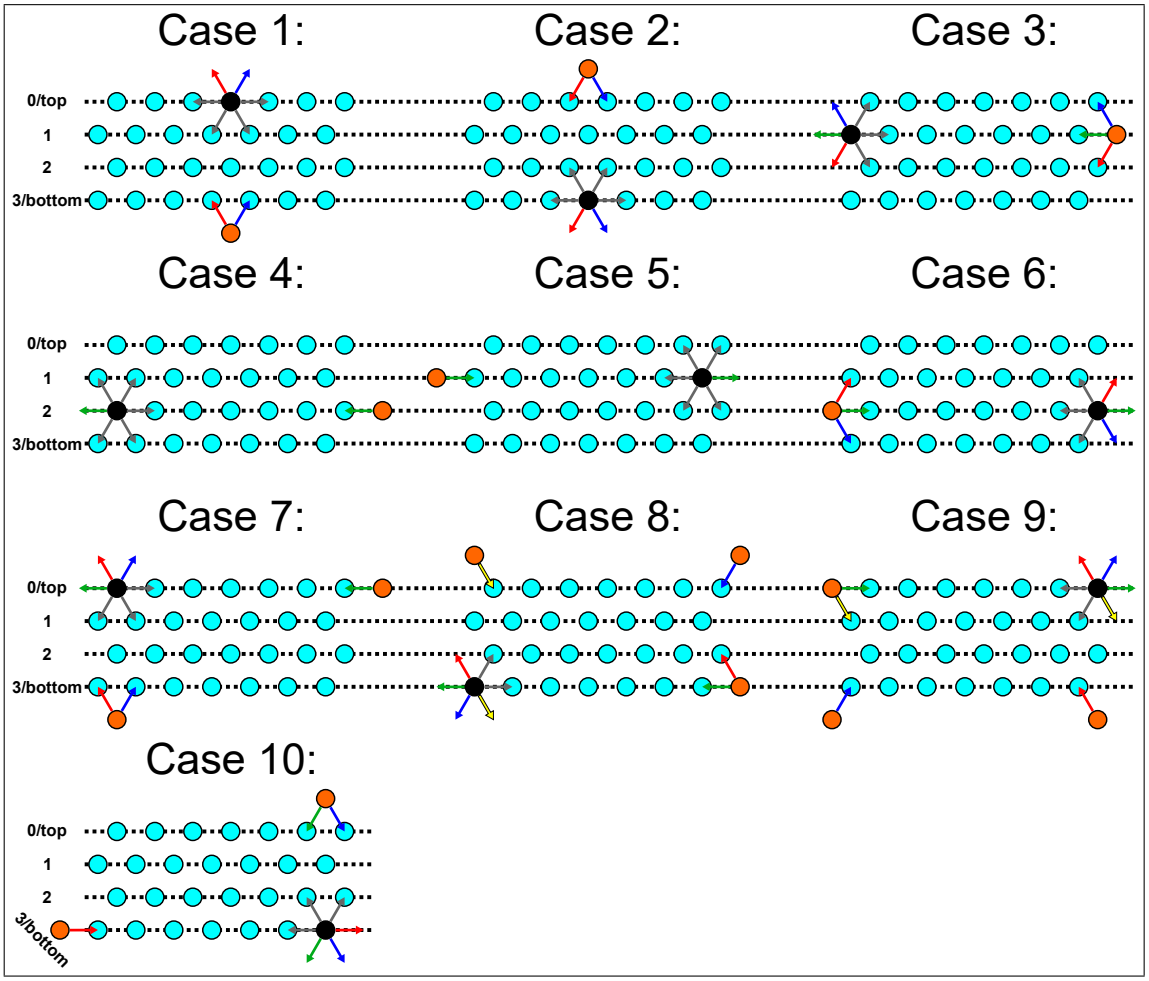


Figure 3.5: Generalized cases of periodic boundary conditions. Black marks a vacancy, blue a position in the plane other than the vacancy, orange a virtual position to simulate an extension of the plane as a visual aid. Grey arrows show movement without triggering a periodic boundary condition and colored arrows show a movement utilizing a periodic boundary condition. A detailed explanation of the cases is given in the text.

boundary conditions. A vacancy exiting on one side will reenter on the adjacent position on the other side of the plane, ensuring no vacancy is lost. Due to the structure of the plane, ten types of cases arise. These can be seen in figure 3.5. Vacancies are colored in black, while the other positions on the plane are shown in light blue. The possible avenues of movements for each vacancy are marked with

arrows. Light gray arrows show movements without triggering periodic boundary conditions and colored arrows show movement, that triggers a periodic boundary condition. As a visual aid, whenever a vacancy would exit the plane and re-enter from the other side, an a virtual position is inserted in orange on the opposing side, as if the plane would continue there. From this virtual position the colored arrows, which show the exit direction of the vacancy, are continued to show the according re-entry direction. To keep description in line with the structure of the python programming language, the top row of the plane is row zero and therefore even.

The following summarizes the boundary conditions that can be triggered for every case but to eliminate unnecessary repetition the normal movements are not explained again.

Case 1 shows a vacancy in the top row of the plane but not on any of the edges of the plane. It can exit to the top left and the top right and will re-enter on the last row of the plane.

Case 2 shows a vacancy at the bottom row of the plane and not in any of the corners of the plane. It can exit to the bottom left or the bottom right and will re-enter on the top row of the plane.

Case 3 shows a vacancy in an odd row (row #1) and on the leftmost position. This vacancy can leave to the left, the top left or the bottom left and will re-enter on the rightmost position of the same row, the one above, or the row below.

Case 4 shows a vacancy in an even row (row #2) and on the leftmost position. It can only exit to the left and will re-enter on the rightmost position of the same row.

Case 5 shows a vacancy in an odd row and on the rightmost position. It can only exit to the right and will re-enter on the leftmost position of the same row.

Case 6 shows a vacancy in an even row and on the rightmost position. It can exit to the top right, the right and the bottom right. It will re-enter on the leftmost position of the same row, the one above, or the one below.

Case 7 has a vacancy in the top row and on the left edge of the row. This vacancy can either exit to the left, where it will re-enter on the very right, or it can exit to the top, making it re-enter on the bottom.

Case 8 shows a vacancy in the last row of the plane and on the leftmost position. This vacancy can exit to the left or top left, re-entering on the rightmost position of the last row or the rightmost position of the second to last row. It can exit to the bottom left, re-entering on the rightmost position of the top row. Lastly, it can exit to the bottom right, re-entering on the leftmost position of the top row.

Case 9 shows a vacancy in the top row on the rightmost position. It can exit to the right or bottom right, re-entering on the leftmost position of either the top row or the row beneath it. The vacancy can exit to the top right, re-entering on the leftmost position of the last row. Lastly, it can exit to the top left, re-entering on the rightmost position of the last row.

Case 10 shows a vacancy in the last row and on the rightmost position. It can exit to the right and re-enter on the leftmost position of the last row, or it can exit to the bottom right or bottom left, re-entering on the last and second to last position of the top row.

3.5 Finite Elements and Empirical Potentials Simulation

Two types of simulations have been used in chapter 4.1 to analyze the distortion effects within CLHs. These are a finite elements simulation and an empirical potentials simulations. This chapter will summarize the two.

3.5.1 Finite Elements Simulations

The finite elements simulation has been done with COMSOL Multiphysics® ver. 6.0 [92] and was graciously provided by Daniel Sahm of the Institute of Metallurgy and Technical Physics in Engineering of University Siegen. As a basis for the simulation, a triangular reference plate has been created, consisting of two sections. An hexagonal area in the middle with a width of 6.64 nm, surrounded by an envelope forming it into a isosceles triangle, with a side length of 14.7 nm. The height of the material is set at 0.617 nm. This shape was chosen to approximate an average CLHs. A schematic of this shape is shown in figure 3.6.

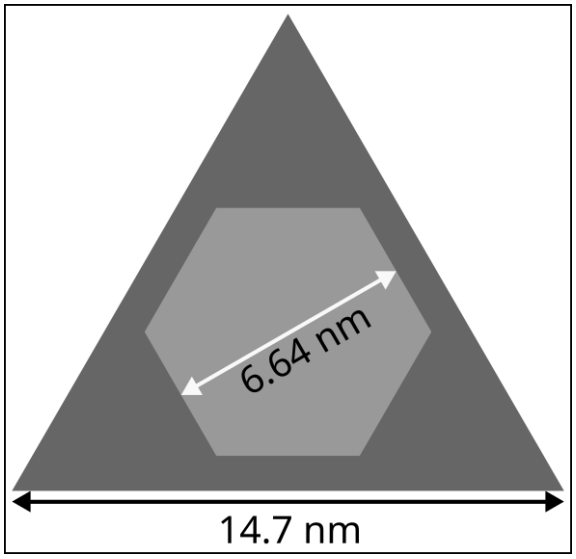


Figure 3.6: Schematic of the starting dimensions used in the finite elements simulations to analyze mechanical deformations. The inner diameter of the hexagon is chosen to be 6.64 nm and the side lengths of the isosceles triangle are chosen at 14.7 nm. These dimensions approximate a typical CLH.

A starting lattice constant of 0.3157 nm is chosen for the whole structure. To facilitate a mismatch, thermal energy is applied to the outer shell. The amount of energy applied equals the energy needed to increase the lattice constant of a filled triangle with the same area as the shell from 0.3157 nm to 0.3300 nm. This is done to simulate the mismatch which is present between MoS_2 and TaS_2 monolayers in their respective equilibrium state. The change in lattice constant has been determined by the change in side length of this reference triangle. An illustration of this can be seen in figure 3.7. The results of the finite elements simulations

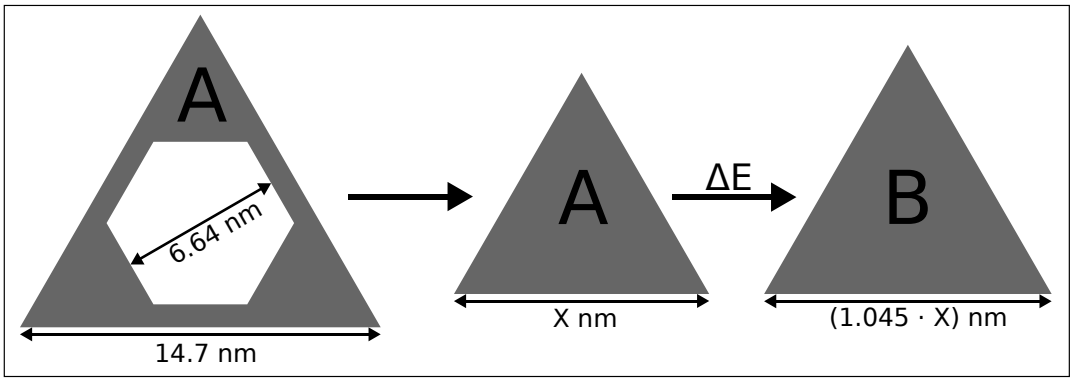


Figure 3.7: Schematic illustration of how the energy for the deformation was chosen. A triangle with area A equaling the area of the shell from the construction in fig 3.6 is deformed until its lattice constant, represented by its side length, has been increased by 4.5%, equaling the mismatch between freestanding MoS_2 and freestanding TaS_2.

is a strained CLHs, as can be seen in figure 3.8. There, the individual atoms are marked by colored spheres after the deformation. The colors represent the amount of dislocation an individual atom has received in nanometers. The results of this simulation have been evaluated the same way as the experimental data which is presented in figure 4.4. To exemplify the measurement process figure 3.8 similarly shows example areas of measurement on the simulated TaS_2 envelope of the triangle (blue box), and the simulated MoS_2 core (red box), together with the measurement directions away from the respective interfaces. A black hexagon marks the original borders of the hexagonal core. One CLHs and its three Mo-S and three S-Ta interfaces have been measured. The results of this measurement are indicated in figure 4.4 b), by the purple dots.

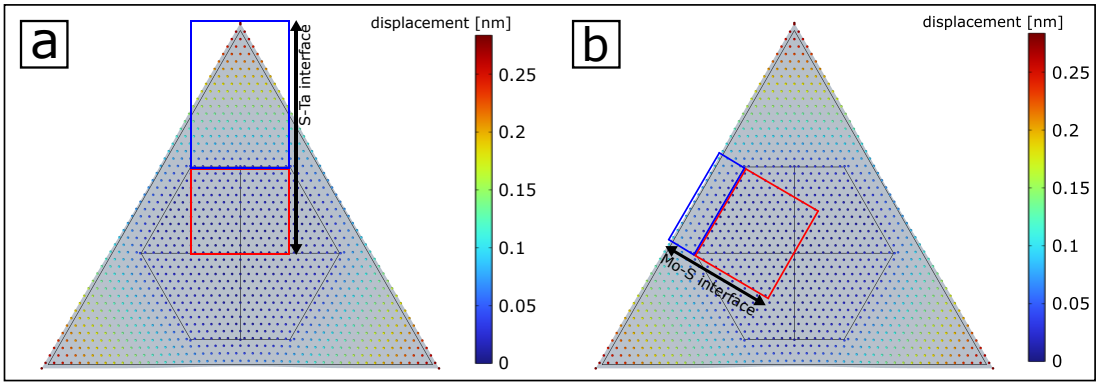


Figure 3.8: a) Finite elements simulation of strained CLH, with panels marking areas of lattice constant measurement parallel to S-Ta interface, the dots represent shifted positions of the atoms in the top layer and are colored according to their net displacement; b) as in a) but for Mo-S interface.

3.5.2 Empirical Potentials Simulations

All empirical potentials simulations have been provided by Mahdi Ghorbani-Asl and Arkady V. Krasheninnikov of the Institute of Ion Beam Physics and Materials Research of the Helmholtz-Zentrum Dresden-Rossendorf. This section shall summarize their structure as published in [68] to give context to the results presented in chapter 4.1.

The simulations use the LAAMPS package [93] as well as Stillinger-Weber empirical potentials. From these potentials lattice constants for extended individual sheets of MoS_2 and TaS_2 were gained, resulting in $a^{EP}_{MoS_2} = 0.3117$ nm and $a^{EP}_{TaS_2} = 0.3315$ nm, which were also used as a basis for the calculations in the CLH. Their validity for usage to describe the TaS_2-MoS_2 interface energy in a CLHs was validated by comparing the results of energy penalty versus interface width to results achieved by DFT calculations in [94], where a good agreement was found. To further optimize the structures, the non-linear conjugate gradient energy minimization method was used. To facilitate the simulations an atomistic model of a CLH was created. This model uses a triangular supercell of 3577 atoms, with dimensions of 15.7 nm × 15.7 nm, to mimic the CLH shown in figure 4.4 a). This structure is consists of a hexagonal core with a side length of eleven unit cells and an envelope with 47 unit cells. The whole model is created at the lattice constant of MoS_2 yielded from the Stillinger-Weber empirical potentials, applying compressive strain on the TaS_2 envelope. The model is then allowed to relax. To mimic the substrate effect on the structure during the process, the z-coordinate of the force on all atoms is set to zero during the energy minimization, while only the components of force inside the x-y-plane are allowed to relax. For ease of analysis, data gained from the empirical potentials simulations is normalized, as to fit the equilibrium lattice constant of the experiment according to $a_{TMDC} = 0.722 \times a^{EP}_{TMDC} + 0.0906$ nm. The visualizations shown in figure 4.6 have been performed using the Open Visualization Tool (OVITO) [95].

CHAPTER 4

RESULTS AND DISCUSSION

4.1 MoS_2-TaS_2 Concentric Lateral Heterostructures

With well established growth processes for MoS_2 [17, 96] and TaS_2 [97, 98] on Au(111), as well as many investigations into structure and modification of these materials [40, 65], the logical next step to increase system complexity is the formation of heterostructures. Two options arise: Out-of-plane heterostructures and in-plane heterostructures. Many publications focus on combining materials out of plane to form layered heterostructures [99, 100, 101], while the formation of in-plane heterostructures and their complicated interactions, however, has gotten less attention.

The following chapter focuses on the preparation and analysis of in-plane heterostructures formed by MoS_2 and TaS_2 on Au(111), in the form of CLH (see chapter 2.6.1 for a formal definition of the concept), especially detailing the behavior at the interfaces where the two materials meet. This chapter is in reference to and expands on the work published in 2D Materials [68].

4.1.1 Preparation and Resulting Structures

For the purpose of ease of access and reproduction of the experiments, this section will provide a general summary of the growth recipes before presenting the resulting structures.

To prepare the CLHs, the cyclical process developed in [26] and described in chapter 3.2 has been applied. The cyclical growth process was applied in its base form. Two cycles were used to grow the CLHs. In the first cycle Mo was evaporated with the sample at room temperature at a rate of 0.007 ML/min, determined by the area covered by MoS_2 after preparation. The time of evaporation could be varied to increase or decrease the size and number of MoS_2 islands present on the sample after preparation (see also [17]). Evaporation times between (5-30) min where

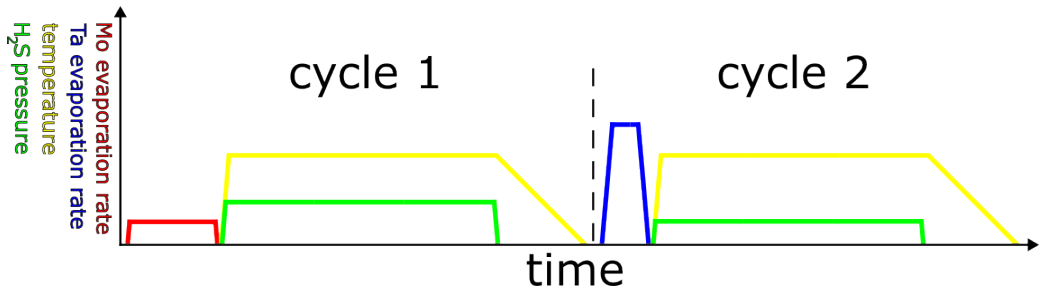


Figure 4.1: Schematic of active preparation parameters over time: Evaporation of Mo (red); evaporation of Ta (blue); presence of H_2S (green), temperature (yellow).

Table 4.1: Preparation parameters resulting in CLHs.

	Mo	Ta
T_{evap}	300 K	300 K
t_{evap}	(5-30) min	(40-180) s
R_{evap}	0.007 ML/min	0.115 ML/min
T_{anneal}	900 K	900 K
t_{anneal}	20 min	20 min
$P_{H_2S,\ anneal}$	$1 \cdot 10^{-5}$ mbar	$1 \cdot 10^{-6}$ mbar

used. This was then followed by annealing in an H_2S atmosphere with a pressure of 1×10^{-5} mbar and at a temperature of 900 K, for a time of 20 min. Afterwards, the sample was cooled down, while the pressure of the H_2S was maintained. At a temperature of 450 K the H_2S flow was stopped and the cooling was continued until RT was reached. This first cycle created MoS_2 islands on the surface.
The process was then repeated with the MoS_2 islands still present on the sample. In the second cycle Ta was evaporated at 0.115 ML/min. Its evaporation time was set, dependent on the desired size and shape of the envelope of the CLH, between (40-180) s. The sample was then annealed in an H_2 pressure of 1×10^{-6} mbar at 900 K. Afterwards it was cooled down and the H_2S supply was stopped at 450 K. While this route presents the Mo and Ta to be evaporated before the H_2S was added, tests have concluded that evaporating while H_2S was already present had no impact, as long as the evaporation takes place at RT. The active process parameters over time are shown in figure 4.1. Additionally, a summary of those parameters is shown in table 4.1 for quick reference.

Figure 4.2 a) shows MoS_2 islands as they would be present after the first cycle of the preparation. These islands are hexagonal or truncated triangular in shape and are located on various terraces of the Au(111) surface. These terraces are of monoatomic height, as has been shown in an earlier work [26] and can be distinguished by the change in brightness of the background behind the islands. All of these terraces exhibit the herringbone reconstruction as described in section 2.3. The sizes of the islands vary within each preparation and range from 5 nm to 50 nm in diameter. On the surface of these islands a repeating pattern can be seen. This pattern is the moiré resulting from the mismatch between the lattice constant of the Au(111) surface and the MoS_2 atop it. The moiré superlattice has a hexagonal structure, as well as the lattice of the Au(111) and the MoS_2 (see chapter 2.7.1). The moiré is aligned with the dense-packed rows of the Au(111), indicating, since MoS_2 also has a hexagonal lattice, that there is no rotation between the lattice of the MoS_2 and the Au(111). Therefore the MoS_2 is also aligned with the dense packed rows of the Au(111). Additionally the edges of the islands are also always parallel to the dense-packed rows of the substrate. On these edges a brightening effect can be seen. This indicates the metallic edge state which has been widely reported for MoS_2 [103, 104].

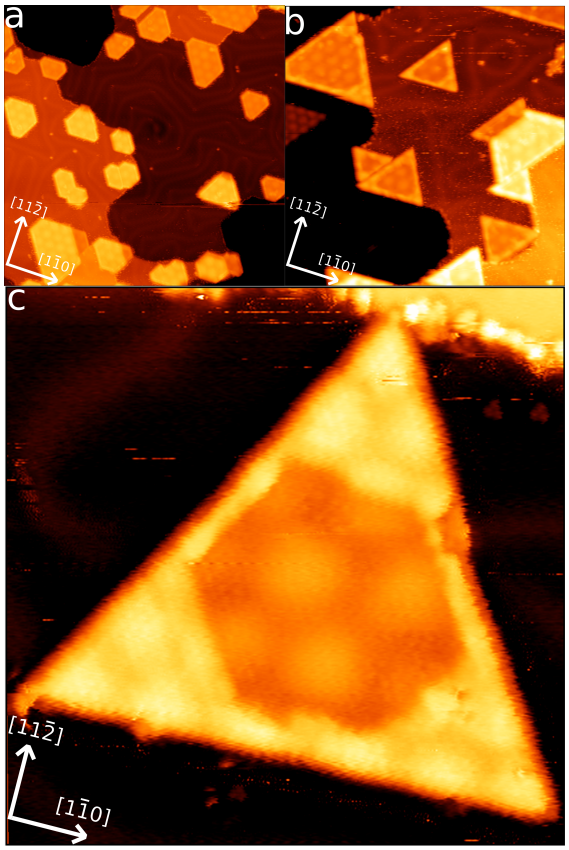


Figure 4.2: a) STM image of MoS_2 islands on a Au(111) surface, $U_{bias} = -1.0$ V, $I = 3 \times 10^{-10}$ A, dimensions: 84 nm × 84 nm; b) Image of MoS_2-TaS_2 CLHs on Au(111) surface, $U_{bias} = -1.0$ V, $I = 3 \times 10^{-10}$ A, dimensions: 46 nm × 46 nm; c) Close up of MoS_2-TaS_2 CLH, $U_{bias} = -1.0$ V, $I = 3 \times 10^{-10}$ A, dimensions: 14.5 nm × 14.5 nm. Modified under Creative Commons Attribution License 4.0 [102] from [68].

Figure 4.2 b) and c) show results after the second cycle has been completed. In figure 4.2 b) a surface similar to a) can be seen. Again multiple terraces of the Au(111) surface and its characteristic herringbone reconstruction are visible. Located on these terraces are islands in form of CLHs consisting of a darker core,

identified as MoS_2 and a brighter envelope, identified as TaS_2, surrounding the core (for a detailed identification process see [26]). The bright envelopes shape the islands into a triangular shape, similar to TaS_2 grown with the same growth parameters and no precursor islands (see [26]). The cores have a hexagonal or truncated triangular structure, similar to the pure MoS_2 islands seen in figure 4.2 a). Figure 4.2 c) shows a close-up of an island where this is exemplified. Here it can be clearly seen that the TaS_2 accumulated in varying amounts to the different edges of the MoS_2 core, forming the whole island into its triangular shape. The majority of the TaS_2 always accumulates at three edges which have a 120° rotation to each other. A typical island has a core with a diameter of 8 nm and a side length of 14 nm. The island exhibits two moiré patterns. One moiré is located on the MoS_2, with a lower periodicity, and the other is located on the TaS_2, with a higher periodicity relative to the one on the MoS_2. Both of the moiré patterns are aligned with the dense-packed rows of the Au(111) surface. The edges of the islands, as well as the interfaces between the MoS_2 and the TaS_2, are parallel to the dense-packed rows of the substrate. Evaluating the interface, it can be seen that there is always a sharp connection between the core and the border and no special electronic signature similar to the edge state of MoS_2 has been found at voltages between -2 V to 2 V. It is of note that no defects have been observed at the interfaces between the MoS_2 cores and the TaS_2 envelopes.

4.1.2 Interface Analysis by Orientation and Distribution of Islands

Chapter 2.5.3 and chapter 2.6.1 have defined two stacking registries, $M_{fcc}X_{top}$ and $M_{hcp}X_{top}$, together with two orientations, (+) and (-), on each an fcc-stacked and hcp-stacked substrate, for both CLHs and singular TMDC monolayers. In the case of CLHs two types of interfaces emerge: The M_{in}-X interface and the X-M_{out} interface. Since asymmetric behavior, like the amount of TaS_2 accumulated during the growth process, has been observed, the determination of the, hitherto unknown, stacking registries and the resulting interface types inside the CLHs are a useful insight. This however is complicated by the fact that an STM only measures the S located in the top layer of the presented TMDC monolayers [17, 62, 105]. Yet, an intricate analysis of the distribution of both pure TMDC islands and CLHs on the two types of stacking exhibited by the Au(111) surface, whilst also taking their orientation into account, can alleviate this problem.

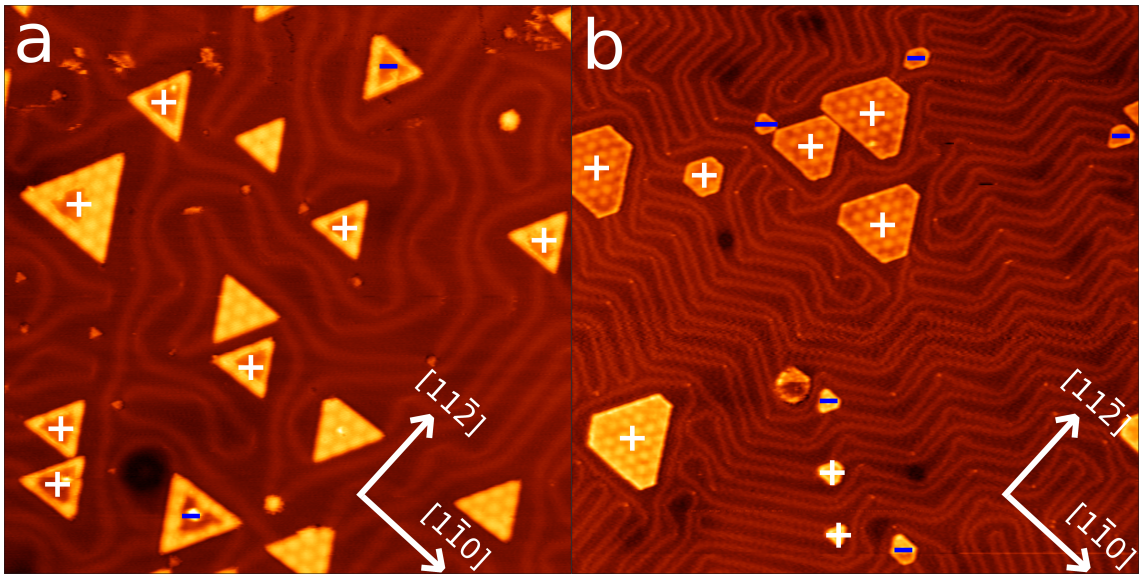


Figure 4.3: STM image of a) MoS_2-TaS_2 CLH on Au(111), $U_{bias} = -0.25$ V, $I = 9{\times}10^{-10}$ A, dimensions: 59 nm × 59 nm; b) MoS_2 islands on Au(111), $U_{bias} = -0.5$ V, $3{\times}10^{-10}$ A, dimensions: 128 nm × 128 nm; Symbols '+' and '-' denote the orientation of the islands, while the stacking of the substrate is indicated by the color white (fcc) and blue (hcp). In *b)*, Fourier-Filtering techniques have been applied to remove a background frequency. Taken under Creative Commons Attribution License 4.0 [106] from [68].

While aspects of the distribution of MoS_2 islands and CLHs between fcc and hcp areas of the Au(111) surface can already be seen in figure 4.2 a) and b), figure 4.3 shows this in more detail. In figure 4.3 a), CLHs, recognizable by the dark

Table 4.2: Distribution (normalized to 1) of each type of structure with a specific combination of their orientation (+/-) and stacking order of the underlying Au(111) substrate (fcc/hcp). Based on datasets of 152 MoS_2 islands and 139 CLHs. Occurances of pure TaS_2 in CLH preparations have been disregarded. Adapted Creative Commons Attribution License 4.0 [107] from [68].

(a) MoS_2-TaS_2 CLHs

	(+)	(-)	sum
fcc	0.73	0.09	**0.82**
hcp	0.01	0.18	**0.19**
sum	**0.74**	**0.27**	

(b) MoS_2 islands

	(+)	(-)	sum
fcc	0.63	0.08	**0.71**
hcp	0.11	0.19	**0.30**
sum	**0.74**	**0.27**	

core and the bright envelope surrounding them, are shown on a single terrace of Au(111). Some islands of pure TaS_2 are also present. The orientations of the CLHs, according to the definitions in chapter 2.6.1, are marked by either a (+) or a (-). The color of the sign marking them distinguishes if the island is located in an fcc or hcp area, with fcc marked in white and hcp marked in blue.
Figure 4.3 b) shows MoS_2 islands, grown with parameters of the first cycle of the CLH preparation in a), with analogue markings which were done here according to the definitions in chapter 2.5.3. It can already be seen that in both images the islands heavily prefer growing in the fcc areas of surface. This happens to such an extend that the islands even distort the herringbone lines, which are prevalently visible in the background of both images.

The results of a distribution analysis can be seen in table 4.2.
In the case of CLHs 82 % of the islands are located in the fcc areas and 19 % are located in the hcp areas of the substrate. Therefore the islands heavily favor the fcc areas of the substrate. Moreover, 73 % of the islands are located in the fcc areas and have the (+)-orientation, while only 9 % are located in the fcc areas and have the (-)-orientation. It is very clear that the (+)-orientation dominates heavily in the fcc areas. Inversely only 1 % of the islands are located in the hcp areas of the surface and have the (+)-orientation, while 18 % have the (-)-orientation and are located in the hcp areas, showing that islands in the hcp areas heavily favor the (-)-orientation. In total 74 % of the counted islands have the (+)-orientation and 27 % islands have the (-)-orientation. This however is heavily skewed by the number of islands located in the fcc areas.

The picture presented by the CLHs is mirrored by the pure MoS_2 islands. Here 71 % of the islands are located in the fcc areas and 30 % are located in the hcp areas. Of all islands 63 % are located in the fcc areas and have the (+)-orientation, while 8 % have have the (-)-orientation. The share of all islands in the hcp areas, with the (+)-orientation is 11 % and with the (-)-orientation 19 %. Overall 74 % of the islands exhibit the (+)-orientation and 19 % the (-)-orientation.

As mentioned earlier the distributions of the CLHs and MoS_2 islands between the two areas of stacking is very similar. In both cases the fcc areas are heavily favored as a location. Within these fcc areas the (+)-orientation dominates, for both CLHs and pure MoS_2 islands. The opposite picture is the case in the hcp areas. Here, for both CLHs and MoS_2 the (-)-orientation is more prevalent. This switch in orientation between the two areas is quite logical if a certain orientation has an energetical preference in reference to the stacking of the first two layers of the substrate, since the fcc and hcp areas are the same in that regard, except for a 180° rotation (see chapter 2.3).

In summary it can be concluded that the distribution of orientations of MoS_2 islands between fcc and hcp areas of the Au(111) substrate, grown with the same growth parameters as were present during the first cycle of a preparation of CLHs, is equal to the distribution of said CLHs between the two areas. There is no indication that the registry of the MoS_2 islands with the substrate changes when TaS_2 is added in the second growth cycle, as this would need a whole restructuring of the island and likely facilitate secondary effects like intermixing, which are not observed. This is further supported by the fact that experiments in the past have shown that TaS_2 shares the distributions and orientations of MoS_2 and CLHs between the fcc- and hcp-stacked areas of the Au(111), while DFT calculations also indicated that it likely shared their preferred registries [65]. Therefore the edge terminations of the MoS_2 can be used to determine the interface types inside the CLHs.

As stated earlier, the two possible interface types are the M_{in}-X interface and the X-M_{out} interface, defined by the material that contributes the metal atom to the metal-chalcogen bond which is crossing the interface. Either the TMDC in the core on the inside contributes the metal atom (M_{in}-X) or it is contributed by the TMDC creating the envelope surrounding the core (X-M_{out}). The location of these interfaces inside a CLH are dependent on its stacking registry, which in turn also determines the edge termination of the whole CLH. However, the orientation of

a CLH and the stacking of the underlying substrate are not enough to determine the stacking registry of the heterostructure, as there are two stacking registries for each orientation (see figure 2.14). Here the stacking registry of pure MoS_2 together with the distribution analysis can lend a hand.

While a similar problem would arise for perfectly symmetrical MoS_2 islands, a preference for an edge termination exists, distorting the islands [108]. According to theoretical and experimental analysis including access to S during the growth process, the shorter edges tend to terminate in S and the longer edges tend to terminate in Mo [109, 103, 110, 111]. Comparing this information with figure 2.11 shows that the (+)-orientation on an fcc-stacked substrate and the (-)-orientation on hcp-stacked substrate, which are the orientations that dominate these substrate stacking orders in the distribution analysis, translate to the $M_{fcc}X_{top}$ stacking registry.

Since the distribution of the MoS_2 islands between the fcc and hcp areas of the substrate, together with the preferred orientation of the islands on these two switching in concordance with the 180° rotation of the two areas, is retained for CLHs (see table 4.2), it is safe to assume that the stacking registry of the MoS_2 is retained, too. As the interface between the MoS_2 core and the TaS_2 envelope is defect free, the stacking registry has to carry over to the TaS_2, as well. This clearly determines the edge terminations of the CLHs, as can be seen in figure 2.11. Triangular CLHs in $M_{fcc}X_{top}$ stacking geometrically terminate with long metal edges and short chalcogen tips in the (+)-orientation on an fcc-stacked substrate, as they do in the (-)-orientation on an hcp-stacked substrate. This shows that the TaS_2 prefers the metal edge, which might indicate that this preference carries over to pure TaS_2 islands as predicted in [65].

Additionally, this clearly identifies the interface types that present inside these CLHs. The CLHs exhibit an X-M_{out} interface for all interfaces parallel to the sulfur edges of the CLHs and M_{in}-X interfaces at all interfaces parallel to the metal edges. Here this means that in the triangular islands, in $M_{fcc}X_{top}$ registry with an fcc substrate, the three X-M_{out} interfaces are located firstly at the topmost-edge of the MoS_2 core in $[1\,1\,\bar{2}]$ direction, secondly at 120° rotated to the first, and the third at 240° rotated to the first one. The remaining three interfaces, located at 60°, 180°, and 300° rotations of the topmost interface are of the M_{in}-X type. This also concludes that the TaS_2 shows a preference to accumulate material at the chalcogen edges of the MoS_2.

4.1.3 Interconnection at the Interface

The results of the previous chapter give an insight into the interface types and edge terminations of the CLHs. It has already been observed that the interface type has an influence on the growth morphology of the islands. Moreover, the earlier analysis is based on the already mentioned observation that the interface between the two materials is defect free. This observation, however, raises another question. An interface between two materials of differing lattice constant needs a mechanism to compensate their mismatch in order to facilitate a connection. As defined in chapter 2.4 the mismatch between two materials can be defined as:

$$f = \frac{a_1 - a_2}{a_1}. \tag{4.1}$$

For MoS_2 monolayers with a lattice constant of a_{TaS_2} = (0.3300 $\pm$ 0.001) nm [40] and TaS_2 monolayers with a lattice constant of a_{MoS_2} = (0.3157 $\pm$ 0.0003) nm [64], both on an Au(111) substrate, the mismatch approximates to $f \approx 4.53\%$. Usually, such a mismatch can be compensated by the introduction of a defect. This case would call for one missing row every 21 rows of connection. The corresponding critical layer thickness has been determined by DFT in one of our publications to be 0.3201 nm [94]. However, no defects, even beyond this critical layer thickness, have been observed at the interfaces of the CLHs. Therefore, another mismatch compensation mechanism needs to be present. Usually, this is strain, expressed through compression or stretching of one or deformation of both of the interconnected materials. Major distortion effects of this type have been observed by STM measurements in the TaS_2 envelope surrounding the MoS_2 core, together with a slight extension of the MoS_2 core, which will be summarized in this section.

Figure 4.4 a) shows an example island. The atomic rows are continuous, independent of the interface is investigated. To quantize the strain effect taking place, the lattice constants of the MoS_2 and TaS_2 have been measured parallel to the interface, atomic row by atomic row. As an illustration of the measurement process an X-M_{out} interface and an M_{in}-X interface (with an MoS_2 core and a TaS_2 envelope, resulting in an Mo-S interface and an S-Ta interface) have been highlighted. A dotted white line marks the measurement direction of the lattice constant. To gain one data point the lattice constants over multiple atoms in one row have been averaged. The white arrow indicates the direction of these measurements movement away from the interface of the two materials. Red boxes indicate areas

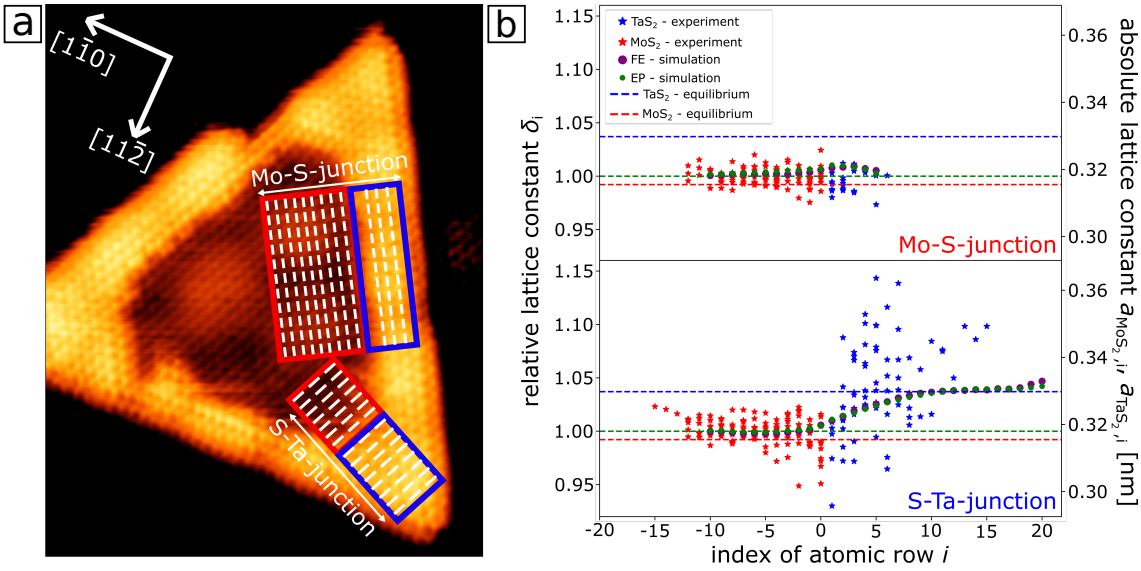


Figure 4.4: a) Atomically resolved STM image of a triangular MoS_2-TaS_2 CLH on Au(111), U_{bias} = -0.9 V, $I = 1 \times 10^{-12}$ A, dimensions: 12.5 nm × 15.8 nm; b) Graph with relative (left scale) and absolute (right scale) lattice constants measured parallel to the heterointerface as indicated by white dashed lines in panel *a)* of several Mo-S interfaces (top) and S-Ta interfaces (bottom), on several different islands (two examples labelled in panel *a)*). Red symbols denote MoS_2, blue symbols denote TaS_2, see also corresponding boxes in panel *a)*. Blue / red dashed lines represent the equilibrium lattice constant of the constituents, see text. Green circles: empirical potential calculations (normalized, see text). Purple circles: finite element simulations. Modified under Creative Commons Attribution License 4.0 [112] from [68].

of measurements on the MoS_2 core, while blue boxes mark measurement areas on the TaS_2 envelope. Figure 4.4 b) shows the results of these measurements. Data has been acquired from 22 different interfaces, on six different CLHs.

The upper graph of figure 4.4 b) shows the lattice constant parallel to the Mo-S interfaces and the lower graph parallel to the S-Ta interfaces. Red data points indicate measured lattice constants on an MoS_2 core and blue data points on the TaS_2 envelope. Purple data points indicate results from a finite-elements simulation made with COMSOL Multiphysics® ver. 6.0 [92]. Green data points indicate results gained from an empirical potentials simulation. Detailed information on these two simulations are given in chapter 3.5. A red dashed line marks the expected value for the MoS_2 lattice constant, in a relaxed, equilibrium state, while a blue dashed line indicates the equilibrium lattice constant for TaS_2. The left y-axis denotes the relative lattice constant δ_i. In an ideal case, deformations in the two materials would be measured by STM directly. Acquiring comparable

data however, can be intensely difficult due to effects like thermal drift and piezo creep. Calibration of the images to a known structure requires the presence of such structures, for example a visible stretch of Au(111) surface in atomic resolution. This is not always the case. Procedures to calculate the lattice constant from the moiré reconstruction ideally also involve multiple supercells and due to the size of the CLHs only very few are present on the MoS_2 cores and often none at all on the TaS_2 envelopes. However, an appropriate normalization scheme can still give insight about the relative strains acquired by the two materials and even relate it to the absolute lattice constants of the two materials.

To achieve this, all data is normalized to the average of the MoS_2 lattice constant of each respective TaS_2-MoS_2 measurement set. This should minimize measurement errors due to varying distortions for differing islands. The normalization can be summarized as follows:

$$\forall \delta \in P_{MoS_2} \; ; \; \delta_i = \frac{a_{MoS_2,i}}{\frac{\sum_{j=1}^{n} a_{MoS_2,j}}{n}} \tag{4.2}$$

and

$$\forall \delta \in P_{TaS_2} \; ; \; \delta_i = \frac{a_{TaS_2,i}}{\frac{\sum_{j=1}^{n} a_{MoS_2,j}}{n}}. \tag{4.3}$$

Here δ denotes a data point of one measurement set. This point can either be acquired from the group of points measured on MoS_2 or TaS_2 (P_{MoS_2} or P_{TaS_2}). These points are always measured along one direction of one CLH. Here $a_{MoS_2,j}$ and $a_{TaS_2,j}$ define a singular instance of a measured lattice constant on either MoS_2 or TaS_2, with n being the number of all measured lattice constants on MoS_2 from this set.

To relate the relative lattice constant δ_i to the absolute lattice constants $a_{MoS_2,j}$ and $a_{TaS_2,i}$, the MoS_2 cores were used. Since the cores are still large enough to contain some supercells (see figure 4.4 a)) an average MoS_2 unit cell count, by averaging over all three symmetry directions from multiple cores, has been acquired. This results in (9.7 $\pm$ 0.5) unit cells, with the standard deviation as the error. This translates to an average lattice constant, by use of moiré analysis according to [113], of $\overline{a}_{MoS_2}$ = (0.318 $\pm$ 0.002) nm. This result is bigger than the results measured on pure MoS_2 islands by Silva et al. [64], resulting in (10.6 $\pm$ 0.1) MoS_2 unit cells per supercell, translating to $\overline{a}_{MoS_2}$ = (0.3157 $\pm$ 0.0003) nm. Therefore the core has on average expanded by $\sim$0.7% compared to pure MoS_2

islands on Au(111). This is easily explained by tensile stress applied to the MoS_2 core due to coherently bonding with the TaS_2 envelope, which has a significantly larger lattice constant in its relaxed state. The average calculated from the MoS_2 cores by moiré analysis is used to link the relative expansion to the absolute lattice constants shown on the right x-axis in figure 4.4 b). A green line links the relative lattice constants δ = 1.00 to the absolute lattice constant a = 0.318 nm. Each relative change is therefore linked to the corresponding change in absolute lattice constant.

It is quickly apparent that the materials have undergone varying amounts of changes. The analysis of the MoS_2 lattice constants shows, that with distance to both types of interfaces, the results hover around the 1.00 line and no systematic change can be seen, only the isotropic expansion of the lattice constant. The TaS_2 tells a different story. Varying results emerge for the Mo-S and the S-Ta interfaces. In the case of the Mo-S interfaces, the TaS_2 lattice constant constricts itself to match the MoS_2 core. To achieve this, the material undergoes a contraction of $\approx$3.6 %. In the case of the Mo-S interfaces this contraction is present until the edge of the island is reached. For the S-Ta interfaces, the TaS_2 also constricts itself to match the MoS_2 core but does expand again with increasing distance to the interface. It is noteworthy however, that this expansion does not stop when the equilibrium lattice constant of TaS_2 is reached but continues even to values of 10% and higher than the equilibrium lattice constant, suggesting possible influence from the strain at the other edges or substrate interactions.

4.1.4 Lattice Constant of TaS_2/Au(111)

To exclude the possibility that the deformations are an effect usually occurring in triangular TaS_2 islands, especially towards the tips of the islands, pure TaS_2 islands have been analyzed as well. The results can be seen in figure 4.5.

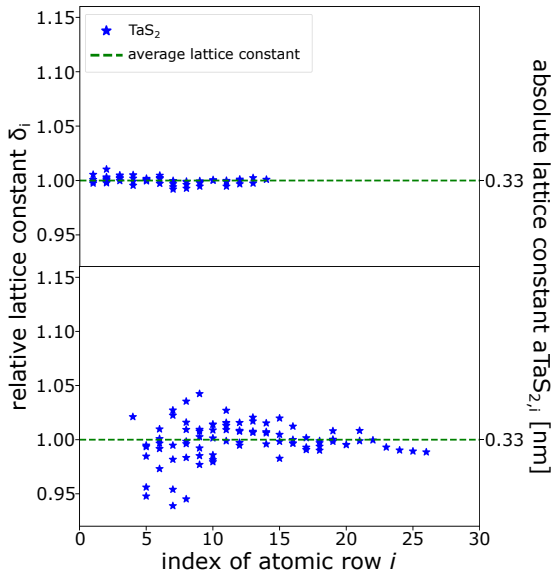


Figure 4.5: Graph with relative (left scale) and absolute (right scale) lattice constants, measured parallel to the two types of edges proposed for TaS_2. A green line indicates the average of each measurement, which corresponds to the TaS_2 lattice constant. Top: Measurement with distance to the metal edge; Bottom: Measurement with distance to the chalcogen edge.

Similar to figure 4.4 b), two directions have been measured on several islands and a similar scheme of normalization has been applied. Instead of normalizing to the average lattice constant of MoS_2, since none is present, a measurement set is normalized to its average TaS_2 lattice constant, which is just the measurement set. This shortens the normalizations seen in 4.2 and 4.3 to:

$$\delta_i = \frac{a_{TaS_2,i}}{\frac{\sum_{j=1}^{n} a_{TaS_2,j}}{n}}. \tag{4.4}$$

As a pure TaS_2 island has no interfaces with another material, the lattice constants are not measured with distance from said interface but distance from an island's respective edge. The upper plot in figure 4.5 shows the measurements starting at a metal edge of the TaS_2, then moving towards the middle of the islands and the lower plot shows measurements starting at a chalcogen tip of the TaS_2 and then moving towards the middle of the islands. The behavior in both directions is the same. No significant variation of the lattice constants was measured. All data is clustered, as expected, closely around its own average, which has been assumed to correspond to a_{TaS_2} = (0.33 ± 0.001) nm (see [40]). No systematic trend can be discerned. The expansion of the range of the data's clustering, in the case of the chalcogen edges, close to the edge of these islands, is easily explained by the increased measurement error, as the amount of lattice periodicities present in the tip, which can be averaged over, is reduced the closer

one measures to the end of the island.

In summary no systematic trend is discernible for both chalcogen and metal edges. This indicates that the trends within CLHs, shown in figure 4.4 b), are not a natural effect of the formation of triangular islands by TaS_2.

4.1.5 Deformation Simulations

As seen in figure 4.4 b), there is a stark difference between the deformation behaviors at the Mo-S interfaces and the S-Ta interfaces. Especially the distortions at the S-Ta interfaces are extraordinary and not present in pure TaS_2 islands. Here the experimental data shows that the TaS_2 in the tips of the triangular islands expands its lattice constant to over 10 % in relation to the lattice constant in the MoS_2 core. The cause of these deformations is of great interest. An instinctual

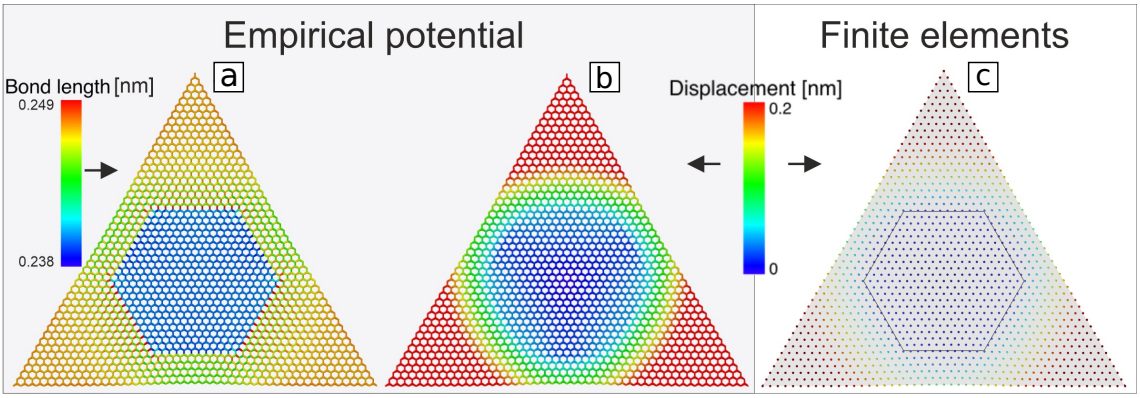


Figure 4.6: Structure of a relaxed concentric lateral heterostructure using empirical potentials calculations a)/b), and finite element finite elements simulations c); a) Metal-sulfur bond length, the entirety of the inner blue region aligns precisely with the MoS_2 core; b) Displacement of the atoms during relaxation in the EP calculation; c) Displacement of the unit cells (represented by the metal atoms) during relaxation in the FE simulation. The hexagon indicates the MoS_2 core. Modified under Creative Commons Attribution License 4.0 from [68].

premise would be that these deformations are of mechanical nature, resulting from the stress caused by the mismatch of the TaS_2 and MoS_2. A useful way to investigate mechanical stresses in materials are finite elements simulations, while a more complex approach is the use of an empirical potentials simulations, which takes into account the atomistic bonds [114]. Both of these have been done and this section summarizes and compares the results already shown in figure 4.4 b), while section 3.5 contains an explanation of the basics and structure of the two simulations utilized.

Results for both kinds of simulations are shown in figure 4.6, where a) and b) show results of the empirical potentials simulation and c) shows a result from the finite elements simulation.

Mo-S interfaces

In the case of the Mo-S interfaces, the two types of simulations show a similar behavior to the experimental data. Generally, both the material in the core (representing the MoS_2) and the material of the envelope (representing the TaS_2) have a common lattice constant with almost no internal variation. This lattice constant is aligned with the lattice constant of the slightly expanded MoS_2 core measured in the experiment. A minor variation is observed, as the lattice constant of the MoS_2 seems to slightly increase with closeness to the interface. This increase appears minimally greater after the interface has been crossed to the TaS_2, but then, with increasing distance from the interface, the lattice constant relaxes to the lattice constant of the expanded MoS_2 core. This behavior, while not impossible, cannot be concluded with certainty from the experimental data. The effect is slightly more pronounced in the empirical potentials simulation compared to the finite elements simulation, as the rise in lattice constant is moderately higher before and after the interface has been crossed, while the decay is also more pronounced and faster but generally the two simulations are in agreement.

Ta-S interfaces

The results of the simulations at the S-Ta interfaces are again comparable to the experimental data but with a difference which is more pronounced than for the Mo-S interfaces. The MoS_2 core experiences the same expansion behavior which is observed in the experimental data and almost all the data clusters around this new value. No clear trend can be observed until about three rows removed from the interface. There the lattice constant begins to increase slightly when closing in on the TaS_2 area, with a continued and rising increase on the TaS_2 side of the interface. This increase has also been observed in the experimental data. However, in the experimental data, a significant increase in lattice constant, even beyond the equilibrium lattice constant of TaS_2, is observed with increased distance to the interface. On average, after about five rows, the equilibrium lattice constant of TaS_2, $a_{TaS_2} = 0.33$ nm, has been reached in the experiment but this is only the

case after eleven rows in the simulation. A slight increase of the lattice constant over the equilibrium lattice constant of TaS_2 is observed but only to about 1 %, nowhere near the over 10 % present in the experimental data. These behaviors are observed for both the finite elements simulation and the empirical potentials simulation, with the only notable difference between the two being that the overextension of the lattice constant in the TaS_2 is slightly more pronounced in the empirical potentials simulation than in the finite elements simulation.

Overall, the simulations generally agree with the experimental data and no significant difference is observed between the empirical potentials simulation and the finite elements simulation. This indicates that even a simple mechanical approach (e.g. finite elements) is sufficient to explain most of the deformation present in the CLHs. While the empirical potentials simulation is more detailed, its results also do not fully align with all observations from the experiment. The overextension in the tips of the triangular TaS_2 envelope is indicated and more pronounced than in the finite elements simulations but does not come near the experimental data. While the empirical potentials simulation tries to take the substrate into account by limiting the z-coordinate during the energy minimization process, this cannot fully replace an investigation of substrate interactions and they remain a main contender for this effect. Additionally, electronic effects are not taken into account in both these simulations. These effects could be encompassed by a DFT simulation but, due to the size of the structures, too much computational power would be required to achieve this at the current point in time.

4.1.6 Conclusion

Several interesting questions could be answered when analyzing the behavior at the interfaces between MoS_2 and TaS_2 inside CLHs. It had been established in an earlier work that CLHs between MoS_2 and TaS_2 could be grown, even though a large mismatch of about 4.53 % between the lattice constants of the two materials exist [26]. What had yet to be answered was how this mismatch was compensated. To answer this question, first the types of interfaces inside the CLHs had to be identified. This was achieved through an investigation of the distributions of the CLHs in the fcc and hcp areas of the surface and their orientations within them, which was subsequently compared to the distributions of MoS_2 islands. From this the preferred stacking order was identified as $M_{fcc}X_{top}$ and enabled the identification of the locations of the M_{in}-X and X-M_{out} interfaces inside the CLHs. This also enabled us to identify the edge terminations of the CLHs. Due to the similarity of the CLHs to TaS_2 islands, this might be used as another indicator for the edge terminations of these islands, which is in line with earlier predictions [65]. Moreover a material and interface dependent mismatch compensation has been found, which contradicts defect mediated compensation mechanisms predicted in theory [94]. The MoS_2 cores have been found to only expand little, while the TaS_2 compresses its lattice constant to fit to the MoS_2 at the interface. At the X-M_{out} interface this compression is relaxed with distance to the interface and even turning into an expansion at a significant enough distance. This solves many unanswered questions regarding the growth of CLHs with MoS_2 and TaS_2 and can act as a staging ground for investigations of CLHs with different materials. Yet, TMDC monolayers with two types of metals do not only exist in the separated form of CLHs.

4.2 $Mo_{(1-x)}Ta_xS_2$ alloys

As discussed in the previous chapters, different preparation parameters lead to a wide range of structures forming on the sample. Specifically the temperature, during deposition or the annealing step, the ratio of the metals, and the supply of S via H_2S are of great importance to decide the final result. In chapter 4.1 MoS_2-TaS_2 CLHs have been grown utilizing an annealing temperature of 900 K, which results in a clear separation of the two TMDCs. Theoretical results from Hemmat et al [19] predicted that above 1000 K a stable alloy of $Mo_{(1-x)}Ta_xS_2$ can be achieved in any composition (see figure 4.7). This chapter will present a growth process which results in various amounts of $Mo_{(1-x)}Ta_xS_2$ alloys, whose rates of mixture are in dependence of annealing temperature and analyzes their structures.

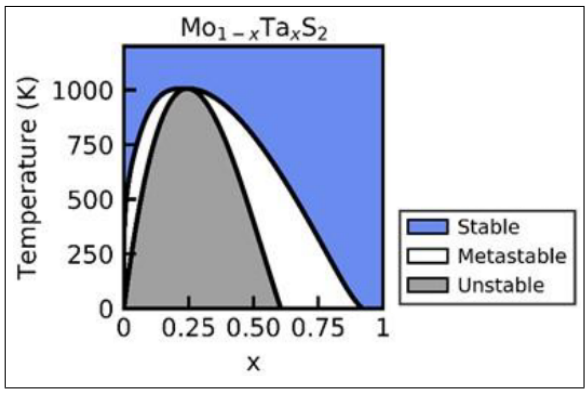


Figure 4.7: Phase diagram of $Mo_{1-x}Ta_xS_2$ alloy in dependence of temperature and metal ratio. Modified with permission from [19].

4.2.1 Preparation and Resulting Structures

Again, for ease of access and reproduction of the findings, the preparation parameters will be summarized first and followed by a description of the resulting structures.

To prepare alloy structures, a variation of the cyclic process from chapter 3.2 was used. In the first cycle MoS_2 was grown by evaporation of Mo at RT with a rate of 0.01 ML/min for 25 min. Following this, the sample was annealed in H_2S at 900 K / 950 K for 20 min. It was then cooled down and when 450 K was reached, the H_2S supply was cut off. This created MoS_2 islands on the surface. Afterwards Ta was evaporated in a second cycle, also at RT, with a rate of 0.06 ML/min, onto the pre-existing MoS_2 islands. This was done for 2 min and then the sample was annealed, depending on the preparation, at (950-1050) K for 20 min. No H_2S was supplied. The parameters of these preparations

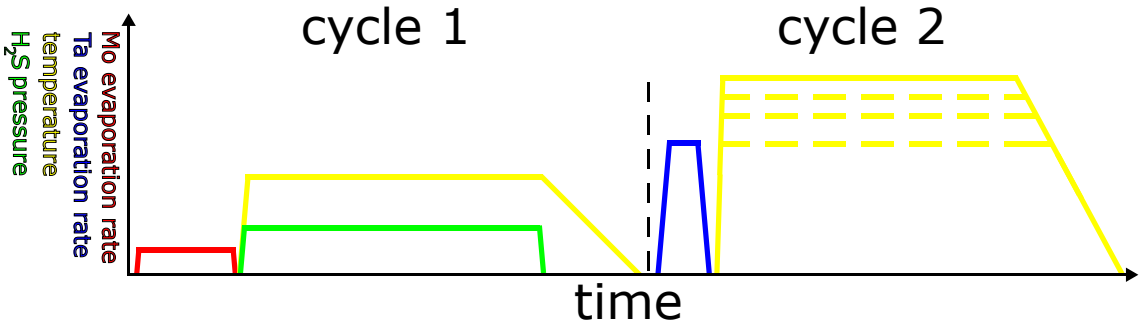


Figure 4.8: Schematic of active preparation parameters over time: Evaporation of Mo (red); evaporation of Ta (blue), presence of H_2S (green), high temperatures (yellow).

Table 4.3: Parameters of preparations which will results in various amounts of alloys.

	Mo	Ta
T_{evap}	300 K	300 K
t_{evap}	25 min	2 min
R_{evap}	0.01 ML/min	0.06 ML/min
T_{anneal}	900 K/950 K	950 K/1000 K/1025 K/1050 K
t_{anneal}	20 min	20 min
$P_{H_2S,\ anneal}$	$1 \cdot 10^{-5}$ mbar	-

are visualized in figure 4.8 and a summary is given in table 4.3 for quick reference.

Various structures can be observed in dependence of growth temperature, as seen figure in 4.9. At lower temperatures (e.g. (950-1000) K) structures resembling the CLHs from chapter 4.1 can be found on the Au(111) surface (see figure 4.9 a)/b)). They consist of a darker core with a bright envelope. Similar to CLHs, no electronic signature is visible at the boundary of the two materials. Both the darker core and the brighter envelope exhibit a moiré pattern. While the material in the core resembles MoS_2, if with some bright inclusions, the envelope is only similar to TaS_2, showing a more diffuse surface, unlike that of pure TaS_2 islands or the TaS_2 in CLHs. This indicates a dilution with Mo or missing of S. It will be later identified as an alloy of the structure $Mo_{(1-x)}Ta_xS_2$ and is henceforth referenced as *alloy*.

The clearness of the structures varies from location to location, pointing to local changes in the relative amount of the available atomic building blocks of Mo, Ta, and S. The relative amount of alloyed structure increased from 950 K to 1000 K and the amount of MoS_2 decreased. More inclusions seem to be present

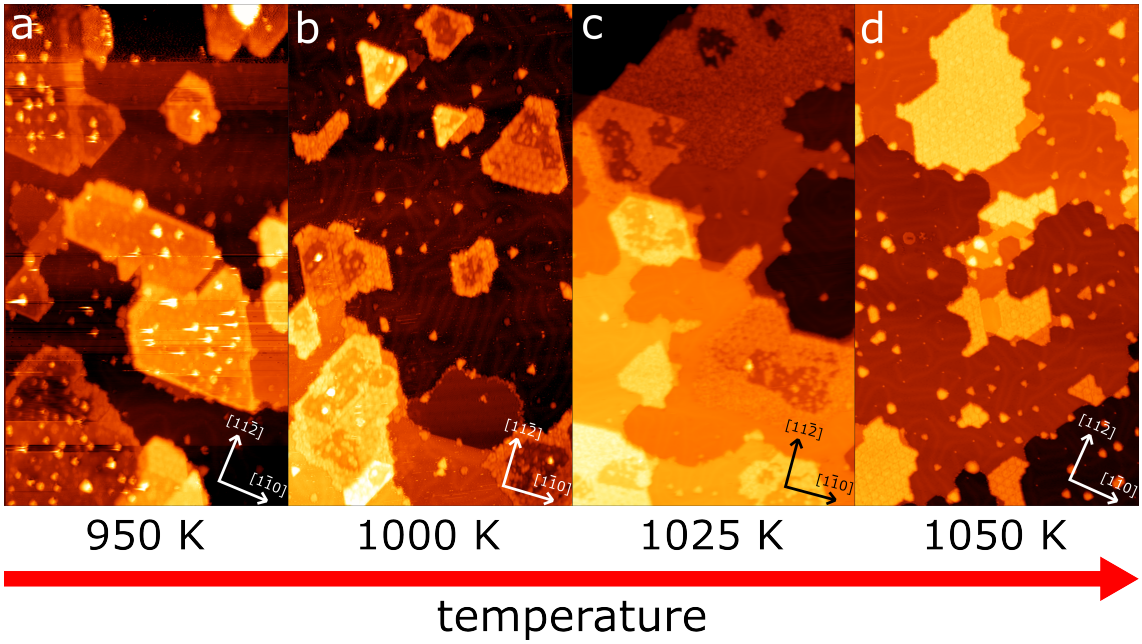


Figure 4.9: a) Preparation with second cycle annealing at 950 K; b) Preparation with second cycle annealing at 1000 K; c) Preparation with second cycle annealing at 1025 K; d) Preparation with second cycle annealing at 1050 K; All images: $U_{\text{bias}} = -0.5$ V, $I = 3 \times 10^{-10}$ A, individual dimensions: 85 nm × 150 nm.

in the MoS_2 at 1000 K than at 950 K. Both these images include second layer accumulations. At 950 K these accumulations are more prevalent than at 1000 K. These accumulations are discernible by their bright sphere like appearance. They occur mostly atop the MoS_2 and interfere with the measurement process of the STM, causing line like artifacts. The accumulations are likely caused by the Ta deposited in the second cycle.

At an annealing temperature of 1025 K (see figure 4.9 c)) the amount of alloyed structure in relation to the MoS_2 has increased further. Only little patches of MoS_2 are present. The borders between the MoS_2 and the surrounding alloy are uneven and many inclusions are present in the MoS_2. The area covered by the alloy has increased dramatically and areas with different surfaces, likely with different levels of Mo-Ta ratios are present.

Figure 4.9 d) shows results with an annealing step at 1050 K. Located on different steps of the Au(111) surface are islands of various sizes, consisting of only one uniform material. This material is similar to the alloys present in the earlier images. No MoS_2 can be found. Comparing the result to figure 4.7, this indicates that a uniform stable alloy has been achieved.

To further illustrate the grown structures, figure 4.10 a) shows a cutout from figure 4.9 b). Here three different types of structures are shown on three terraces of the Au(111) substrate. Figure 4.10 b) shows the same image with highlighting. In red, the darker MoS_2 core, usually with bright spots, and always surrounded by the brighter envelope is picked out. The MoS_2 has a vaguely truncated triangular shape and some moiré spots. The border between the MoS_2 and its envelope is uneven and bright inclusions are present in the MoS_2, as well as some second layer accumulations atop it. Usually the identification of the MoS_2 has rested on an analysis of its moiré pattern, as described in [26], but due to the bright inclusions in its structure, making regular observation of the moiré pattern difficult, the identification as MoS_2 is based on several other facts. The first indication is the growth process, which involves the creation of MoS_2 in its first cycle and the addition of Tantalum in the second cycle. In analogue to the previous MoS_2-TaS_2 CLHs, where the MoS_2 is contained in the center, here another type of CLH is formed of MoS_2 and an alloy envelope, with the MoS_2 in the same location. Additionally, the apparent height is comparable to the MoS_2 in MoS_2-TaS_2 CLHs. Therefore the identification as MoS_2 is deemed reasonable.

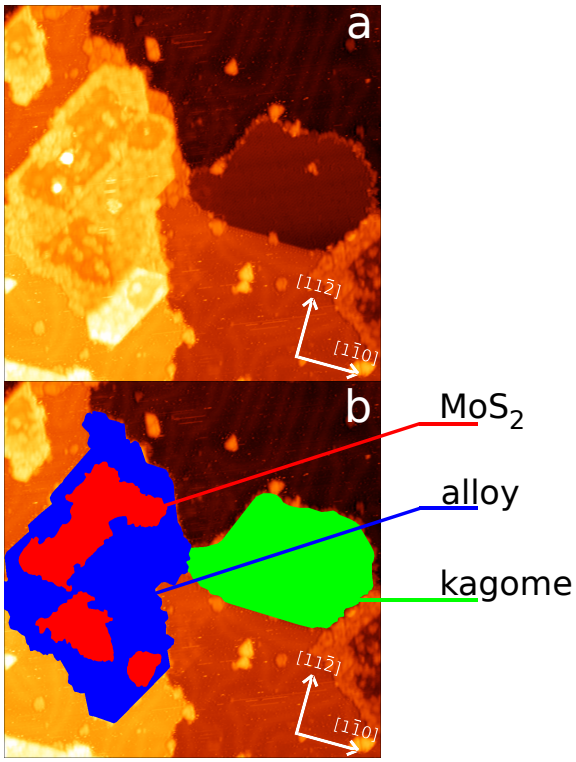


Figure 4.10: a) Mixture of observed materials including alloy, MoS_2, and kagome; b) Same image as *a)* but with areas of materials highlighted in different colors: red → MoS_2, blue → alloy, green → kagome; Both images: $U_{\text{bias}} = -0.5$ V, $I = 3 \times 10^{-10}$ A, dimensions: 70 nm × 70 nm.

Second, the bright envelope, identified as an $Mo_{(1-x)}Ta_xS_2$ alloy, is highlighted in blue. It surrounds the MoS_2 to form a CLHs or sometimes forms islands of its own. It has a hexagonal moiré pattern of a washed out nature whose clearness varies. Additionally, the bright inclusions in the MoS_2 are similar in nature to the bright envelope and therefore either made of TaS_2 or some alloy similar to $Mo_{(1-x)}Ta_xS_2$.

Lastly a structure is picked out in green. This structure is a kagome structure. It is described in further detail in chapter 4.4.

4.2.2 Structure of the $Mo_{(1-x)}Ta_xS_2$ Alloy

As preparations at various annealing temperatures lead to different amounts of mixture between the precursors, creating alloys with changing relative amounts of Mo and Ta, it is difficult to study them all, especially since the bright envelope containing the alloys is small at lower temperatures. The best candidates to take a closer look into are the preparations with higher annealing temperatures. The alloy has to present a hexagonal crystal structure, due to the presence of a hexagonal moiré pattern on its surface, while present on the hexagonal Au(111) surface. This pattern, however, can vary with location and annealing temperature, indicating strongly that various stages of mixture are present. A useful starting point for further analysis is therefore the alloy present in preparations which were annealed at 1050 K. Those yielded only one uniform type of structure, showing a very clear moiré pattern, with little to no variation with location.

Figure 4.11 a) shows the result from figure 4.9 d) in more detail. Three sets of brightness, due to three steps in the Au(111) surface, identifiable by the herringbone reconstruction, are visible. Located on these steps are small and large island structures. Small island structures tend to have a triangular shape. The larger structures indicate a tendency to form similar shapes but since they fill their terraces completely are restrained by those in their shape. A black box marks an area magnified in figure 4.11 b) to show the surface in more detail. While not as clear as for MoS_2, or TaS_2 islands, a moiré pattern can be observed. No individual atoms can be seen, however. Figure 4.11 c) shows a 2D autocorrelation of the close up shown in b). This presentation makes the repeating pattern more obvious and easier to evaluate. It can be clearly seen that the pattern is hexagonal, therefore confirming a hexagonal lattice structure. An analysis of the periodicity of this moiré results in

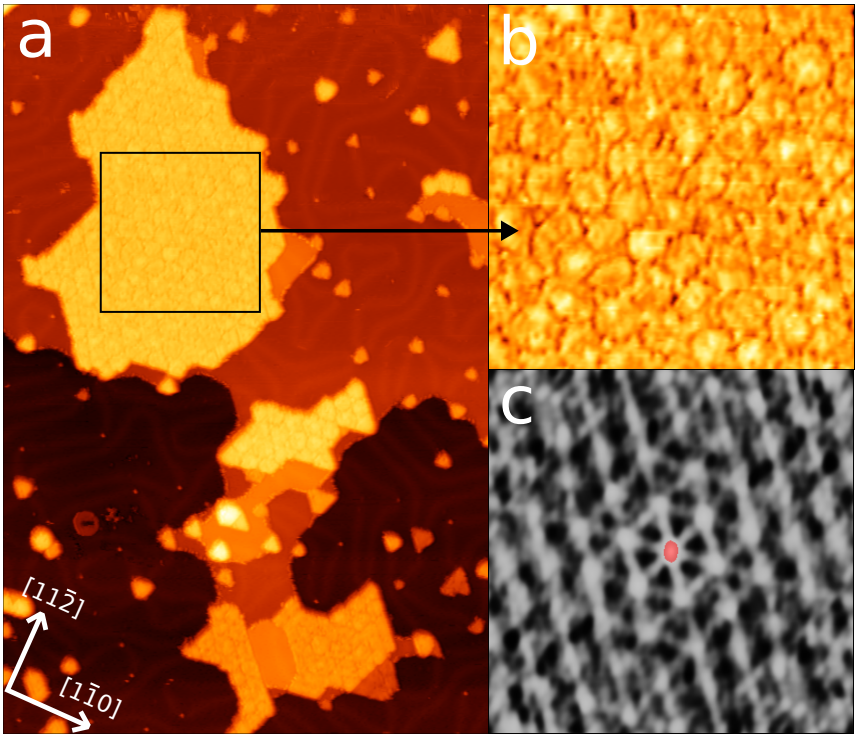


Figure 4.11: a) Islands of $Mo_{(1-x)}Ta_xS_2$ alloys on Au(111), the black box marks the area magnified in *b)*, $U_{\text{bias}} = -0.5$ V, $I = 3 \times 10^{-10}$ A, dimensions: 71.6 nm × 107.8 nm; b) Close up of area marked in *a)*, a moiré pattern can be observed on the surface, $U_{\text{bias}} = -0.5$ V, $I = 3 \times 10^{-10}$ A, dimensions: 23.4 nm × 23.4 nm; c) 2D autocorrelation of *b)*, the red dot highlights the location of highest correlation, representing little to no image shift, dimensions: 23.4 nm × 23.4 nm.

$a_{\text{moiré}}$ = (3.043 ± 0.15) nm. From this the lattice constant can be calculated with

$$a_{\text{moiré}} = \frac{a_{\text{gold}} \times a_{\text{lattice}}}{|a_{\text{lattice}} - a_{\text{gold}}|}, \tag{4.5}$$

resulting in

$$a_{\text{lattice, alloy}} = 0.3186 \pm 0.0011\ nm. \tag{4.6}$$

Comparing the result to the lattice constant of freestanding MoS_2 (a_{MoS_2} = (0.3157 ± 0.0003) nm [64]) and freestanding TaS_2 (a_{TaS_2} = (0.330 ± 0.001) nm [40]) the value marks an increase of 0.9 % compared to the MoS_2 and a decrease of 3.45 % compared to the TaS_2.

According to Vergard's law, the lattice constant of a solid solution of two materials is the weighted mean of the two constituent's lattice constants [115]. As a lattice constant between the one of freestanding MoS_2 and freestanding TaS_2 has been measured and together with the fact that Ta was added to existing MoS_2 is-

lands, such a solid solution will be assumed in the following, while keeping the simplicity of the assumption in mind. The resulting general structure can be determined following the formula $Mo_{1-x}Ta_xS_2$ and with the use of Vergard's law a value for x can be calculated, as well. Using

$$0.3186\,nm = (1-x)\cdot 0.3157\,nm + x\cdot 0.3300\,nm, \tag{4.7}$$

This results in a value x of ~ 0.2 and therefore a ratio of 0.8:0.2. Inserting this into our formula for the alloy results in $Mo_{0.8}Ta_{0.2}S_2$. This can be compared to the ratio of Mo and Ta received from the evaporation rates. With the evaporation rates of Mo at 0.01 ML/min for 25 min leading to 0.25 monolayers and Ta at 0.06 ML/min for 2 min leading to 0.12 monolayers, this results in an approximate ratio of 0.68:0.32. Due to the difficult nature of determining the evaporation rates accurately, it can be said that the two values are in good agreement and the assumption that the material generally follows Vergard's law is likely to be a good approximation for this structure. This type of analysis has also been done for other structures, prepared at the various different temperatures. All evaluations are done with topography or 2D autocorrelation images on a case by case basis. The results are presented in table 4.4.

Table 4.4: Values of moiré periodicity, calculated lattice constant and resulting alloy ratio by Vergard's law (rounded) for structures grown at various temperatures. Errors ranges consist of standard deviation and systematic measurement inaccuracy.

Annealing temperature [K]	Moiré periodicity [nm]	Lattice constant [nm]	Vergard ratio [Mo/Ta]
950 K	-	-	-
1000 K	2.63 ± 0.10	0.324 ± 0.001	42/58
1025 K/structure 1	3.36 ± 0.09	0.3155 ± 0.0006	100/0
1025 K/structure 2	2.73 ± 0.08	0.3224 ± 0.0007	53/47
1050 K	3.06 ± 0.09	0.3185 ± 0.0007	80/20

It was not possible to extract information from preparations annealed at 950 K, as the alloy envelope surrounding the MoS_2 was too thin to effectively evaluate its moiré. The other preparations indicate varying rates of mixture. While uncertainties for this type of measurement are high, a trend to increase the relative amount of MoS_2 in the mixture with an increase in annealing temperature is visible. The relative amount of Mo rises from 42 % up to 80 %. This behavior coincides with the hypothesis that the MoS_2 cores are slowly dissolving and merging with the

added Ta, creating a MoS_2-TaS_2 solid solution or alloy.

While Vergard's law is in good agreement with the structures gained from annealing at 1050 K, where a full mixture has been achieved, its limitations have to be discussed again.

For certain situations Vergards law might not be the most accurate way to describe an $Mo_{(1-x)}Ta_xS_2$ alloy, especially when the relative amounts of Mo in the mixture are low. Remmert et al. [116] investigated the change in lattice constant for bulk alloys of $Mo_{1-x}Ta_xS_2$. While not a perfect analogue, the in-plane lattice constant might give some indication for the behavior of monolayers. Figure 4.12 shows the results of powder diffraction measurements on these alloys with varying ratios of Mo and Ta (to avoid confusion, the reader is at this point reminded that [116] uses an inverse definition of the alloy).

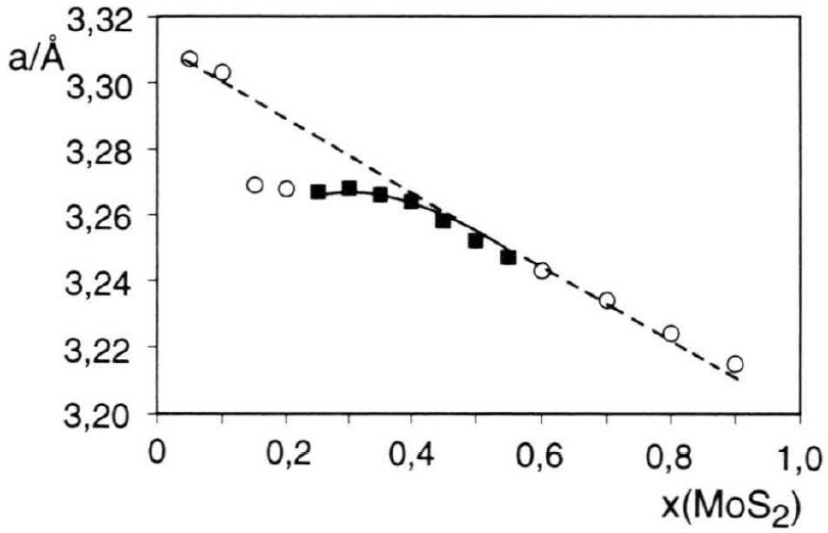


Figure 4.12: In-plane lattice constants of $Ta_{(1-x)}Mo_xS_2$ for various values of x, measured by powder diffraction. Squares show normal data, while circles show phases of which the exact composition could not be determined exactly by the scale. Reproduced under CC BY-NC-ND 3.0 [117] from [116].

It can be seen that the alloy only starts to follow the linear behavior known from Vergard's law after the relative proportion of Mo reaches about 40 %. Before this point, a constant value weighted towards the lattice constant of MoS_2 is measured. Therefore ratios calculated from lattice constants, via Vergards law, for the preparations annealed at 1000 K and 1025 K, might not result in an accurate answer. Instead a range of ratios might result in the same lattice constants. Still, a logical conclusion can be drawn from the data presented in table 4.4, when the in-

formation from figure 4.12 is taken into account. The composition of the mixture, as seen in figure 4.11, clearly changes with temperature, as in, the higher the temperature the sample is annealed at, the higher the relative amount of Mo which is present in the alloy. This is logical because at lower temperatures MoS_2 is still present on the sample but at 1050 K only an alloy structure is present. Therefore the MoS_2 must have completely merged with the added Ta, increasing the relative amount of Mo in the alloy.

An analysis of the relative amounts of coverage by the MoS_2 and the alloy supports this and will be presented in the following section.

Surface Coverage

As already visible in figure 4.11, the relative amount of surface covered by either the MoS_2, the alloy, or the kagome, changes from preparation to preparation. The preparation parameter varied was the temperature of the annealing step after the Ta was added. This varied from 950 K to 1050 K. Figure 4.13 a) shows the coverage in percentage of the whole surface covered, with alloys in blue, MoS_2 in red, kagome in green, and the sum of those three in yellow. Figure 4.13 b) shows the relative coverage in reference to the types of materials present, again with alloys in blue, MoS_2 in red, and kagome in green. Both graphs are in dependence of annealing temperature.

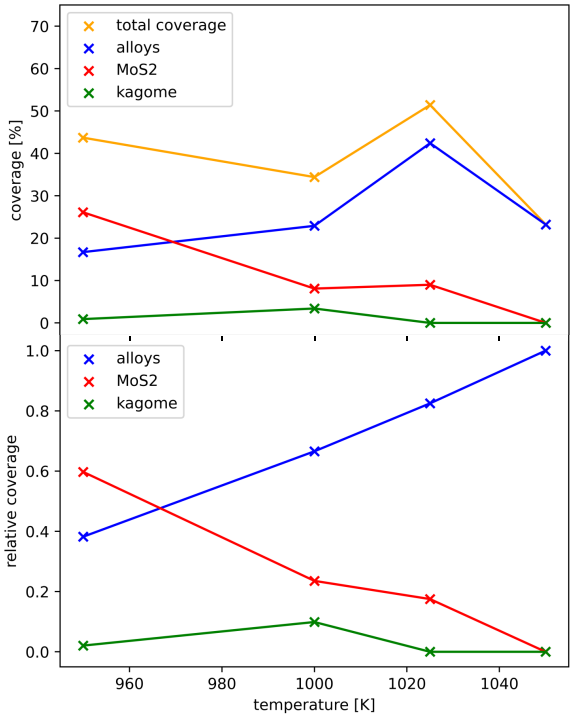


Figure 4.13: Absolute coverage of alloys, MoS_2, kagome and the whole surface (top) and relative coverage in reference to total coverage on the sample (bottom).

The coverage rates for the three materials vary greatly. While the kagome is relatively stable and covers between (0-3) % at any time, the amount of MoS_2 decreases steadily with an increase in temperature. At 950 K there is more MoS_2 on the sample than alloys but at 1000 K this fact has reversed already. Inversely, the amount of alloys increases with the temperature, starting with less

coverage than the MoS_2 and then steadily increasing, with a little drop at 1050 K. The overall coverage holds at around 45 % until 1050 K, where it drops to around 25 %.

As all structures on the surface are assumed to consist to at least some parts of S, the availability of it is of great importance. The only available source, however, are the MoS_2 islands present on the surface after the first growth cycle. Residuals of H_2S are possible to some degree but will be neglected in this analysis. As the area of surface covered by MoS_2, after the first cycle of preparation, results in a coverage of around 25 % and MoS_2 contains two S atoms for every unit cell, this represents the amount of available S atoms. MoS_2 has a hexagonal Bravais lattice and therefore its unit cell the area

$$A_{\mathrm{MoS_2}} = \frac{\sqrt{3}}{2} a^2_{\mathrm{MoS_2}} = 0.086\ nm^2. \tag{4.8}$$

This leads to a density of sulfur inside the area covered by MoS_2 of

$$d_{\mathrm{MoS_2,\ sulfur}} = \frac{1\ \mathrm{sulfur}}{0.043\ nm^2}. \tag{4.9}$$

All structures grown in the second cycle have to gain their S from the MoS_2 that used to be present on the surface after the first cycle. Since the amount of kagome on the surface is always negligible and the main focus is the alloy structure that grows around the MoS_2, it will not be taken into account.

Up until now the formula $Mo_{(1-x)}Ta_xS_2$ has been assumed even though another likely candidate would be $Mo_{1-x}Ta_xS$. Using the lattice constant a_{alloy} = (0.3185 $\pm$ 0.0007) nm, measured on the alloy at 1050 K, it is possible to calculate the necessary amount of precursor MoS_2 coverage to grow the material as either a disulfide or a monosulfide and show which is more reasonable.

Based on the fact that a hexagonal moiré pattern, on a hexagonal substrate, necessitates a hexagonal unit cell on part of the alloy, the area covered by a unit cell can be determined as

$$A_{\mathrm{unit\text{-}cell,\ alloy}} = \frac{\sqrt{3}}{2} a^2_{\mathrm{alloy}} = 0.088\ nm^2. \tag{4.10}$$

Resulting in a sulfur density of the disulfide of

$$d_{\mathrm{Mo_{1-x}Ta_xS_2,\ sulfur}} = \frac{1\ \mathrm{sulfur}}{0.044\ nm^2}, \tag{4.11}$$

while the monosulfide has a density of

$$d_{Mo_{1-x}Ta_xS,\ sulfur} = \frac{1\ \text{sulfur}}{0.088\ nm^2}. \tag{4.12}$$

From this follows that, if the alloy is a disulfide, for every nm^2 covered by an alloy 0.98 nm^2 of MoS_2 islands must have existed. If, however, the alloy is a monosulfide, for every nm^2 covered by an alloy only 0.49 nm^2 of MoS_2 must have existed to supply the sulfur. Since measurements of coverage and this analysis both have uncertainties, and this calculation is an estimation, the ratios are rounded. For the same reason the errors in the previous calculation are omitted. This results in a ratio of necessary precursor MoS_2 to alloy of 1:1 for a disulfide alloy and 1:2 for a monosulfide alloy. Comparing this to the result of total coverage for the alloy gained by annealing at 1050 K (shown in figure 4.13 top) good agreement is found with the 1:1 ratio. It is therefore reasonable to assume that the alloy formed at 1050 K is a disulfide with the formula $Mo_{1-x}Ta_xS_2$.

Moreover, the coverage of MoS_2 after the first cycle establishes the upper limit of coverage possible for the alloy. From that point, the total surface coverage of the two materials must effectively stay the same if $Mo_{1-x}Ta_xS_2$ is present. This general trend is confirmed by the results in figure 4.13, as well. Additionally, the coverage of alloys must be roughly the inverse of the remaining MoS_2, which can also be seen in figure 4.13 bottom. If the alloy would be a monosulfide, the total coverage on the sample would rise and for every unit of MoS_2 lost, two units of alloy would be gained. This would lead to an upper limit of about double the surface coverage established by the MoS_2 islands. This is not the case. Therefore, while local exceptions might apply, it can tentatively be assumed that the alloy formed at other temperatures is also $Mo_{(1-x)}Ta_xS_2$.

All of these results coincide well with the first principles calculations by Hemmat et.al [19], who predicted the existence of stable $Mo_{1-x}Ta_xS_2$ alloys above 1000 K. Below This temperature, depending on the concentrations of the two TMDCs, metastable and unstable phases can exist. This is also well in accordance with the observation, as temperatures from 950 K to 1050 K were utilized in the growth process. Up to 1025 K stable MoS_2 is still observed, while also (possibly unstable) alloys of various rates of mixture accumulate around the MoS_2. Yet, a clear separation of the two materials is present. If the temperature is raised sufficiently, only one stable alloy phase is observed.

4.2.3 Alternative Growth Process

The formation process of alloys can be further appended upon by an additional, small, change to the preparation cycles. This section will summarize these new preparation parameters first and present some of the results afterwards.

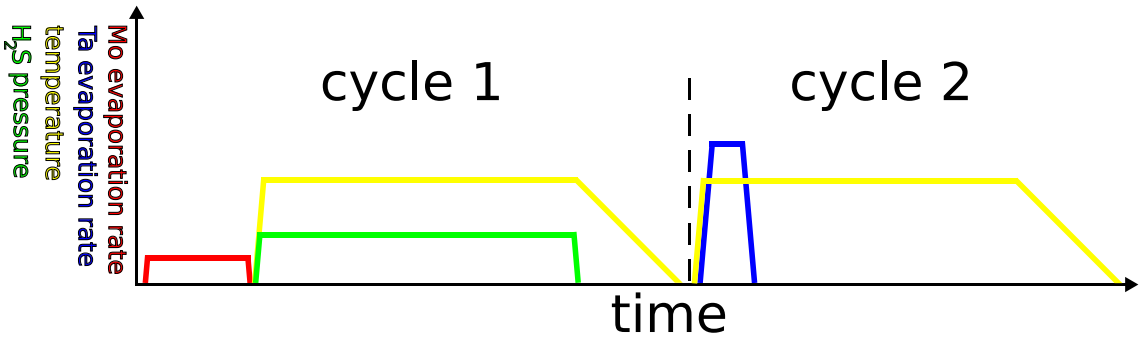


Figure 4.14: Schematic of active parameters for alternative alloy growth process over time: Evaporation of Mo (red); evaporation of Ta (blue); presence of H_2S (green), high temperatures (yellow).

Table 4.5: Parameters for the preparation of the alternative growth process.

	Mo	Ta
T_{evap}	300 K	900 K
t_{evap}	5 min	1 min 30 s
R_{evap}	0.01 ML/min	0.06 ML/min
T_{anneal}	900 K	-
t_{anneal}	20 min	-
$P_{H_2S,\ anneal}$	1×10^{-5} mbar	-

The first cycle of the preparation was kept as normal. Mo was evaporated at RT for 25 min with a rate of 0.01 ML/min for 5 min. This was followed by annealing in an H_2S atmosphere of $1{\times}10^{-6}$ mbar for 20 min. Afterwards the sample was cooled down and as a temperature of 450 K was reached the H_2S supply was shut off. This first cycle creates the well established MoS_2 islands on the surface. In the second cycle, the sample was heated to 900 K and as soon as the temperature was reached Ta was evaporated with a rate of 0.06 ML/min for 1 min 30 s. This was followed by an immediate cooldown to RT. A visual representation of the active parameters over time can be found in figure 4.14 and a summary of the growth parameters is shown in table 4.5 for quick reference.

An overview of the resulting structures is presented in figure 4.15. Figure 4.15 a) shows islands on the Au(111) surface, which is recognizable by the characteristic herringbone reconstruction in the background. A step is present due to the drastic change in brightness in the top right corner of the image. Atop this background are island structures. The structures present dark cores, similar to CLHs but with a high amount of bright inclusions. These cores are surrounded by bright envelopes exhibiting various phases. A moiré pattern is discernible on these envelopes only. Depending on the phase, the moiré is clear and resembles that of TaS_2 or is less sharp and includes additional spots located in some of the minima of the hexagonal superstructure. One of the islands grows over the step of the Au(111), which is a rarity for TMDCs.

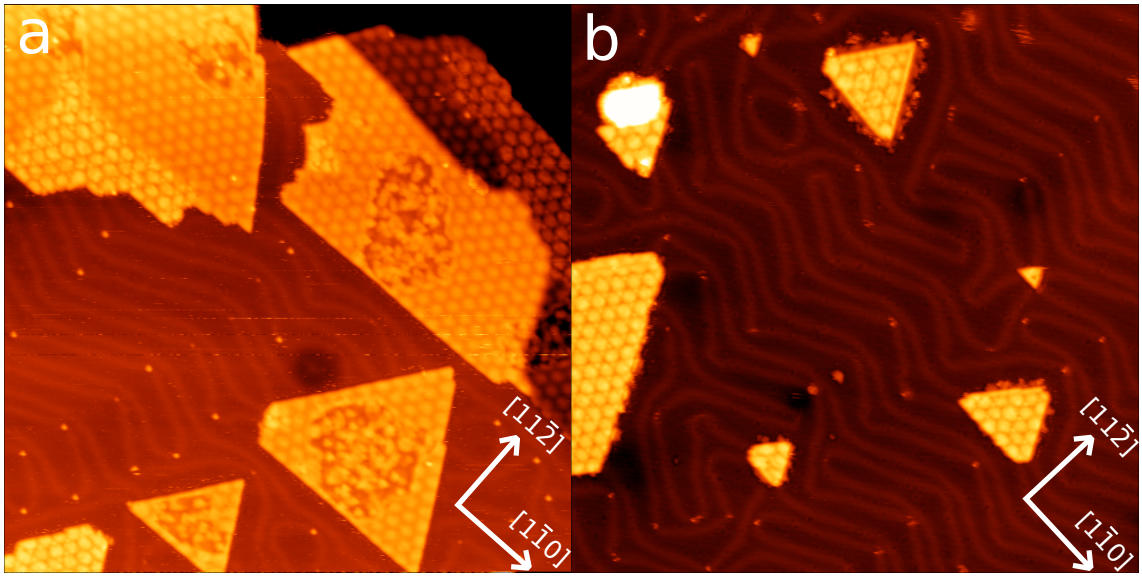


Figure 4.15: a) Islands with different phases of TMDCs. A dark core with obvious signs of mixing and brighter phases of TMDCs surrounding the cores similar to CLHs. $U_{\text{bias}} = -0.5$ V, $I = 3 \times 10^{-10}$ A, dimensions: 79 nm × 79 nm; b) Islands of a thoroughly mixed TMDC. $U_{\text{bias}} = -0.5$ V, $I = 3 \times 10^{-10}$ A, dimensions: 81 nm × 81 nm.

Figure 4.15 b) shows a group of smaller islands. The islands exhibit a generally triangular shape and are located on a single plateau of the Au(111) surface. Again, the characteristic herringbone reconstruction is visible in the background. A uniform phase is present on these islands. This phase also exhibits a moiré with additional spots in some of the minima of the hexagonal superstructure. It is noteworthy that one of the islands exhibits a special formation at its edges. This formation encloses the island completely like a border line. Another island presents this structure on one of its edges.

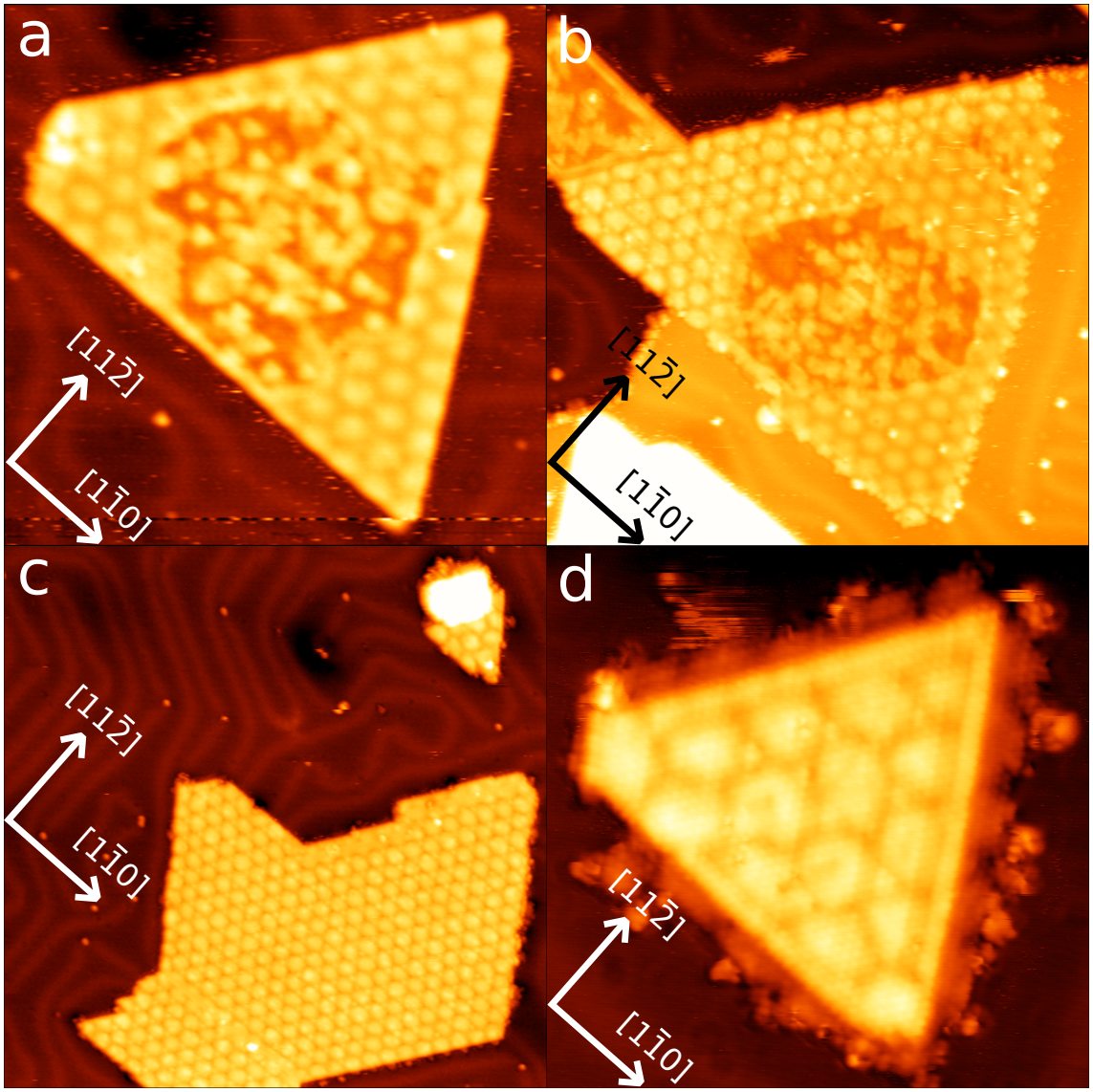


Figure 4.16: Different types structures present on the substrate after preparation with parameters in table 4.5: a) Island similar to CLH with signs of mixing in the core and an outer rim resembling TaS_2, dimensions: 30.5 nm × 30.5 nm; b) Island similar to the one in *a)* but the envelope exhibits multiple, differing, phases, one of which resembles TaS_2, dimensions: 45 nm × 45 nm; c) Islands resembling TaS, dimensions = 66 nm x 66 nm, d) Island with moiré similar to TaS and complexly-structured edges, dimensions = 16.6 nm × 16.6 nm; All images: $U_{\text{bias}} = -0.5$ V, $I = 3 \times 10^{-10}$ A.

Four of the structures are picked out, representing most of the observed phenomena. These are shown side by side in figure 4.16 and will be described in more detail.

The first one, pictured in figure 4.16 a), is structure of triangular shape similar to the CLHs. An inner core, with inclusions, and a bright envelope are present. The shape of the core is roughly hexagonal but, due to the high amount of bright inclusions, it is not very distinct. The envelope on the other hand, is of one clear phase and shapes the structure into a triangular shape. It exhibits a moiré and is structurally similar to TaS_2. The edge is straight and clear.

The second structure, pictured in figure 4.16 b), is similar to the structure shown in figure 4.16 a). A darker core with bright inclusions is present, surrounded by a brighter envelope. Here, however, multiple phases are present in the envelope. Some are similar in structure to TaS_2, like in the earlier envelope, while others present a moiré with additional spots in some of the minima of the pattern. The overall shape of the island is triangular the edges are jagged.

Figure 4.16 c) mainly shows one big island. The island is made of a uniform material exhibiting a moiré pattern with additional spots in its minima. A grain boundary is present on the bottom left of the island. The island has a mixture of straight edges and edges that follow the outline of the moiré pattern.

In figure 4.16 d) a triangular island is shown in atomic resolution. It also exhibits a moiré pattern with additional spots. The island has the special edge structure mentioned earlier, wherein a two to three atom wide straight line, exhibiting no continuation of the moiré pattern, surrounds the whole island.

4.2.4 Structural Analysis

To gain more information about these structures, the lattices were analyzed in further detail. As the structures were unknown, a special regimen was followed to retain a normalization for calibration of the images.

To start, the island with atomic resolution in figure 4.16 d) was used to calculate the lattice constant via moiré analysis (see [113]). From this the moiré periodicity was calculated and a normalization could be created. This normalization has been applied to the other structures and subsequently their moiré periodicity has been measured, as well as their lattice constants calculated. The results are summarized in table 4.6.

Table 4.6: Moiré periodicity and lattice constants for the patterns shown in figure 4.17.

	Moiré periodicity [nm]	Lattice constant [nm]
Figure 4.17 a)	2.25 ± 0.02	0.3307 ± 0.0009
Figure 4.17 b)	2.227 ± 0.004	0.3313 ± 0.00019
Figure 4.17 c)	2.221 ± 0.003	0.3314 ± 0.00014
Figure 4.17 d)	2.52 ± 0.14	0.3256 ± 0.0024

Figure 4.17 shows the moiré patterns from the corresponding structures in figure 4.16 in more detail. The pattern in figure 4.17 a) resembles the pattern of TaS_2 on Au(111) very closely. A hexagonal pattern is present with no additional spots. Together with a measured periodicity of $a_{\text{periodicity}}$ = (0.3307 ± 0.0009) nm the lattice is very much aligned with previous measurements by Silva et al, which resulted in a_{TaS_2} = (0.330 ± 0.001) nm [40]. It is therefore reasonable to assume that TaS_2 was formed with sulfur taken from the MoS_2 islands which were present after the first growth cycle.

Figure 4.17 b) also shows a hexagonal moiré pattern. This one, however, includes additional spots in some of its minima. A lattice constant of a_{lattice} = (0.3313 ± 0.00019) nm has been determined, which is slightly higher than freestanding TaS_2. Comparing these results to the lattice constant of TaS (β-phase), a^{β}_{TaS} = (0.332 ± 0.001) nm, good agreement can be found not only between the lattice constants but also due the characteristic, additional, spots exhibited by the moiré pattern (see [97]). This indicates that due to a lack of sulfur supply, a monosulfide has been formed by the applied Ta. Close inspection of the structure in figure 4.16 b), shows that two phases are exhibited on the island's envelope. One without the

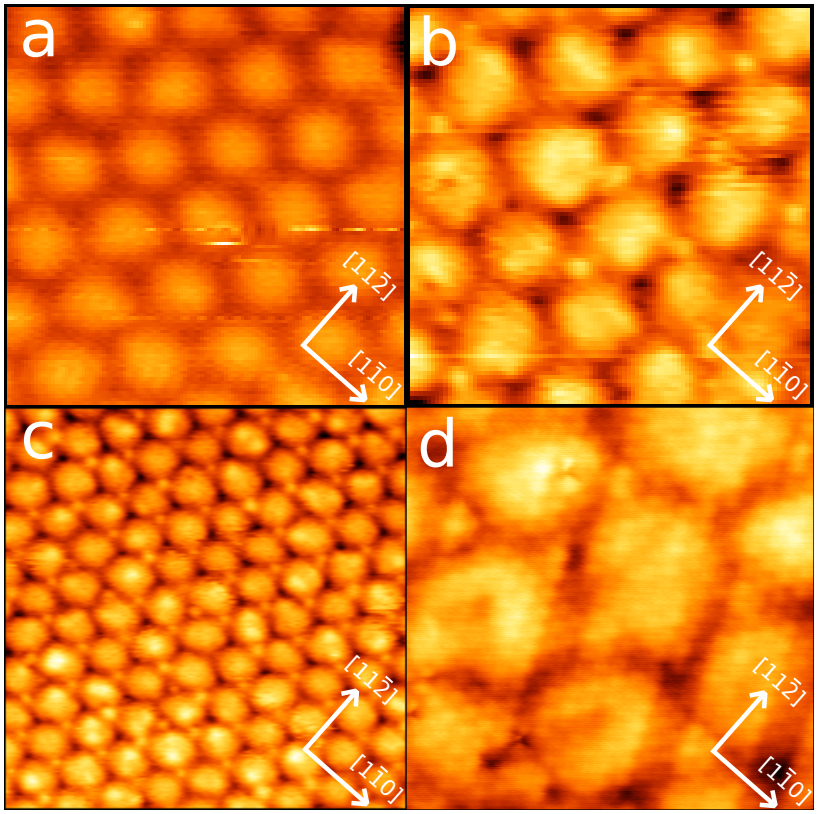


Figure 4.17: Moiré patterns from 4.16 a)-d) respectively: a) Dimensions: 11.8 nm × 11.8 nm; b) Dimensions: 9.7 nm × 9.6 nm; c) Dimensions: 22.5 nm × 22.5 nm; d) Dimensions: 7.2 nm × 7.2 nm; All images: $U_{\text{bias}} = -0.5$ V, $I = 3 \times 10^{-10}$ A.

additional spots and one with the additional spots. It is therefore assumed that the local sulfur supply varied, forming areas of TaS and areas of TaS_2.

The structure from figure 4.17 c) exhibits a lattice constant of a_{lattice} = (0.3314 ± 0.00014) nm, together with additional spots in its minima. This is, again, characteristic of TaS, which was likely formed due to low supply of sulfur during the growth process.

Figure 4.17 d) shows a more complex picture than the structures before. A moiré is present and shows additional spots in most of its minima. A lattice constant of a_{lattice} = (0.3256 ± 0.0024) nm has been determined. This result is below both the lattice constant of TaS_2 and TaS. Moreover, the three-atom wide edge structure surrounding the island has been observed in neither TaS_2 nor TaS. The reduction in lattice constant could be due to alloying with MoS_2. Assuming Vergard's law, which has come with its own restrictions before, the addition of the Mo could reduce the lattice constant of the mixture. In this case an alloy of roughly $Mo_{0.31}Ta_{0.61}S$ might be present.

Both the growth of TaS and $Mo_{(1-x)}Ta_xS$ are a likely candidates for some of the

structures resulting from this growth process. It has been established that TaS grows in low sulfur environments [97], which indeed was present here. All sulfur must be supplied from the MoS_2 islands present after the first cycle of the preparation. Some of these MoS_2 islands are still visible inside the new structures, yet they appear to be diminished in size and form and present many inclusions. This could indicate the tendency of the Ta to replace Mo in those islands. The high temperatures might also help the release of bound S, which then can be repurposed by the Ta.

Additional Annealing

An additional experiment tested the behavior resulting from the application of an additional annealing step. The sample was annealed for 10 min at 900 K, after the above listed preparation procedure had been completed. This resulted in new structures which can be seen in 4.18.

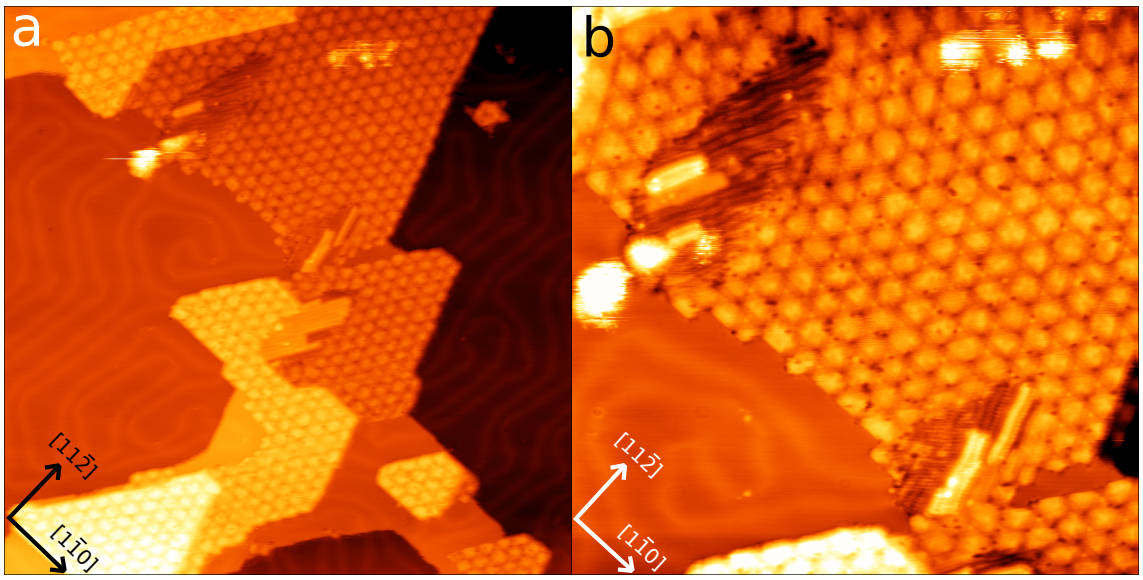


Figure 4.18: a) Result after additional annealing at 900 K for 10 min, dimensions: 88 nm × 88 nm; b) Close up of *a)*, dimensions: 45 nm × 45 nm; Both images: $U_{bias} = -0.5$ V, $I = 3 \times 10^{-10}$ A.

Figure 4.18 a) shows an overview of the resulting structures. Several islands can be seen located on various steps of the Au(111) surface. These steps are identifiable by the herringbone reconstructions in the background and are distinguishable by the various degrees of brightness. Two phases of material are present. A bright island structure exhibiting a moiré pattern with additional spots, in analogue to figure 4.16 c), and a new structure. This new structure is

darker and oval in shape. Close inspection shows that the structure consists of atoms stacked in threads of parallel lines. This material is only observed in conjunction with the earlier mentioned island structure.

Cursory analysis shows a lattice constant, in the direction of the lines of this new core, of a_{inline} = (0.379 ± 0.03) nm and from line to line of $a_{\text{line-line}}$ = 0.3416 ± 0.06) nm, measured for the structure at the top in figure 4.18 b). The structure at the bottom figure 4.18 b) exhibits a lattice constant of a_{inline} = (0.328 ± 0.03) nm and $a_{\text{line-line}}$ = (0.299 ± 0.06) nm. In both cases the errors are based on measurement inaccuracy and estimations of normalization offsets, as no known structures as reliable reference are present in the images.

Comparing the structures, one can see quickly that there is a huge deviation between lattice constants at the two spots, even though visual inspection shows great similarity between the two materials. Several factors can be at play here. The first is the direction the lines in the two structures point towards, as they are not parallel to each other. This might lead to a structural difference, possibly due to the connection to the island that surrounds them. Another point might be the missing normalization, as the image could be distorted differently in the two directions. Overall the results of the additional annealing step supports the idea that S is taken from the MoS_2 to grow new island structures with Ta. The supposed MoS_2 cores from before have likely diminished further and changed into the striped material. Most of the S has been incorporated into the surrounding envelope which is likely another monosulfide, due to the presence of additional spots in the moiré, and possibly alloyed with Mo to varying degrees.

While the true dimensions and structural compositions of these new cores cannot be determined from present data, speculation about their nature is still possible. Assuming S has been removed from MoS_2, a simple assumption is that an undersulfurized deviation of MoS_2 is present. Studies by Wang et al. and Chen et al., on vacancies in MoS_2, have shown that the lattice of MoS_2 can reconstruct and form extended line vacancies upon removal of consecutive S atoms, changing the stoichiometry from MoS_2 to Mo_3S_5 [118, 119]. The results appear very similar to the observations in figure 4.18. Analyses of a TEM image, in figure 9 b) of the supplementary material of the study by Wang et al.[118], yield lattice constants of a_{inline} = (0.3308 ± 0.002) nm and $a_{\text{line-line}}$ = (0.2236 ± 0.002) nm, with the error as the estimation of measurement offsets. The distance of S to S was measured, as it was assumed that the STM in the experiment of this dissertation would still pick

out S atoms over Mo, even in highly undersulfurized conditions.

The lattice constant a_{inline} of the structure from Wang et al. is quite comparable to the value measured for the structure at the bottom of figure 4.16 b), yet, deviates a little for the structure at the top. The line to line lattice constant $a_{\text{line-line}}$, even with the great measurement uncertainties is further away from that reference structure. Overall, many similarities exist between the observation by Wang et al., Chen et al., and this experiment. Therefore, the current prediction is that a similar structure has been observed as the result of this additional annealing step. Deviations in the measured lattice constant might be explained due different environments and missing normalizations. The MoS_2 presented by Wang et al. was grown on an SiO_2/Si substrate and measured on an Si_3N_4 TEM grid. This minimizes substrate interactions, which can be present with an Au(111) substrate. Yet, a more dominant factor might be that the material was freestanding, while the experiment in this thesis is in combination with a secondary material, forming a type of CLH. As seen in chapter 4.1, the connection to a second material with a different lattice constant can lead to mechanical distortions as a result of stresses. Close inspection of figure 4.18 b) shows that the lines are not straight but in fact wavy. This might be due to the close connection with the surrounding island structure, causing great stress and deforming these lines, leading to a change in lattice constant. Ultimately, further analysis is needed to make a conclusive judgment.

4.2.5 Conclusion

It has been shown that MoS_2 islands can be turned into $Mo_{(1-x)}Ta_xS_2$ alloys by application of Ta at RT and subsequent annealing in an H_2S-free environment. This shows that if not enough H_2S is present to form the newly arriving Ta into TaS_2, it will start diffusion processes with the MoS_2, integrating in it and possibly acquiring its S to realize the structures of its own.

Moreover, relative amount of resulting alloys could be shown to be in dependence of the annealing temperature and the structural formula was determined by Vergard's law and the relative surface coverages of present materials. In addition to this, the relative amounts of Mo in the alloy have been estimated at various annealing temperatures, showing an analogue dependence on these temperatures, wherein the amount increases with their increase. This shows that the predictions of [19] are accurate and can be realized under real world conditions, indicating other alloys could be grown as well. The ability to finely tune the amount of alloys present and their rates of mixture, just from the annealing temperature, also opens many reliable avenues for further growth processes. This makes it possible to engineer coverage or mixture rates that could be used in the growth of CLHs with alloys or stacked heterostructures. The fact that these alloys form in the first place shows that complicated diffusion processes can take place, even after islands of the first growth cycle are seemingly fully formed and emphasizes the importance of material availabilities during growth.

In addition to this, an alternative growth process has been presented, wherein Ta is evaporated onto the MoS_2 islands at elevated temperatures. This leads to the formation of various structures including alloys and CLH. These CLHs have MoS_2 cores with high levels of inclusions and envelopes of many different phases. Due to the short nature of the high temperature step, this likely presents another middle point between stable CLHs and alloys. These varied aspects suggest that the applied Ta and pre-existing MoS_2 islands form a complex diffusion process, with varying amounts of Ta, Mo, and S involved, resulting in the plethora of different structures seen. The fact that the MoS_2 islands where already at high temperatures seemed to play a role in these processes, possibly allowing the Ta additional paths of diffusion, like the z-direction, on arrival.

This has been expanded upon by an additional annealing step, leading to more diminishment of the MoS_2 cores, likely forming them into an undersulfurized form of their former selves, possibly Mo_3S_5, underlining the trend to fully desolve the MoS_2 islands and form an $Mo_{(1-x)}Ta_xS_2$ alloy.

All of this shows the intricate, diffusion based, interactions taking place between the involved materials. These, however, are not only able to form new structures but under the right conditions, effects like the Kirkendall holes can be observed, too.

4.3 Kirkendall Holes in Two-Dimensional $Mo_{(1-x)}Ta_xS_2$ Alloys

The results presented in this chapter are based on the work published in The Journal of Physical Chemistry Letters [120]. Due to the results of chapter 4.2 the alloys in this chapter will be referenced as $Mo_{(1-x)}Ta_xS_2$ instead of $Mo_xTa_yS_2$, as in the referenced publication.

By varying the growth parameters of the cyclic growth process, not only different points of the MoS_2-TaS_2 structural phase diagram can be investigated, showing a multitude of structures, but also fascinating physical effects can occur. By introducing a minute change to the growth process of CLHs presented in chapter 4.1, the formation of Kirkendall holes, as a 2D-equivalent to Kirkendall voids, in $Mo_{(1-x)}Ta_xS_2$ alloys can be observed.

4.3.1 Preparation and Resulting Structures

Again, for ease of reference and reproduction of the experiments, the preparation parameters will be summarized shortly, before the resulting structures are shown.

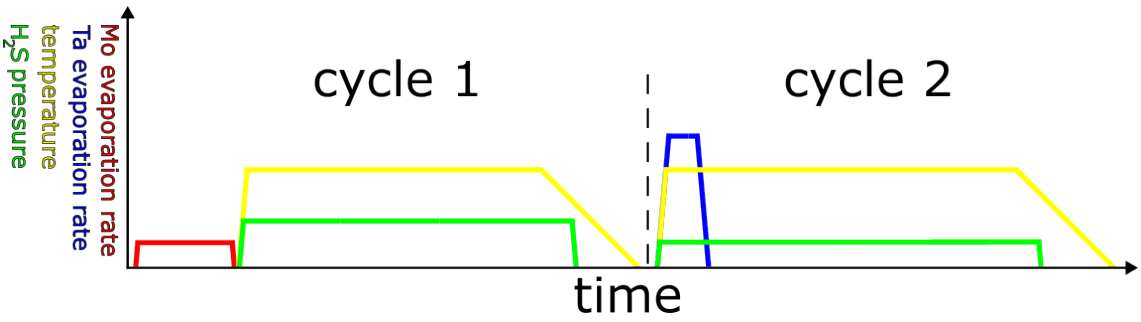


Figure 4.19: Schematic of active parameters for preparation with Kirkendall holes, over time: Evaporation of Mo (red); evaporation of Ta (blue); presence of H_2S (green), high temperatures (yellow).

To create islands presenting these holes, the first cycle of the cyclical growth process, as presented in chapter 3.2, was applied. Mo was evaporated with 0.01 ML/min for 5 min, with the sample at room temperature. This was followed by annealing in H_2S at a chamber pressure of 1×10^{-5} mbar and a temperature of 900 K for 20 min. Afterwards the sample was cooled down to RT. As soon as a temperature of 450 K was reached during the cooldown, the H_2S supply was shut off. In the second cycle, the growth process was modified by evaporation of Ta

at a temperature of 900 K, in an H_2S atmosphere of 1×10^{-6} mbar. This was followed by continuous annealing at 900 K in said atmosphere, for 20 min, without further Ta evaporation. After these 20 min, the sample was cooled down and at 450 K the supply of H_2S was shut off. Figure 4.19 shows an illustration of the active parameters over time and table 4.7 summarizes these parameters for quick reference.

Table 4.7: Parameters for preparations which will result in the Kirkendall effect.

	Mo	Ta
T_{evap}	300 K	900 K
t_{evap}	5 min	1 min/1 min 30 s
R_{evap}	0.01 ML/min	0.06 ML/min
P_{evap}	-	1×10^{-6} mbar
T_{anneal}	900 K	-
t_{anneal}	20 min	20 min
$P_{H_2S,\ anneal}$	$1 \cdot 10^{-5}$ mbar	-

Results of this growth process can be seen in figure 4.20. In figure 4.20 d), islands later identified as a $Mo_{(1-x)}Ta_xS_2$ alloy, similar to the one in chapter 4.2, with an approximately triangular shape are located on several steps of the Au(111) surface, identifiable by the different degrees of brightness of the background. The islands stretch over several of these steps, an occurrence which is uncommon in freestanding TMDC monolayers or CLHs. Located roughly in the center of these islands are holes, which will be shown to be caused by the Kirkendall effect. These holes are the two-dimensional version of the well established Kirkendall voids and shall henceforth be referenced as *Kirkendall holes*.

Through these holes the Au(111) surface with its herringbone reconstruction is visible. This is highlighted in the close up shown in figure 4.20 e). The holes exhibit a truncated triangular or sometimes almost hexagonal shape, similar to MoS_2 islands or MoS_2 cores in CLHs.

To lend as a tool of comparison and to illustrate how a minute change in the preparation parameters causes a significant deviation in resulting structures, figure 4.20 a) shows MoS_2 as it would be grown by the first cycle of the preparation process and figure 4.20 b) and c), shows CLHs as they would appear if the Ta in the second preparation cycle would have been evaporated at RT, instead of at 900 K.

A blue arrow indicates the preparation path from MoS_2 to CLHs, by evaporating the Ta at low temperatures, while a yellow arrow indicates the path to alloys with Kirkendall holes, by evaporation of Ta at high temperatures. Comparing the

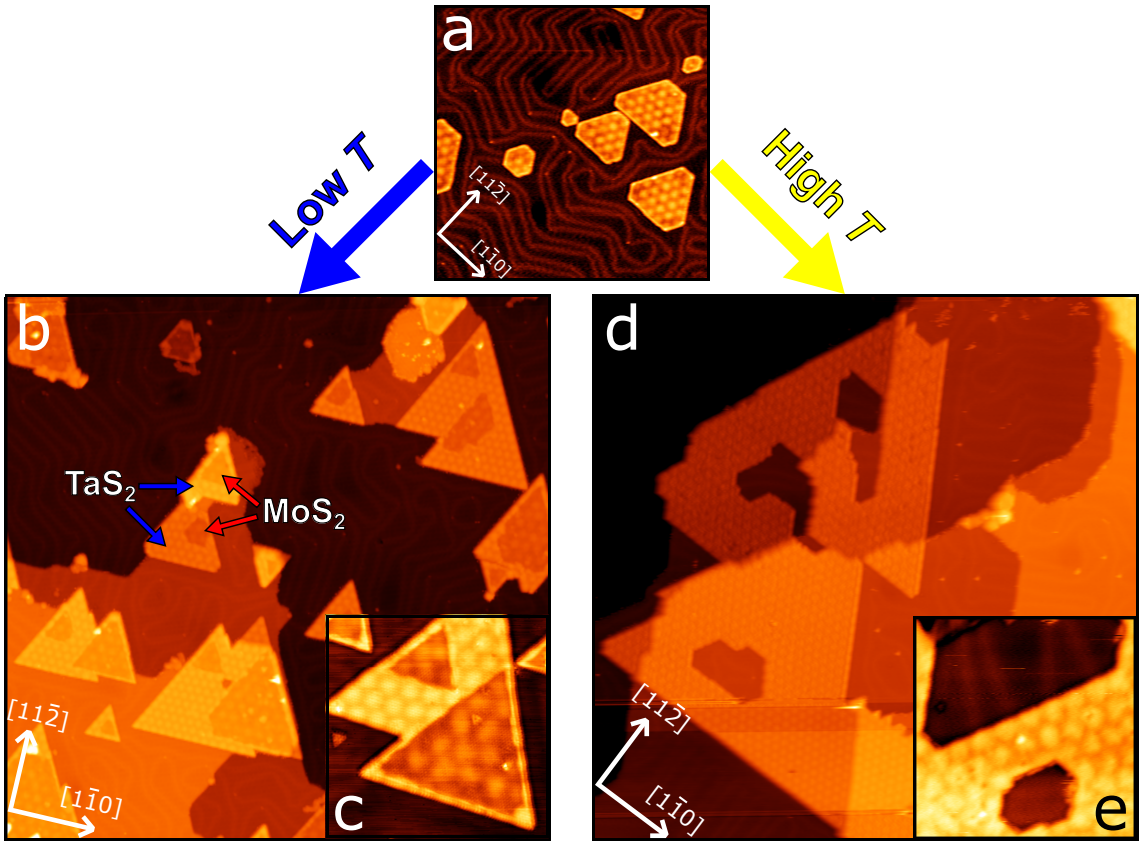


Figure 4.20: Formation of $Mo_{(1-x)}Ta_xS_2$ islands with Kirkendall holes on Au(111) (STM, same scale): a) Initial MoS_2 islands after the first preparation cycle, dimensions: 75 nm × 75 nm; b) Low-temperature process leads to lateral MoS_2-TaS_2 heterostructures, dimensions: 150 nm × 150 nm; c) close up, dimensions: 24.4 nm × 24.4 nm. d) High-temperature process leads to $Mo_{(1-x)}Ta_xS_2$ islands with Kirkendall holes, dimensions: 150 nm × 150 nm; e) close up with herringbone reconstruction of Au(111) visible through the holes, dimensions: 25 nm × 25 nm. Image d): $U_{bias} = -0.25$ V, $I = 3 \times 10^{-9}$ A; All other STM images: $U_{bias} = -0.5$ V, $I = 3 \times 10^{-10}$ A. Reused with permission from [120].

Kirkendall holes in figure 4.20 d) to the MoS_2 islands in a) and the CLHs in figure 4.20 b) and c) underlines the earlier statement about the similarity of the holes' shape to that of freestanding MoS_2 or MoS_2 cores in CLHs. Especially some of the distorted and elongated MoS_2 cores of the CLHs exhibit a very similar shape to the Kirkendall holes. Together with their positions, this indicates that they have replaced the MoS_2 by vacancy diffusion.

4.3.2 Moiré Analysis

Kirkendall holes are an effect of the vacancy diffusion process between two adjoined materials. When the diffusion coefficients between two materials varies significantly, vacancies moving into the material with the lower mobility can be trapped there and accumulate in the border region. Information about the diffusion process creating the Kirkendall holes can be obtained from a moiré analysis. In figure 4.21 a) one of these Kirkendall holes is seen surrounded by an island

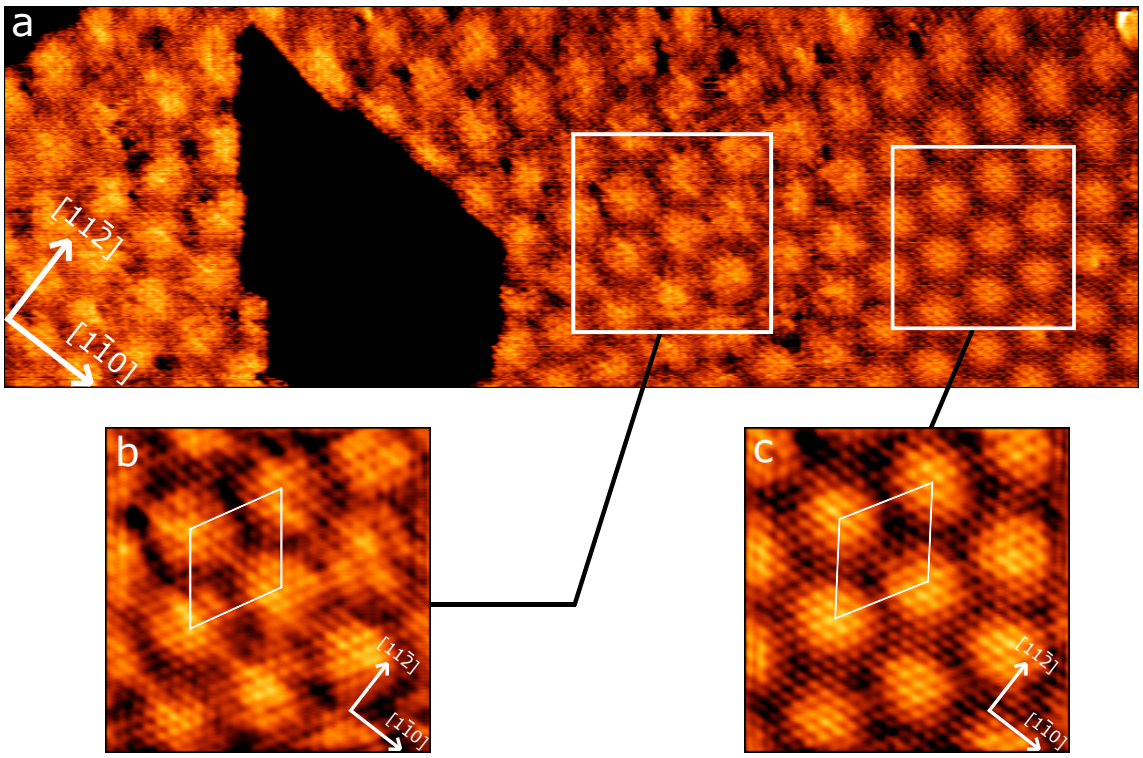


Figure 4.21: a) $Mo_{(1-x)}Ta_xS_2$ island with Kirkendall hole and surrounding material showing varying states of mixing, $U_{bias} = -0.25$ V, $I = 1 \times 10^{-9}$ A, dimensions: 52 nm × 17 nm; b/c) Fourier-filtered close ups as indicated by the white boxes in a) with sizes: 9 nm × 9 nm and 8 nm × 8 nm. A white rhombus marks a unit cell of the moiré in each of them. Reused with permission from [120].

structure in atomic resolution. The clarity of the moiré varies drastically so that two areas with different phases can be identified. Closer to the hole more defects are present and the moiré is less sharp, while further away less defects are present and the moiré more closely resembles that of TaS_2. In each of these phases an area is marked by a white square. Figures 4.21 b) and c) show Fourier-filtered versions of the areas highlighted in figure 4.21 a). In both of these a white rhombus marks a unit cell of the moiré. Using a moiré analysis the lattice constant in the two areas can be determined with

$$\frac{1}{n \cdot a_{\mathrm{TMDC}}} = \frac{1}{a_{\mathrm{Au(111)}}} - \frac{1}{a_{\mathrm{TMDC}}}. \tag{4.13}$$

Here n represents the number of atoms between two moiré maxima. Twelve unit cell are evaluated in each area. The area close to the Kirkendall hole exhibits an average number of (7.4 $\pm$ 0.5) atoms per unit cell, resulting in a lattice constant a_{close} = (0.327 $\pm$ 0.003) nm. The area further apart from the hole counts (6.8 $\pm$ 0.5) atoms on average, leading to a lattice constant of a_{distant} = (0.331 $\pm$ 0.003) nm. The uncertainties result from the standard deviations and systematic measurement errors. Comparing these results to the lattice constants of MoS_2 on Au(111) with a_{MoS_2} = (0.3157 $\pm$ 0.0003) nm [64] and TaS_2 on Au(111) with a_{TaS_2} = (0.330 $\pm$ 0.001) nm [40], it is reasonable to assume that the area further away, which already resembles TaS_2, consists in fact mostly of TaS_2. The material which is closer to the hole, however, exhibits a lattice constant which neither resembles MoS_2 nor TaS_2 but one in between.

Taking into account Vergards' law again and the results from chapter 4.2, it can be assumed that an alloy of $Mo_{(1-x)}Ta_xS_2$ is present close to the hole because the relative amount of Mo in the alloy is lowering the lattice constant. The change in lattice constant with distance to the hole points to a non uniform mixture. Assuming the Mo diffuses from the MoS_2, originally located in the area of the hole, into the TaS_2, created during the growth process, its concentration is likely highest closer to the hole, where it influences the lattice constant of the alloy the most. As diffusion is time and energy dependent, with increasing distance the relative amount of Mo in the alloy will decrease and eventually only TaS_2 will be present. This is corroborated by the observations. Vergard's law calculates an alloy of $Mo_{0.21}Ta_{0.71}S_2$ for the area close to hole an alloy of $Mo_0Ta_1S_2$, or simply TaS_2, for the area further away. However, its already discussed limitations have to be kept in mind.

4.3.3 Surface Coverage

There are several other ways besides moiré analysis to estimate the level of dilution and gather information about the diffusion process forming Kirkendall holes. The relative coverage rates of alloys and holes in comparison to CLHs grown with similar parameters can provide one of these insights. To evaluate the quantity to which the holes are directly linked to the areas which were covered by MoS_2 before the second preparation cycle, an evaluation of the areas covered by holes and alloys from preparations with Kirkendall holes, in comparison to MoS_2 cores and TaS_2 envelopes from said CLHs preparations was made. Two Kirkendall hole preparations have been chosen. They vary in the evaporation time of Ta with t_1 = 1 min 30 s and t_2 = 1 min. These in turn are compared to CLHs preparations which have an identical first preparation cycle and an evaporation time of Ta with t_2 = 1 min in the second cycle. The results of this coverage analysis are summarized in table 4.8.

Table 4.8: Relative area of either alloy, Kirkendall holes, or background, in the case of a Kirkendall preparations and areas covered by envelopes, core materials, or background in the case of CLHs preparations. The parameters t_1 and t_2 represent the time of Ta evaporation, with t_1 = 1 min 30 s and t_2 = 1 min.

	Kirkendall (t_1)	Kirkendall (t_2)	CLHs (t_2)
alloy/envelope	0.35	0.35	0.11
hole/core	0.04	0.02	0.07
empty	0.61	0.65	0.83
sum	**1.00**	**1.02**	**1.01**

The area covered by islands in the preparations with the Kirkendall effect is about three times the area covered by TaS_2 envelopes of comparable preparations with CLHs. Additionally, the area covered by holes is only a third of the area of the MoS_2 cores of those preparations. A comparison of the area covered by alloys to those covered by the sum of cores and envelopes finds 35 % coverage for the alloys of the preparations with the Kirkendall effect but only 18 % for the sum of structures in the preparations with CLHs. A simple estimation would expect a constant level of coverage between the two, as it is assumed that for the preparation with Kirkendall holes an alloy with a lattice constant between that of MoS_2 and TaS_2, similar to the results seen in chapter 4.2, is present. Even with a local variation in the relative mixture of the components, one should expect the surface coverage remain constant.

This difference might be explained by several reasons. First, due to measurement bias on areas with any material present or areas where the STM can physically measure, an uneven distribution of the islands might lead to an overestimation or underestimation of coverage. This holds especially true for preparations with locally varying island densities or, simply, bigger islands compared to preparations with more evenly distributed islands. This effect appears to be quite applicable, since preparations with the Kirkendall effect, in contrast to CLHs, present larger islands instead of many small islands, which indicates these areas of higher material concentration.

Second, the structure formed by the merger of Mo, from the MoS_2, with the applied Ta and S might be more complex. As discussed in chapter 4.2, an alloy of $Mo_{(1-x)}Ta_xS_2$ might not strictly adheres to Vergard's law, which would entail a constant coverage upon merger but could reach a non linear composition as seen in figure 4.12. Furthermore, the alloy present in the preparations with Kirkendall holes might not be a disulfide like the alloy in chapter 4.2. The alloy might be a monosulfide such as $Mo_{(1-x)}Ta_xS$, or even a trisulfide like $Mo_{(1-x)}Ta_xS_3$. Especially the monosulfide is not considered likely, however, due to the missing of additional moiré spots often exhibited in such cases [97, 65]. This leaves out the impact of defects and smaller vacancies, which could also play a role. Overall, the range of options is too large to declare a definitive reason for the discrepancies in the current dataset.

Comparing the area covered by Kirkendall holes to the area covered by MoS_2 cores in the CLHs preparations also shows a discrepancy. An area of (2-4) %, depending on the preparation, is covered by holes in the preparation with Kirkendall holes. However, 7 % is covered by MoS_2 cores in the CLHs preparations. Again, a difference of a factor of up to two. Besides the reasons mentioned above, an instinctually obvious cause might be that not all MoS_2 cores leave behind Kirkendall holes and some just form a uniform alloy with the surrounding material. An observation underlining this is shown in figure 4.22. In figure 4.22 a) an island stretches over the center of the image. The island exhibits two Kirkendall holes on the sides and an area of obvious mixture between a bright and a darker material in the center. The area is highlighted with a white box and shown in close up in figure 4.22 b). The dark material resembles MoS_2 and still exhibits some moiré spots, while the bright material is similar in structure to TaS_2 or $Mo_{(1-x)}Ta_xS_2$. No unified area of MoS_2 can be defined, as would be present

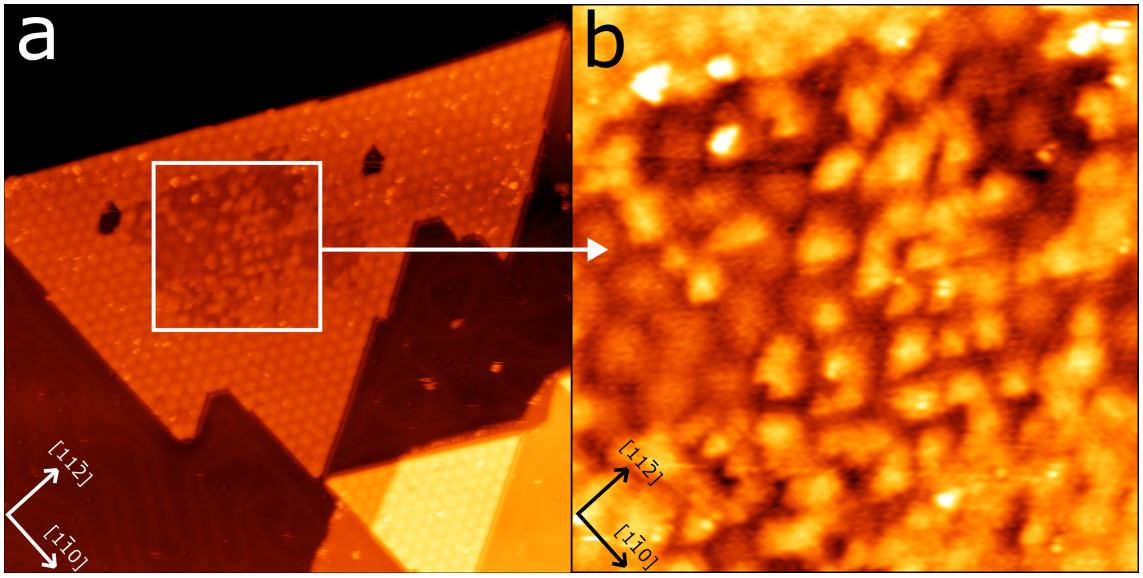


Figure 4.22: a) Islands with Kirkendall holes and obvious areas mixing, marked by a white box, on Au(111) surface, $U_{\text{bias}} = -0.5$ V, $I = 3 \times 10^{-10}$ A, dimensions: 85 nm × 85 nm; b) Close up of area of mixing highlited in *a)*, $U_{\text{bias}} = -0.5$ V, $I = 3 \times 10^{-10}$ A, dimensions: 24 nm × 24 nm.

for the MoS_2 cores in CLHs. It is obvious that a diffusion process has taken place in the center, yet the location shows no clear sign of a Kirkendall hole formation.

While clearly a difference exists between the area covered by holes and the area covered by MoS_2 cores in comparable CLH preparations, under the assumption that this difference is small, an estimation for the relative amount of components of an ideal alloy can be made in analogue to chapter 4.2. This, for now, assumes that all holes used to be MoS_2, which have then dissolved into the surrounding regions evenly and are the sole supplier of Mo.

The results are based on the values in table 4.8. In the first step, the area of the holes needs to be subtracted from the area covered by the alloys, since the alloy is assumed to contain the MoS_2 which was once in the holes. This leaves us with an area equivalent to the expected TaS_2 coverage.

The area equivalent to the MoS_2 coverage, here the area of the holes, divided by the area of a unit cell of MoS_2 calculates the amount n_{Mo} of Mo atoms present on the surface. Afterwards the TaS_2 area can be divided by the area of a TaS_2 unit cell, resulting in the equivalent amount of n_{Ta} Ta atoms. The ratio of Mo and Ta atoms can then be used to calculate x in $Mo_{(1-x)}Ta_xS_2$. The calculation is shown in accumulated form in the equation below.

$$A_{\mathrm{TaS_2}} = (A_{\mathrm{alloy}} - A_{\mathrm{hole}}), \tag{4.14}$$

$$A_{\mathrm{MoS_2}} = A_{\mathrm{hole}}, \tag{4.15}$$

$$n_{\mathrm{Ta}} = \frac{A_{\mathrm{TaS_2}}}{A_{\mathrm{TaS_2\text{-}unit\text{-}cell}}}, \tag{4.16}$$

$$n_{\mathrm{Mo}} = \frac{A_{\mathrm{MoS_2}}}{A_{\mathrm{MoS_2\text{-}unit\text{-}cell}}}, \tag{4.17}$$

$$\frac{n_{\mathrm{MoS_2}}}{n_{\mathrm{MoS_2}} + n_{\mathrm{TaS_2}}} + \frac{n_{\mathrm{TaS_2}}}{n_{\mathrm{MoS_2}} + n_{\mathrm{TaS_2}}} = 1. \tag{4.18}$$

Together with

$$(1 - x) + x = 1, \tag{4.19}$$

as in $\mathrm{Mo_{(1-x)}Ta_xS_2}$ follows:

$$1 - x = \frac{n_{\mathrm{MoS_2}}}{n_{\mathrm{MoS_2}} + n_{\mathrm{TaS_2}}}, \tag{4.20}$$

$$x = \frac{n_{\mathrm{TaS_2}}}{n_{\mathrm{MoS_2}} + n_{\mathrm{TaS_2}}}, \tag{4.21}$$

and with equation 4.15 and equation 4.16

$$x = \frac{(A_{\mathrm{alloy}} - A_{\mathrm{hole}})}{A_{\mathrm{hole}}} \frac{A_{\mathrm{MoS_2\text{-}unit\text{-}cell}}}{A_{\mathrm{TaS_2\text{-}unit\text{-}cell}}}. \tag{4.22}$$

This leads to the results summarized in table 4.9.

Table 4.9: Estimation for $\mathrm{Mo_{(1-x)}Ta_xS_2}$ by area analysis and the expected lattice constant for the mixture according to Vergard's law for the preparations with Kirkendall holes done with evaporation times t_1 = 1 min 30 s and t_2 = 1 min.

	x	(1-x)	Expected lattice constant [nm]
t_1	0.14	0.86	0.3280
t_2	0.13	0.87	0.3281

The expected values of the lattice constants a_{t_1} = 0.3280 and $a_{t_2} = 0.3281$ are very close to the values measured for the alloy in close proximity to the hole of figure 4.21, yet indicate, as assumed, less presence of $\mathrm{MoS_2}$.

Based on the rates of evaporation, preparations with a Ta evaporation time of t_1 should result in $Mo_{0.45}Ta_{0.55}S_2$ and preparations with a Ta evaporation time of t_2 in $Mo_{0.36}Ta_{0.64}S_2$, which are distinctively different from the results achieved. While this difference might be explained by due to Vergard's law possibly understating the amount of Mo in the mixture (see figure 4.12), these two results are also in accordance with the earlier stipulation that not all MoS_2 islands leave behind Kirkendall holes, or holes of the same size. Some of these islands might just diffuse into the surrounding alloy seamlessly.

To gain further insights on this topic, the following section will present a growth model under consideration of the theoretical aspects of diffusion.

4.3.4 Theoretical Analysis and Proposed Model Growth Process

The Kirkendall effect necessitates two things: Vacancies and a difference in the ability of these vacancies to move in conjoined materials. The two conjoined materials present during the preparation were MoS_2, from islands grown in the first preparation cycle, and TaS_2, which starts its growth at those islands during the second preparation cycle. Using DFT calculations, kindly supplied by Francis H. Davies and Arkady V. Krasheninnikov, the vacancy mobility in those two materials can be compared. The results of these calculations can be seen in figure 4.23.

Figure 4.23 shows the energy barriers for vacancy diffusion inside of MoS_2 and TaS_2, in relation to reaction coordinates. MoS_2 is shown in pink and TaS_2 in light blue. The reaction coordinates describe the diffusion path alongside which the energy is calculated and are explained further by three insets at the top of the image. The inlets show a generalized 2H TMDC in top view. Sulfur atoms are shown in yellow and metal atoms in purple. On the left, the initial geometry of a vacancy in the metal sublattice is shown together with a red arrow indicating a metal atom and the position it will move to. The inset in the middle shows a metastable intermediate structure, resulting from the movement indicated in the first inlet, whose local binding pattern is very similar to that of a 4|4 P mirror twin boundary [121]. Again, a red arrow indicates the metal atom and its next position. The third inset, located on the right, shows the final structure where the metal atom has now moved one lattice constant in zigzag direction to the left and consequently has moved a vacancy similarly to the right. The overall movement is in principle a two step process through the metastable intermediate state, however,

while the energy barriers are very different, in praxis the bigger barrier will heavily dominate the process. The following conclusions are therefore only based on this bigger barrier.

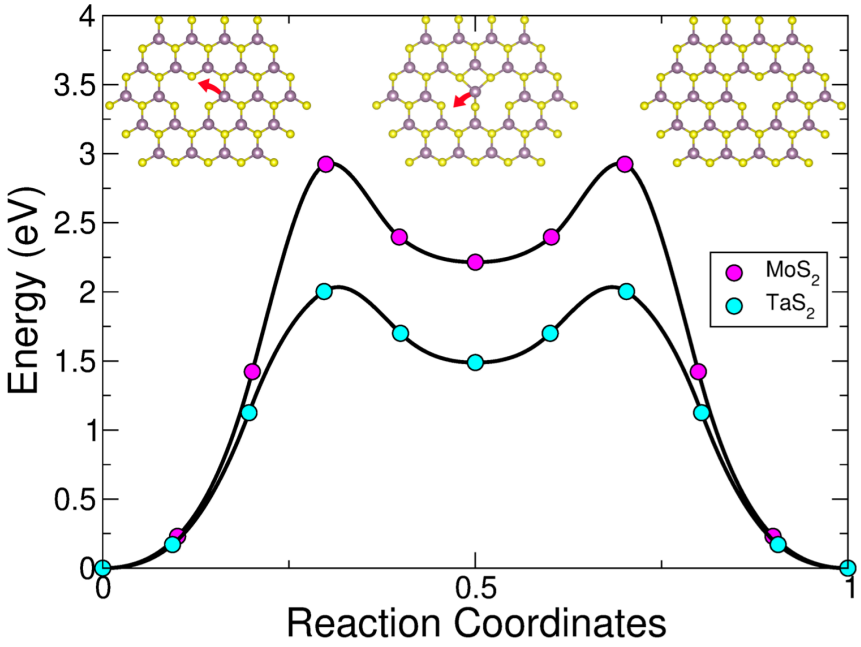


Figure 4.23: Energy barrier for vacancy diffusion in MoS_2 and TaS_2 depending on the reaction coordinate. Reused with permission from [120].

The energy barriers of MoS_2 and TaS_2 show that the movement of vacancies takes significantly more energy in the MoS_2, with a barrier maximum of $E_{b,\,MoS_2}$ = 2.93 eV than in the TaS_2, which has a barrier at its highest point of $E_{b,\,MoS_2}$ = 2.03 eV. Therefore vacancies can move with a high frequency and speed in the TaS_2 but as soon as they reach an area of MoS_2 the vacancy movement slows down drastically. The scope of difference in movement speed can be assessed by the diffusion jump rate according to the Arrhenius law

$$v = v_0 e^{\frac{-E_B}{k_b T}}. \quad [122] \tag{4.23}$$

Here a common attempt frequency $v_0 = 10^{12}\ \frac{1}{s}$ is assumed [123, 124]. An exact number is not necessary as the outcome is heavily dependent on the temperature. At 900 K, as was utilized during the growth process, this results in a diffusion jump rate in TaS_2 of v_{TaS_2} = 4.3 Hz, while in the MoS_2 the diffusion jump rate is only $v_{MoS_2} = 3.9 \times 10^{-5}$ Hz. This constitutes a difference of six orders of magnitude. The vacancies therefore collect inside the MoS_2 until enough vacancies accumulate to form a hole.

Information about the energetics of the system were also acquired from the DFT calculations. Creating an Mo impurity by moving a vacancy from TaS_2 into the MoS_2 increases the energy of the system by ΔE_1 = 1.9 eV, while the opposite process, of moving a vacancy from the MoS_2 into the TaS_2 and creating a Ta impurity in the MoS_2, lowers the energy of the system by ΔE_2 = -1.8 eV. According to these energetics, the vacancies should accumulate in the TaS_2. While this opposes the kinetics presented earlier, the experiment clearly shows the accumulation of vacancies inside the MoS_2. The kinetics are therefore indicated to be the dominant factor in this process. The apparent contradiction can be explained by the fact that the results for the energetics hold true at thermodynamic equilibrium, a state which is not present during or after the growth process, as it would necessitate effective diffusion of vacancies in both materials. Dependent on the enthalpy of mixing, a thermodynamic equilibrium would not exhibit a gradient of diffusion throughout the material, as seen in figure 4.21, but either a homogeneous alloy or a clear phase separation. This is further emphasized by the second necessity for the Kirkendall effect, which is an ample supply of vacancies. It is well established that the formation energies in the metal sublattice of TMDCs like MoS_2 is high, even in a chalcogen rich limit [125]. This in turn means that the defect density in thermodynamic equilibrium is low. The equilibrium fraction of vacancies can be calculated with

$$n_{\mathrm{V}} = e^{\frac{-Q_{\mathrm{V}}}{k_{\mathrm{B}}T}}. \tag{4.24}$$

Here electronic, entropic, and vibrational contributions to the Gibbs energy are neglected. The parameter Q_{V} denotes the formation energy of the vacancies, which has been calculated for MoS_2 as $Q_{\mathrm{V,\,MoS_2}}$ = 5.45 eV and for TaS_2 as $Q_{\mathrm{V,\,TaS_2}}$ = 5.82 eV. The resulting vacancy fractions at both RT (300 K) and the temperature during the growth process (900 K) are summarized in table 4.10.

Table 4.10: Equilibrium fraction of vacancies for MoS_2 and TaS_2 at 300 K and 900 K.

	300 K	900 K
$n_{\mathrm{V,\,MoS_2}}$	2.8×10^{-92}	3.0×10^{-31}
$n_{\mathrm{V,\,TaS_2}}$	1.7×10^{-98}	2.5×10^{-33}

It is very obvious that even at an elevated temperature no vacancies are found in thermodynamic equilibrium, as one would be unlikely to find even a single vacancy on the whole sample. However, many vacancies must be present in the system, enough even to form Kirkendall holes. This is another indicator that the growth process has to take place far away from this equilibrium.

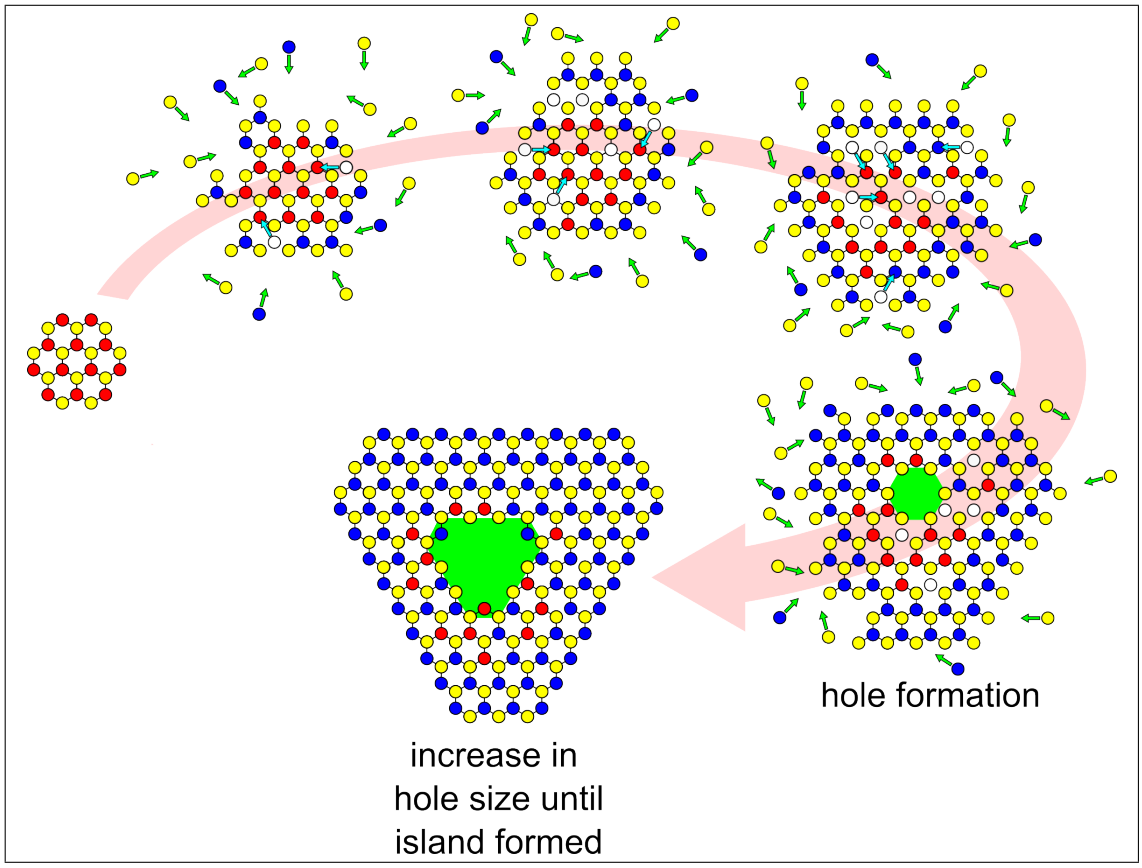


Figure 4.24: Schematic of the creation of Kirkendall holes during the island formation process. Ta is applied in a highly sulfurised environment, leading to the formation of Ta_xS_2 with $x < 1$. The resulting Ta vacancies have high mobility until they reach and area of MoS_2, where they slow down and become trapped. Reused with permission from [120].

The origin of these vacancies is likely to be found in the way the growth process is structured, as illustrated in figure 4.24. During the first growth cycle free-standing MoS_2 islands were created, while the second cycle added Ta and S (as part of the H_2S gas). It is assumed from the experimental results that these components try to form TaS_2 at the edges of the MoS_2 islands, in a process similar to the formation of CLHs. The relative amount of S is high compared to the Ta which is present. Our model suggests that, due to the large surplus of S, every

Ta atom is quickly sulfurized. This happens to such a degree that diffusion paths along the structure become blocked and the newly grown structures are momentarily locked in place, leading to further growth at these positions. This disorderly growth introduces vacancies at the edges. These vacancies can then move quickly in the TaS_2 but become trapped when they reach an area of MoS_2, where they then accumulate. If enough vacancies, in this case three, collect in an area they can break the all bonds which used to link the sulfur in the top and bottom layer of the TMDC to metal atoms, forming a hole. The following chapter shows this process in more detail via a Monte Carlo simulation.

4.3.5 Monte Carlo Simulation

While figure 4.24 already gives a good overview of the proposed formation process of Kirkendall holes in $Mo_{(1-x)}Ta_xS_2$ alloys, the model can be shown in more detail via a simple Monte Carlo simulation and, with the input of data from the DFT calculations mentioned earlier, also given more weight. The rules of the simulation can be found in chapter 3.4.3 and the corresponding Python code in the appendix (see chapter 7).

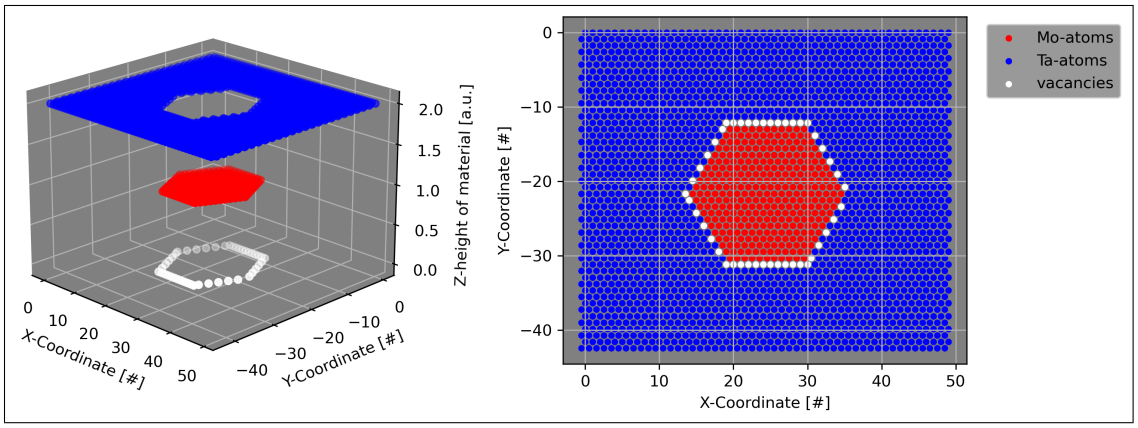


Figure 4.25: Starting position of the Monte Carlo simulation. Mo atoms are shown in red, Ta atoms in blue and vacancies in white. Left: Shows a representation at different heights. With Ta atoms at a height of two, Mo atoms at a height of one and vacancies at a height of zero. These heights illustrate the different apparent heights in the STM but have no material impact on the simulation; Right: In plane projection of the construction shown on the left.

The simulation took place inside the metal sublayers of the TMDCs only and had three base components: Mo atoms, Ta atoms and vacancies. This effectively simulates the unit cells of the experiment, while excluding the sulfur. To mimic the conditions of the experiment, the simulation started with a hexagonal core of Mo atoms. Placed at its border were varying amounts of vacancies. The rest of the area was filled with Ta atoms. While the location and amount of vacancies can have an influence on the exact outcome of a simulation, the general behavior should mostly be independent and an arbitrary amount was chosen. These starting conditions are shown in figure 4.25.

The simulation evolved iteratively, abiding by its rules, until a set limit of evolutions was reached or no more movements were allowed. Figure 4.26 shows an example run in the projection of figure 4.25 (right), with snapshots taken during the evolutionary process.

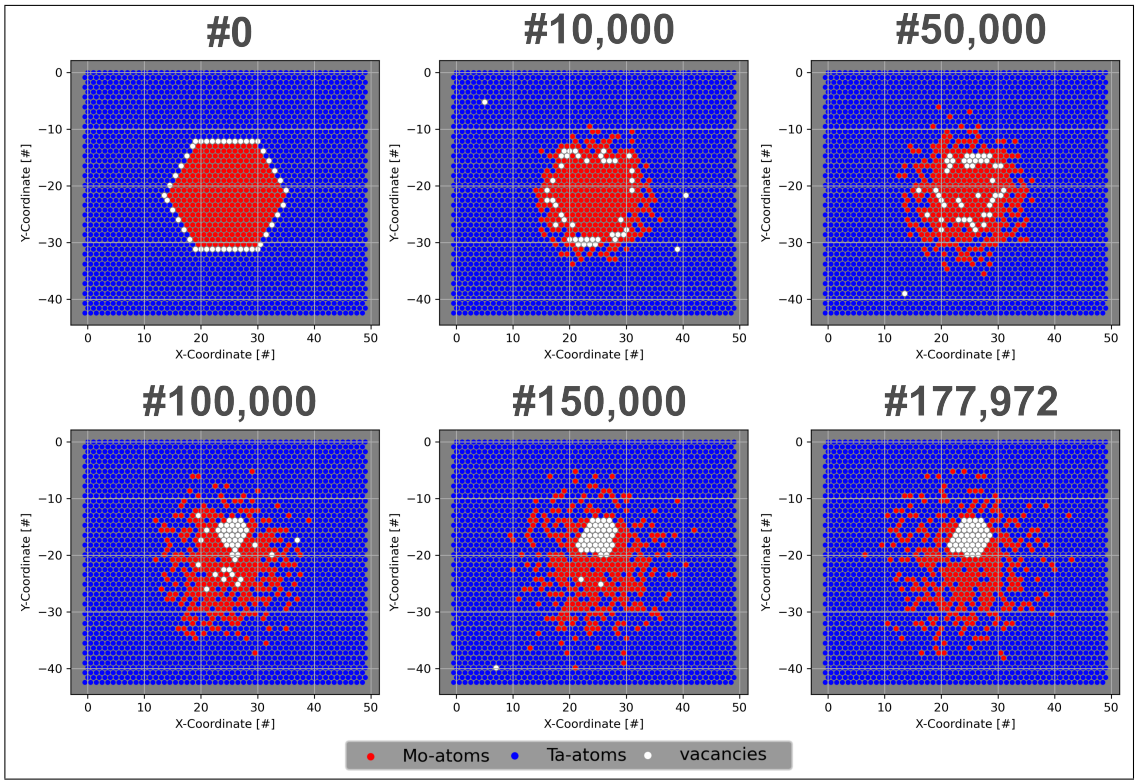


Figure 4.26: Evolution of the simulation by iterations. The current is iteration is denoted by the number above each image. The starting position is in the top left at iteration zero. Mo-atoms are drawn in red, Ta-atoms in blue and vacancies in white. With each step the vacancies move over the surface and eventually get trapped in the Mo-rich areas until they loose all of their mobility and get trapped there. The simulation ended, when no more movement was possible.

In the top left, enumerated with zero, the starting position is shown. The picture to its right displays the state after 10,000 iterations. Most of the vacancies already accumulated inside the Mo-rich area, where their movement is very slow. The process of vacancy diffusion also moved Mo atoms into areas originally only occupied by Ta and vice versa. This movement continues until enough vacancies accumulate inside a small area, forming a structure where no movement is allowed for any of its constituents. For this to happen, every vacancy needs to have three vacancies as nearest neighbors. The smallest structure where this is the case is a hexagon.

After 50,000 iterations, several groups of vacancies have accumulated in the upper part of the Mo-rich area. However, not all of them have grown into a stable structure and some might leave in future iterations, in turn also lowering the neighbor count of their neighbors and allowing them to move again. Yet, a stable hexagon has already formed, creating a permanent hole. The diffusion of the Mo

into the areas originally covered by the Ta continued.

After 100,000 iterations, the non-permanent structures did indeed dissolve again. The hexagon anchoring the hole, on the other hand, has grown significantly. It serves as a reliable source of nearest neighbors, allowing vacancies to collect around it and become themselves immovable, growing the structure further. Atoms of Mo have continued to diffuse away further from their original source.

At 150,000 iterations, most of the vacancies have been collected at the hole and, again, the diffusion of the Mo into the surrounding area has expanded further. As 177,972 iteration have been reached, all vacancies have collected at the hole and the simulation has stopped since no more movement was possible. The diffusion of Mo and Ta has therefore also stopped.

Overall, the vacancies spend most of their time in Mo-rich areas. This is expected as their diffusion coefficient is significantly reduced in those areas. It could be seen that a hole started slightly below the border between the Mo- and Ta-rich areas. Over time it collected all the vacancies and grew until no more movement was possible. The movement of the vacancies themselves caused a mixing between the Mo and the Ta. While Ta also diffuses into the starting positions, originally only filled by Mo atoms, due to the displacement by Mo atoms with vacancies in those areas, more Mo atoms diffuse into areas originally only covered by Ta. However, the distance the Mo atoms travel is a statistical process dependent on chance and the time of the diffusion process. With increasing time, Mo disperses further into the Ta. At the end of the simulation, when no more vacancies were available to facilitate movement, a gradient had formed with a higher concentration of Mo close to the starting hexagon of the Mo atoms and a decreasing concentration with distance to it. As the hole, which had formed, is not located in the center of this area, this gradient is not isotropic when measured away from its location.

Comparing these results to figure 4.20 d) and e), good agreement with the results of the experiment can be found. The supplied vacancies eventually formed a hole inside an originally Mo-rich area. The shape of the hole, due to the chosen stable hole configurations, grows roughly hexagonal but is highly dependent on the local vacancy supply and may grow extensions on its sides, an effect neatly observed in those images.

The creation of a diffusion gradient for the Mo, centering on the origin of the Mo atoms, which represents the MoS_2 islands in the experiment, and decreasing with distance, is in analogue to observations from figure 4.21. While chapter 4.3.2 analyses this gradient in reference to the position of a hole and assumes it to be roughly the center of the source of the Mo atoms, the idea that this gradient is not necessarily isotropic around such a hole is also sensible. Since Kirkendall voids are known to grow in the border region of two materials with varying diffusion coefficients [86], it is likely that the holes also often grow in those regions in 2D space. This alone causes an isotropy of the diffusion coefficient between the two sides of the hole, as it would not be centered in the source of the Mo atoms. Furthermore, the hole can block the path of diffusion for Mo atoms, from an area of high concentration on one side to an area of low concentration on the other side, as a vacancy exchange mechanism is not possible in an area where no lattice is present.

In summary not only good agreement is found between results of the experiment and the simulation but the process of hole formation by vacancy diffusion was further highlighted. An interesting point which was illustrated, is the location of the holes and the resulting anisotropy of the diffusion gradient relative to the hole. While not enough data is present to investigate this now, analyses of anisotropy around Kirkendall holes could indicate if the formation in the 2D realm takes place in the border region, too. This shows that even with a simple simulation the growth process can be adequately reconstructed and further avenues of investigation can be highlighted.

4.3.6 Conclusion

The formation of Kirkendall holes, as the 2D equivalent of the 3D Kirkendall voids, was observed in the growth process of $Mo_{(1-x)}Ta_xS_2$ alloys. It could be shown that these holes accumulate in the areas originally occupied by MoS_2, grown in the first cycle of the preparation. This exemplifies that the growth processes, leading to the formation of 2D alloys are as vacancy driven as their 3D counterparts. The formation of such holes necessitates different vacancy mobilities in two adjoined materials, which has been shown by DFT calculations, and an ample supply of vacancies. While no supply of vacancies is expected at thermodynamic equilibrium, a growth model could be proposed, showing the intricate growth process supplying such vacancies. This, together with the high-temperature environments, concludes that the system is far away from such an equilibrium. The feasibility of this model has been further tested by application to a Monte Carlo simulation, whose results very much aligned with the experiments.

The insights from this growth model are also applicable to the general growth of many TMDC alloys, as were presented for example in chapter 4.2, while the Kirkendall holes itself extend the possibilities for in-plane growth processes further. The voids formed by the holes, could, for example, be filled with other materials, circumnavigating possible boundaries in different growth processes.

4.4 Kagome Lattice

As already mentioned in chapter 4.2, during the preparation of $Mo_{(1-x)}Ta_{(x)}S_2$ alloys, an additional structure of interest was realized. This structure was consequently named *Kagome*, due to its crystal structure, a term coined by Kôdi Husimi and first used in a publication by Ichirō Shōji, originally describing a bamboo-basket woven pattern [126]. The structure appears in other preparations as well. This chapter will give a short summary of that structure and the possible uses of the material.

4.4.1 Preparation and Resulting Structures

While the kagome structure can be observed as a byproduct of many preparations containing Tantalum, parameters for preparations resulting in large areas of kagome will be summarized here for quick reference. Large kagome structures could be achieved by first evaporating Tantalum with an evaporation rate of 0.01 ML/min for 50 s. Following this, the sample was annealed in H_2S at a pressure of 1×10^{-7} mbar at 1000 K for 20 min. Afterwards, the sample was cooled down and when a temperature of 450 K was reached the H_2S supply was shut off. No second cycle was applied. An illustration of the active parameters over time are shown in figure 4.27 and they are summarized for quick reference in table 4.11 again.

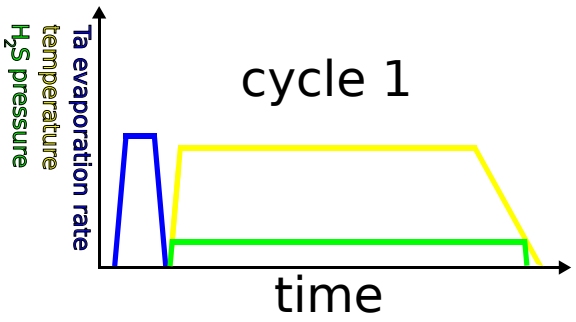


Figure 4.27: Schematic of active parameters for preparation with large areas of kagome, over time: Evaporation of Ta (blue); presence of H_2S (green), high temperatures (yellow).

Table 4.11: Parameters for preparations resulting in the large areas of a kagome structures.

	Ta	
T_{evap}	300 K	
t_{evap}	50 s	
R_{evap}	0.06 ML/min	
P_{evap}	-	
T_{anneal}	1000 K	
t_{anneal}	20 min	
$P_{H_2S,\ anneal}$	$1 \cdot 10^{-7}$ mbar	

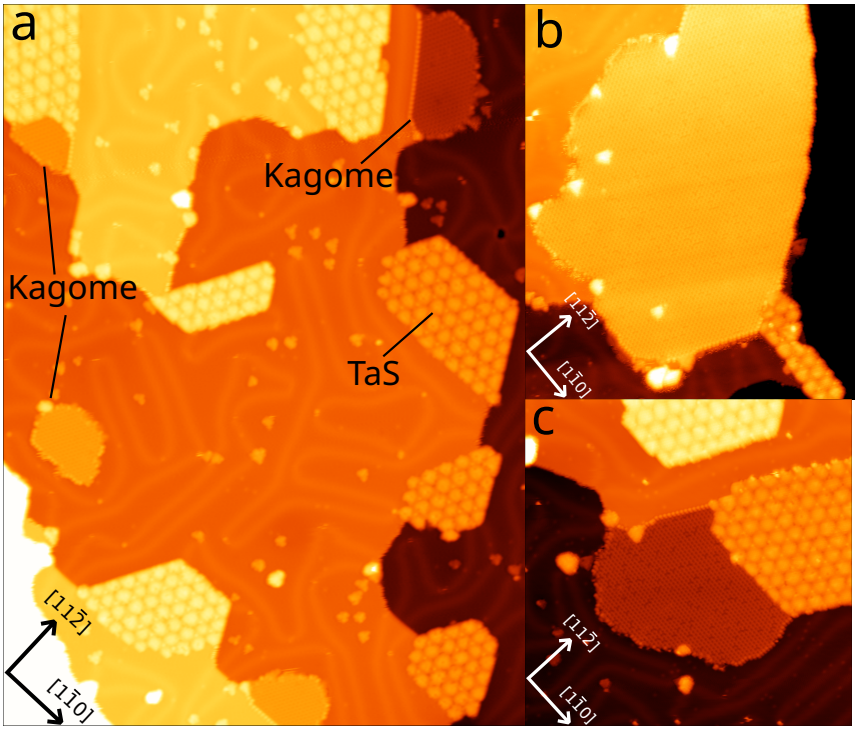


Figure 4.28: STM images of: a) Kagome lattices and TaS islands located on different steps of the Au(111) surface, $U_{bias} = -1.6$ V, $I = 1 \times 10^{-9}$ A, dimensions: 67 nm $\times$ 92 nm; b) Large area Kagome lattice, $U_{bias} = -0.4$ V, $I = 3 \times 10^{-10}$ A, dimensions: 42 nm $\times$ 51 nm. c) Close up of Kagome lattice adjoined to TaS island and Au(111) step, $U_{bias} = -0.5$ V, $I = 3.4 \times 10^{-10}$ A, dimensions: 45 nm $\times$ 45 nm.

Figure 4.28 shows some results of these preparations. In figure 4.28 a) a large area of the Au(111) surface is displayed. Several steps are present, distinguishable by the changes in brightness. The characteristic herringbone reconstruction is visible on all of these steps. Located on these steps are two structures. The first is an island structure, exhibiting a moiré with additional spots. Due to these spots, and application of Ta in a low sulfur environment, these islands are identified

as TaS according to [97, 65]. Additionally to these islands, several patches of the kagome structure are present on the surface. These patches can be freestanding, connected to a step or connected to a TaS island (see also figure 4.28 c)). Sizes of these patches vary from 10 nm to 50 nm in diameter. A larger patch is shown in figure 4.28 b). None of the kagome structures exhibit a moiré superstructure and all of them must therefore be commensurate with the Au(111) surface. The patches of the kagome structure are always round or oval in shape and tend to express adsorptions of material at the edges, for which, due to the behavior of other monolayers, a likely candidate is sulfur [127].

4.4.2 Structure and Analysis

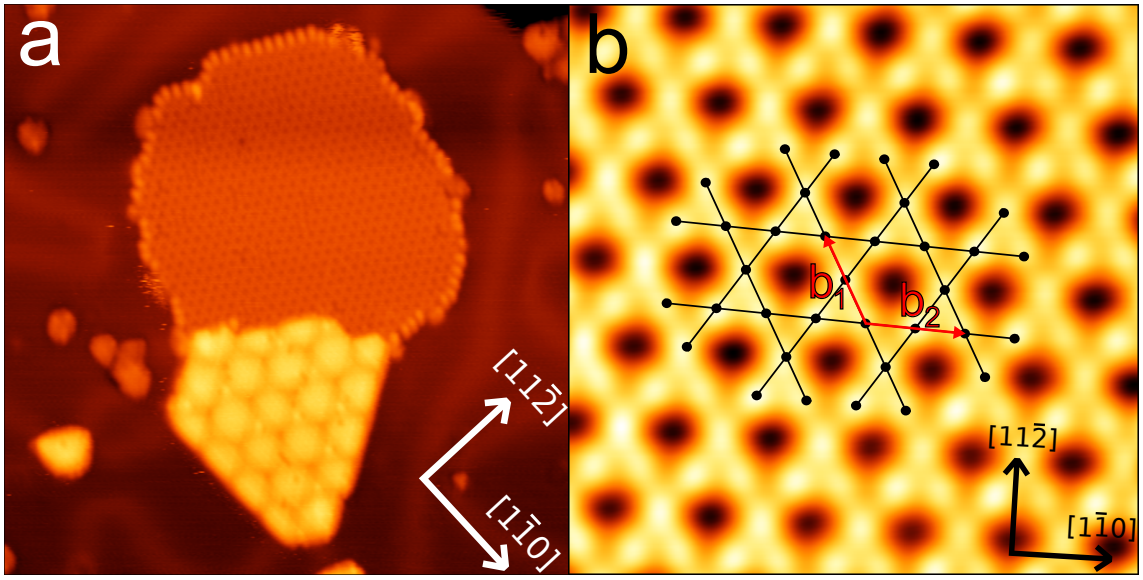


Figure 4.29: STM images of: a) Kagome lattice adjoined to TaS island, $U_{\text{bias}} = -0.8$ V, $I = 4.5 \times 10^{-10}$ A, dimensions: 30 nm × 30 nm.; b) Close up of a kagome lattice with part of the lattice highlighted in black and two lattice vectors marked in red, $U_{\text{bias}} = -0.5$ V, $I = 3 \times 10^{-10}$ A, dimensions: 3.23 nm × 3.23 nm, Fourier-filtering techniques applied.

Figure 4.29 a) shows an example of the kagome lattice, connected to an island of TaS. In figure 4.29 b) another kagome lattice is shown in a close up. To better visualize the structure, part of the lattice is highlighted in black and two lattice vectors $\vec{b_1}$ and $\vec{b_2}$ are shown. The apparent lattice is a 2D-hexagonal Bravais lattice with a three-atomic basis. To accurately determine the two lattice vectors, images with a kagome lattice and a known structure are necessary. Assuming the other structure in figure 4.29 a) to be TaS with a known moiré

periodicity of (2.26 ± 0.06) nm [97], it can be used as a tool for normalization. Using this normalization, the two lattice vectors are determined to be $\vec{b_1}$ = (0.628 ± 0.004) nm and $\vec{b_2}$ = (0.591 ± 0.002) nm, with the error as the standard deviation plus measurement uncertainties. The difference between the two values already indicates problems with the normalization. There is a significant difference between the two, which, while not impossible, is unlikely for a kagome structure. It is possible that the adjacent structure does not fully conform to the morphology of TaS or that not enough area was present for a proper normalization. Influences like the piezo drift and other offsets of the measurement can also have an impact on the uncertainty, which cannot be evaluated. The lattice constants of the real structure are estimated to be in the size range of $\vec{b_1} = \vec{b_2} \approx 0.61$ nm.

4.4.3 Conclusion

The kagome structure is an interesting byproduct of many preparations including Tantalum. After first observations, the question of focused synthesization quickly arose. A reliable recipe was deduced, able to grow large patches of kagome, including completely freestanding islands. The fact that the preparation only includes Tantalum and H_2S infers that the kagome is also likely a composite of these two. The lattice constant of the kagome structure could be roughly estimated but further study is needed to increase the accuracy of the result. Furthermore, the existence of this structure underlines the vast possibilities to grow structures with even limited available components, such as only Ta and S. One use already apparent, due to its regular appearance in the growth of other structures, is as a tool of normalization itself, as soon as its lattice constants are known with a high enough accuracy. More detailed questions like specific composition, electronic structure and more uses and applications will be answered in other interesting and ongoing investigations.

CHAPTER 5

SUMMARY

This thesis investigated various monolayer structures on an Au(111) surface, grown with Mo, Ta, and S. The range of options for these three components to grow structures and interact with each other is great. This includes, but is not limited to, the formation of concentric lateral heterostructures, the creation of alloys, the kagome structure, and the development of the Kirkendall holes.

- **Concentric lateral heterostructures** form when one TMDC encloses another during its growth process. Here, MoS_2 has been grown, forming a source of nucleation, and TaS_2 has been attached to it in a second step, creating a seamless connection between an TaS_2 envelope and an MoS_2 core. This was achieved even though a lattice mismatch of about 4.53 % exists. While the growth process for this had already been established in [26], question about the nature of the interface still had to be answered. Due to the structure of the involved materials, two types of possible interfaces emerged. An M_{in}-X interface (or Mo-S interface due to the actually present elements), wherein the MoS_2 core terminates in an Mo atom and is connected to an S atom from the surrounding TaS_2 and an X-M_{out} (or S-Ta) interface where the MoS_2 terminates in an S atom and is connected to a Ta atom from the surrounding TaS_2. The characteristic distribution of pure MoS_2 islands between the fcc and hcp areas of the Au(111) surface, together with their known stacking order in those [109], could be used to identify these interfaces, as it was shown that the distribution was conserved after the islands were grown into CLHs. This means that the edge terminations of the MoS_2 cores would directly dictate the type of interface, as no defects were observed. The interconnection of the two materials exhibiting a significantly different lattice constants is only possible if a compensation mechanism is present. Usually this is accomplished by the periodic introduction

of defects. This was not the case. It could be shown that a deformation was present to compensate for the material stresses introduced by the connection. Results demonstrate that the MoS_2 only has a small isotropic expansion, independent of the interface investigated, while the surrounding TaS_2 contracts it lattice constant significantly when connecting at an S-Ta interface and relaxing its lattice constant with distance, interestingly, not only to its equilibrium size but even extending itself. At an Mo-S-interface the lattice constant of the TaS_2 contracts to match the MoS_2.

- **The creation of $Mo_{(1-x)}Ta_xS_2$ alloys** has been observed, when Ta was added to MoS_2 and then annealed. At lower temperatures this created structures comparable to CLHs with areas of MoS_2 in the middle and an alloyed structure surrounding it, indicating that Ta had either alloyed into existing MoS_2 islands or taken sulfur components from them to form structures similar to TaS_2. With an increase in temperature the amount of alloyed structures increased and the areas identifiable as the original MoS_2 decreased, until only one type of alloy structure was observed. Analysis of the lattice constant, under the general assumption that Vergard's law held true, indicated that with an increase in temperature the relative amount of Mo in the alloy also increased. This happened until, at a critical temperature of 1050 K, only one structure, also holding the highest relative amount of Mo, was present. Using a combination of coverage and moiré analyses the most likely structural formula was deduced as $Mo_{(1-x)}Ta_xS_2$.

- **Kirkendall holes**, as the 2D equivalent of the 3D Kirkendall voids, have been discovered in a special growth process of $Mo_{(1-x)}Ta_xS_2$ alloys. The addition of Ta in a heated H_2S atmosphere on pre-existing MoS_2 islands causes a diffusion process and results in the formation of these Kirkendall holes. This necessitates a difference in diffusion coefficients and an ample supply of vacancies. DFT calculation have shown that the vacancies have a high mobility in the TaS_2 and a low mobility in the MoS_2, which causes them to effectively become trapped in MoS_2 rich areas during the growth process. While no vacancies would be present between the two materials in thermodynamic equilibrium, a model was presented showing that the special method of growth supplies enough vacancies to facilitate the formation of Kirkendall holes. Assumptions of this model were utilized in a Monte Carlo simulation to contextualize this process and good agreement was found.

- **The Kagome lattice** is a 2D hexagonal Bravais lattice with a three atomic basis, which appears as a byproduct of many growth processes presented in this dissertation. A dedicated growth process could be developed, growing large islands of this structure and reducing the candidates of its composition to Ta and S. Via topography analysis, the lattice vectors of the structure were estimated to be around $\vec{b_1} = \vec{b_2} \approx 0.61$ nm. While no further analysis has been done in this thesis, the Kagome lattice is useful due to its regularity and the ease with which it can be measured, making it valuable to calibrate STM images.

CHAPTER 6

OUTLOOK

The realm of TMDC monolayers on an Au(111) surface is vast and exhibits various structures of great interest for further study and applications. This thesis focused on TMDCs with Mo, S, and Ta. Starting with CLHs, MoS_2-TaS_2 CLHs have been investigated. But the world of TMDCs is not limited to these three compounds. WS_2 and TaS_2 can also exhibit CLH [26]. The lattice constant mismatch in this combination is virtually identical to MoS_2 and TaS_2[40, 64, 128]. Therefore, it might be of interest to examine the behavior at the interface of these materials as well. Many more contenders for heterostructure formation arise, introducing VS_2, $MoSe_2$, $TaSe_2$ just to name a few. Additional structures might be grown by expanding the amount of materials involved, since the cyclic growth process is easily expanded, CLHs with three, four, five or many more materials seem possible. The preference to grow in plane does not hold true for all material combinations and growth orders must be tailored to each individual combination [26]. This offers not only new challenges but also new opportunities. With the right choice of material and substrate, CLHs might be combined in the z-direction opening the door further for epitaxial device manufacturing. Preferences of different materials to grow on certain others, when grown in the right order, might be used to fine tune the stacking behavior, while temperatures and chalcogen supply can switch between CLHs, alloy, or alloy with Kirkendall holes. These Kirkendall holes in turn can be filled with other materials, which might then prefer to grow on the layer beneath, revealed through these holes. This could create growth stencils, forcing materials into shapes and combinations usually unfavorable for them.

Alloying between TMDCs shows similar promise. Not only changes in physical structure can occur, which opens the door to the tuning of structural parameters like the lattice constant, specific doping for desired bandgaps might be possible by adjusting the amount of dilution through temperature or supply of materials [129, 130]. Even alloys with continuous gradients over large lengths could be achieved. During these growth processes, unforeseen structures, similar to the kagome structure, might appear. This structure itself is interesting but goes vastly unresearched in this dissertation. Electronic and structural analysis is of interest, unlocking the compounds it consists of and its behavior.

While many avenues of growth and combination within the rich TMDC landscape have been investigated in this dissertation, leading to complex and interesting new insights, even more have opened up, giving opportunities for research in the years to come.

CHAPTER 7

APPENDIX

The base of the python code to create the Monte Carlo simulation is appended here. Small variation to create different starting positions shown in section 4.3.5 are not appended here to shorten the attachment.

```
# -*- coding: utf-8 -*-
"""
Created on Fri Jul  5 21:27:43 2024

@author: kaime
"""

import plotly.graph_objects as go
import sys
import numpy as np
import random
import math
from scipy.interpolate import griddata
import matplotlib.pyplot as plt
import matplotlib.gridspec as gridspec
import traceback



def create_hexagonal(Laenge, Hoehe):
    # Liste erstellen die dann abwechselnd Listen mit Laenge und Laenge-1
    ↪  enthalten
    # dies hilft später beim hexagonal plotten
    hexagonal = []
    for i in range(Hoehe):
        if i % 2 != 0:
```

```
            hexagonal.append(np.zeros(Laenge))
        else:
            #need to be same length
            hexagonal.append(np.zeros(Laenge))

    return(hexagonal)



def create_nn(zero_in_matrix, matrix):

    #define first and last row for easier reference
    first_row = 0
    last_row = len(matrix)-1

    #define fist and last atom in each row for easier reference
    first_atom = 0
    # only makes sense if rows have the same length
    last_atom = len(matrix[0])-1


    # create a list containing lists of each nearest neighbour for each
    ↪  later randomly chosen vacancy
    # global for checking purposes
    global list_NN_list
    list_NN_list = []

    for i in range(len(zero_in_matrix)):


        random_location_Y = zero_in_matrix[i][0]
        random_location_X = zero_in_matrix[i][1]

        # active to check the choices
        """
        print('This is the chosen one:')
        print('Y:' + str(random_location_Y))
        print('X:' + str(random_location_X))
```

```
63          print('value:' + str(matrix[random_location_Y][random_location_X]))
64          print(matrix[random_location_Y][random_location_X])
65          """
66
67
68          #make list of nearest neighbours
69          NN_list = []
70
71
72          # the nearest neighbours depent on the location of the vacancy. If
            ↪  at any border periodic boundary conditions
73          # have to be applied
74
75          # perdiodic boundary conditions
76
77          if random_location_Y == first_row and random_location_X !=
            ↪  first_atom and random_location_X != last_atom:
78              # this means we are at the very top, but also NOT in a corner
79              # Y-1 wraps around to bottom
80              # case 1
81
82
83
84              # movement upwards circles down to last
85              NN_list.append((matrix[last_row][random_location_X],
                ↪  (last_row,random_location_X)))
86              NN_list.append((matrix[last_row][random_location_X+1],
                ↪  (last_row,random_location_X+1)))
87
88              # these work as normal
89              NN_list.append((matrix[random_location_Y][random_location_X-1],
                ↪  (random_location_Y,random_location_X-1)))
90              NN_list.append((matrix[random_location_Y][random_location_X+1],
                ↪  (random_location_Y,random_location_X+1)))
91              NN_list.append((matrix[random_location_Y+1][random_location_X],
                ↪  (random_location_Y+1,random_location_X)))
```

```
92
                ↪ NN_list.append((matrix[random_location_Y+1][random_location_X+1],
                ↪ (random_location_Y+1,random_location_X+1)))
93
94
95
96
97          if random_location_Y == last_row and random_location_X !=
            ↪ first_atom and random_location_X != last_atom:
98              # this means we are at the very bottom, but also NOT in a
                ↪ corner
99              # case 2
100             # Y+1 wraps around to top
101
                ↪ NN_list.append((matrix[random_location_Y-1][random_location_X-1],
                ↪ (random_location_Y-1,random_location_X-1)))
102             NN_list.append((matrix[random_location_Y-1][random_location_X],
                ↪ (random_location_Y-1,random_location_X)))
103             NN_list.append((matrix[random_location_Y][random_location_X-1],
                ↪ (random_location_Y,random_location_X-1)))
104             NN_list.append((matrix[random_location_Y][random_location_X+1],
                ↪ (random_location_Y,random_location_X+1)))
105             #here:
106             NN_list.append((matrix[first_row][random_location_X-1],
                ↪ (first_row,random_location_X-1)))
107             NN_list.append((matrix[first_row][random_location_X],
                ↪ (first_row,random_location_X)))
108
109
110         if random_location_X == first_atom and random_location_Y !=
            ↪ first_row and random_location_Y != last_row and
            ↪ random_location_Y%2 != 0:
111             # this means we are on the very left but not in a corner, also
                ↪ of course not first or last row
112             # there are two cases. One for a row of even row and one for an
                ↪ even row
113             # this is for an odd row
114             # X-1 wraps around to rightmost position for three rows
```

```
115             # this is case 3
116
117
118
119             # this is top left nn -> wraps around to the last entry of the
                ↪  row above
120             NN_list.append((matrix[random_location_Y-1][last_atom],
                ↪  (random_location_Y-1,last_atom)))
121
122             # this is the top right nn
123             NN_list.append((matrix[random_location_Y-1][random_location_X],
                ↪  (random_location_Y-1,random_location_X)))
124
125             # nn position to the left wraps around to the very right
126             NN_list.append((matrix[random_location_Y][last_atom],
                ↪  (random_location_Y,last_atom)))
127
128             # nn to the right as normal
129             NN_list.append((matrix[random_location_Y][random_location_X+1],
                ↪  (random_location_Y,random_location_X+1)))
130
131             # the bottom left nn wraps around
132             NN_list.append((matrix[random_location_Y+1][last_atom],
                ↪  (random_location_Y+1,last_atom)))
133
134             # the bottom right nn is just the first in the next row
135             NN_list.append((matrix[random_location_Y+1][random_location_X],
                ↪  (random_location_Y+1,random_location_X)))
136
137
138         if random_location_X == first_atom and random_location_Y !=
            ↪  first_row and random_location_Y != last_row and
            ↪  random_location_Y%2 == 0:
139             # this means we are on the very left but not in a corner, also
                ↪  of course not first or last row
140             # this is for an even row
141             # here everything is normal but the left nn wraps around to the
                ↪  right
```

```
142             # this is case 4
143
144
145             NN_list.append((matrix[random_location_Y-1][random_location_X],
                ↪  (random_location_Y-1,random_location_X)))
146
                ↪  NN_list.append((matrix[random_location_Y-1][random_location_X+1],
                ↪  (random_location_Y-1,random_location_X+1)))
147
148             #left wraps around
149             NN_list.append((matrix[random_location_Y][last_atom],
                ↪  (random_location_Y, last_atom)))
150
151             NN_list.append((matrix[random_location_Y][random_location_X+1],
                ↪  (random_location_Y,random_location_X+1)))
152             NN_list.append((matrix[random_location_Y+1][random_location_X],
                ↪  (random_location_Y+1,random_location_X)))
153
                ↪  NN_list.append((matrix[random_location_Y+1][random_location_X+1],
                ↪  (random_location_Y+1,random_location_X+1)))
154
155
156
157         if random_location_X == last_atom and random_location_Y !=
            ↪  first_row and random_location_Y != last_row and
            ↪  random_location_Y%2 != 0:
158             # this means we are on the very right but not in a corner
159             # again even row and odd row has to be differentiated
160             # this is for an odd row
161             # case 5
162
163             # here just the right nn wraps around. rest normal
164
                ↪  NN_list.append((matrix[random_location_Y-1][random_location_X-1],
                ↪  (random_location_Y-1,random_location_X-1)))
165             NN_list.append((matrix[random_location_Y-1][random_location_X],
                ↪  (random_location_Y-1,random_location_X)))
```

```
166             NN_list.append((matrix[random_location_Y][random_location_X-1],
                ↪  (random_location_Y,random_location_X-1)))
167
168             # right wraps around to first atom
169             NN_list.append((matrix[random_location_Y][first_atom],
                ↪  (random_location_Y,first_atom)))
170
171
                ↪  NN_list.append((matrix[random_location_Y+1][random_location_X-1],
                ↪  (random_location_Y+1,random_location_X-1)))
172             NN_list.append((matrix[random_location_Y+1][random_location_X],
                ↪  (random_location_Y+1,random_location_X)))
173
174
175
176
177
178         if random_location_X == last_atom and random_location_Y !=
            ↪  first_row and random_location_Y != last_row and
            ↪  random_location_Y%2 == 0:
179             # this means we are on the very right but not in a corner
180             # this is for an odd row
181             # case 6
182
183             #top left works as normal
184             NN_list.append((matrix[random_location_Y-1][random_location_X],
                ↪  (random_location_Y-1,random_location_X)))
185
186             #top right wraps around to the first point in the upper row
187             NN_list.append((matrix[random_location_Y-1][first_atom],
                ↪  (random_location_Y-1,first_atom)))
188
189             #left nn works as normal
190             NN_list.append((matrix[random_location_Y][random_location_X-1],
                ↪  (random_location_Y,random_location_X-1)))
191
192             #right nn flips around to leftmost atom
```

```
193             NN_list.append((matrix[random_location_Y][first_atom],
                ↪  (random_location_Y,first_atom)))
194
195             # bottom left works as normal
196             NN_list.append((matrix[random_location_Y+1][random_location_X],
                ↪  (random_location_Y+1,random_location_X)))
197
198             # bottom right flips around to the leftmost atom
199             NN_list.append((matrix[random_location_Y+1][first_atom],
                ↪  (random_location_Y+1,first_atom)))
200
201
202
203
204
205         ##############
206         # boundary conditions for the four corners
207         ##############
208
209         if random_location_X == first_atom and random_location_Y ==
            ↪  first_row:
210
211             # this means we are on the top left corner
212
213             # case 7
214
215             # top left nn wraps to first atom of last row
216             NN_list.append((matrix[last_row][first_atom],
                ↪  (last_row,first_atom)))
217
218             # top right nn wraps to second atom in last row
219             NN_list.append((matrix[last_row][random_location_X+1],
                ↪  (last_row,random_location_X+1)))
220
221             # left nn wraps to last atom in same row
222             NN_list.append((matrix[random_location_Y][last_atom],
                ↪  (random_location_Y,last_atom)))
223
```

```
224             # these three stay normal
225             NN_list.append((matrix[random_location_Y][random_location_X+1],
                ↪  (random_location_Y,random_location_X+1)))
226             NN_list.append((matrix[random_location_Y+1][random_location_X],
                ↪  (random_location_Y+1,random_location_X)))
227
                ↪  NN_list.append((matrix[random_location_Y+1][random_location_X+1],
                ↪  (random_location_Y+1,random_location_X+1)))
228
229
230
231         if random_location_X == first_atom and random_location_Y ==
            ↪  last_row:
232             # this means we are in the bottom left corner
233
234             # case 8
235
236             # top left nn wraps to last atom of row above
237             NN_list.append((matrix[random_location_Y-1][last_atom],
                ↪  (random_location_Y-1,last_atom)))
238
239             # top right nn works as normal
240             NN_list.append((matrix[random_location_Y-1][first_atom],
                ↪  (random_location_Y-1,first_atom)))
241
242             # left goes to last atom of same row
243             NN_list.append((matrix[random_location_Y][last_atom],
                ↪  (random_location_Y,last_atom)))
244
245             # right goes works as normal
246             NN_list.append((matrix[random_location_Y][random_location_X+1],
                ↪  (random_location_Y,random_location_X+1)))
247
248             # bottom left goes to last atom of first row
249             NN_list.append((matrix[first_row][last_atom],
                ↪  (first_row,last_atom)))
250
251             # bottom right goes to top row first atom
```

```
252             NN_list.append((matrix[first_row][first_atom],
                ↪  (first_row,first_atom)))
253
254
255
256
257
258
259
260
261         if random_location_X == last_atom and random_location_Y ==
            ↪  first_row:
262             # this means we are on the top right corner
263             # case 9
264
265             # top left nn wraps to last atom of last row
266             NN_list.append((matrix[last_row][last_atom],
                ↪  (last_row,last_atom)))
267
268             # top right nn wraps to first atom of last row
269             NN_list.append((matrix[last_row][first_atom],
                ↪  (last_row,first_atom)))
270
271             # left nn works as normal
272             NN_list.append((matrix[random_location_Y][random_location_X-1],
                ↪  (random_location_Y,random_location_X-1)))
273
274             # right nn wraps to first atom of same row
275             NN_list.append((matrix[random_location_Y][first_atom],
                ↪  (random_location_Y,first_atom)))
276
277             # bottom left nn works as normal
278             NN_list.append((matrix[random_location_Y+1][random_location_X],
                ↪  (random_location_Y+1,random_location_X)))
279
280             # bottom right nn wraps to first atom of second row
281             NN_list.append((matrix[random_location_Y+1][first_atom],
                ↪  (random_location_Y+1,first_atom)))
```

```
282
283
284
285
286
287
288
289         if random_location_X == last_atom and random_location_Y ==
            ↪  last_row:
290             # this means we are in the bottom right corner
291             # case 10
292
293
294
295             # top left nn works as normal
296
                ↪  NN_list.append((matrix[random_location_Y-1][random_location_X-1],
                ↪  (random_location_Y-1,random_location_X-1)))
297
298
299             # top right nn works as normal
300             NN_list.append((matrix[random_location_Y-1][random_location_X],
                ↪  (random_location_Y-1,random_location_X)))
301
302
303             # left nn works as normal
304             NN_list.append((matrix[random_location_Y][random_location_X-1],
                ↪  (random_location_Y,random_location_X-1)))
305
306
307             # right nn warps around to first atom of same row
308             NN_list.append((matrix[random_location_Y][first_atom],
                ↪  (random_location_Y,first_atom)))
309
310             # bottom left nn wraps to second to lst atom of first row
311             NN_list.append((matrix[first_row][random_location_X-1],
                ↪  (first_row,random_location_X-1)))
312
```

```
313
314             # bottom right goes to last atom of first row
315             NN_list.append((matrix[first_row][last_atom],
                ↪  (first_row,last_atom)))
316
317
318
319
320         # non special cases handled here
321
322         if random_location_Y%2 == 0 and random_location_X != first_atom and
            ↪  random_location_X != last_atom and random_location_Y !=
            ↪  first_row and random_location_Y != last_row:
323             # general case a)
324             # even row (count starts at 0)
325
326             NN_list.append((matrix[random_location_Y-1][random_location_X],
                ↪  (random_location_Y-1,random_location_X)))
327
                ↪  NN_list.append((matrix[random_location_Y-1][random_location_X+1],
                ↪  (random_location_Y-1,random_location_X+1)))
328             NN_list.append((matrix[random_location_Y][random_location_X-1],
                ↪  (random_location_Y,random_location_X-1)))
329             NN_list.append((matrix[random_location_Y][random_location_X+1],
                ↪  (random_location_Y,random_location_X+1)))
330             NN_list.append((matrix[random_location_Y+1][random_location_X],
                ↪  (random_location_Y+1,random_location_X)))
331
                ↪  NN_list.append((matrix[random_location_Y+1][random_location_X+1],
                ↪  (random_location_Y+1,random_location_X+1)))
332
333
334         if random_location_Y%2 != 0 and random_location_X != first_atom and
            ↪  random_location_X != last_atom and random_location_Y !=
            ↪  first_row and random_location_Y != last_row:
335             # general case b)
336
```

```
337
                ↪  NN_list.append((matrix[random_location_Y-1][random_location_X-1],
                ↪  (random_location_Y-1,random_location_X-1)))
338             NN_list.append((matrix[random_location_Y-1][random_location_X],
                ↪  (random_location_Y-1,random_location_X)))
339             NN_list.append((matrix[random_location_Y][random_location_X-1],
                ↪  (random_location_Y,random_location_X-1)))
340             NN_list.append((matrix[random_location_Y][random_location_X+1],
                ↪  (random_location_Y,random_location_X+1)))
341
                ↪  NN_list.append((matrix[random_location_Y+1][random_location_X-1],
                ↪  (random_location_Y+1,random_location_X-1)))
342             NN_list.append((matrix[random_location_Y+1][random_location_X],
                ↪  (random_location_Y+1,random_location_X)))
343
344
345
346         list_NN_list.append(NN_list)
347
348     return(list_NN_list)
349
350
351
352 def create_evolution(matrix):
353
354
355     # use list comprehension should be fast
356     global zero_in_matrix
357     zero_in_matrix = [(i,j) for i, row in enumerate(matrix) for j, column
        ↪  in enumerate(row) if column ==0]
358
359     # call helper function to find NN for all vacancies
360
361     list_NN_list = create_nn(zero_in_matrix, matrix)
362
363
364
365
```

```
366     ################### remove all elements where the vacancy checksum is <
        ↪  3 meaning no movement when 3 NNs are also vacancies
367     global list_NN_list_filtered
368     list_NN_list_filtered = []
369     global zero_im_matrix_filtered
370     zero_in_matrix_filtered = []
371
372
373
374     for NN_list, vacancy_position in zip(list_NN_list, zero_in_matrix):
375         vacancy_counter = 0
376         for element in NN_list:
377             if element[0] == 0:
378                 vacancy_counter = vacancy_counter + 1
379         if vacancy_counter < 3:
380             list_NN_list_filtered.append(NN_list)
381             zero_in_matrix_filtered.append(vacancy_position)
382
383
384     ################### pick the NN by weighted chance
385     global chances_list
386     chances_list = []
387     for NN_list in list_NN_list_filtered:
388
389         chance_calculator = 0
390         divisor = 0
391
392         for element in NN_list:
393
394             if element[0] == 1:
395                 chance_calculator = chance_calculator + 1/97849
396                 divisor = divisor + 1
397             if element[0] == 2:
398                 chance_calculator = chance_calculator + 1
399                 divisor = divisor + 1
400
401         chances_list.append(chance_calculator/divisor)
402
```

```
403
404
405         global choice_index
406         choice_index = random.choices(range(len(list_NN_list_filtered)),
            ↪  chances_list,k = 1)[0]
407
408         NN_list_choice = list_NN_list_filtered[choice_index]
409         random_location_Y = zero_in_matrix_filtered[choice_index][0]
410         random_location_X = zero_in_matrix_filtered[choice_index][1]
411
412
413
414
415
416
417
418         matrix = movement_evolution(NN_list_choice, matrix, random_location_X,
            ↪  random_location_Y)
419
420         return(matrix)
421
422
423
424 def movement_evolution(NN_list, matrix, random_location_X,
    ↪  random_location_Y):
425
426
            ↪  ##########################################################################
427         # Hilfsfunktion um die Bewegung zu definieren
428
            ↪  ##########################################################################
429         ### zähle die Anzahl der vorhandenen Atome und Leerstellen in der
            ↪  Umgebung und speichere die Positionen
430
431         counter0 = 0
432         counter1 = 0
433         counter2 = 0
434
```

```
435     NullList = []
436     EinsList = []
437     ZweiList = []
438 
439     #print('NN item:' + str(NN_list[2][0]))
440     #print('NN item:' + str(NN_list[2]))
441 
442 
443     for i in range(len(NN_list)):
444         if NN_list[i][0] == 0:
445             counter0 += 1
446             NullList.append(NN_list[i])
447 
448         if NN_list[i][0] == 1:
449             counter1 += 1
450             EinsList.append(NN_list[i])
451 
452         if NN_list[i][0] == 2:
453             counter2 += 1
454             ZweiList.append(NN_list[i])
455 
456 
    ↪  ##########################################################################
457     # Hüpfe die Leerstelle
458 
459 
460 
461 
462     # determine the type of area the vacancy is in by weighing the nearest
    ↪  neighbours
463     # mobility in pure MoS2 area (1) is 1/97849
464     # mobility in pure TaS2 area (2) is 1
465     # distribute mobility according to weighted nearest NN average and
    ↪  exclude other vacancies
466 
467 
468 
469 
```

```
470
471
472     switch_options = ["NullList", "EinsList", "ZweiList"]
473     weights = [counter0/6, counter1/6, counter2/6]
474
475     choice = random.choices(switch_options, weights,k = 1)[0]
476
477     if choice == "NullList":
478     # a switch with a zero is the same as no change
479         return(matrix)
480
481
482
483     if choice == "EinsList":
484         randomIndex = np.random.randint(0, len(EinsList))
485
486         matrix[EinsList[randomIndex][1][0]][EinsList[randomIndex][1][1]] =
            ↪  0
487         matrix[random_location_Y][random_location_X] = 1
488
489         return(matrix)
490
491     if choice == "ZweiList":
492
493         randomIndex = np.random.randint(0, len(ZweiList))
494
495         matrix[ZweiList[randomIndex][1][0]][ZweiList[randomIndex][1][1]] =
            ↪  0
496         matrix[random_location_Y][random_location_X] = 2
497
498         return(matrix)
499
500
501
502 def fill_hexagonal(hexagonal_surface):
503     # this function fills the surface with a hexagonal combination of the
      ↪  two materials and a distribution of holes
504
```

```
505     ##fill with first material as 1
506
507     for i in range(len(hexagonal_surface)):
508         #print(hexagonal_surface[i])
509         for j in range(0, len(hexagonal_surface[i])-0):
510             hexagonal_surface[i][j] = 2
511
512
513
514
515     # define hexgagon
516     # aufsteigend
517     hexagonal_surface[15][20:31] = 1
518     hexagonal_surface[16][19:31] = 1
519     hexagonal_surface[17][19:32] = 1
520     hexagonal_surface[18][18:32] = 1
521     hexagonal_surface[19][18:33] = 1
522     hexagonal_surface[20][17:33] = 1
523     hexagonal_surface[21][17:34] = 1
524     hexagonal_surface[22][16:34] = 1
525     hexagonal_surface[23][16:35] = 1
526     hexagonal_surface[24][15:35] = 1
527     hexagonal_surface[25][15:36] = 1
528
529     #absteigend
530
531     hexagonal_surface[26][15:35] = 1
532     hexagonal_surface[27][16:35] = 1
533     hexagonal_surface[28][16:34] = 1
534     hexagonal_surface[29][17:34] = 1
535     hexagonal_surface[30][17:33] = 1
536     hexagonal_surface[31][18:33] = 1
537     hexagonal_surface[32][18:32] = 1
538     hexagonal_surface[33][19:32] = 1
539     hexagonal_surface[34][19:31] = 1
540     hexagonal_surface[35][20:31] = 1
541
542
```

```
543     # add zeroes
544
545     hexagonal_surface[14][19:31] = 0
546     hexagonal_surface[36][20:31] = 0
547
548     hexagonal_surface[15][19] = 0
549     #hexagonal_surface[16][18] = 0
550     hexagonal_surface[17][18] = 0
551     #hexagonal_surface[18][17] = 0
552     hexagonal_surface[19][17] = 0
553     #hexagonal_surface[20][16] = 0
554     hexagonal_surface[21][16] = 0
555     #hexagonal_surface[22][15] = 0
556     hexagonal_surface[23][15] = 0
557     #hexagonal_surface[24][14] = 0
558     hexagonal_surface[25][14] = 0
559     #hexagonal_surface[15][31] = 0
560     hexagonal_surface[16][31] = 0
561     #hexagonal_surface[17][32] = 0
562     hexagonal_surface[18][32] = 0
563     #hexagonal_surface[19][33] = 0
564     hexagonal_surface[20][33] = 0
565     #hexagonal_surface[21][34] = 0
566     hexagonal_surface[22][34] = 0
567     #hexagonal_surface[23][35] = 0
568     hexagonal_surface[24][35] = 0
569     #hexagonal_surface[25][36] = 0
570
571
572
573
574
575     hexagonal_surface[26][14] = 0
576     #hexagonal_surface[27][15] = 0
577     hexagonal_surface[28][15] = 0
578     #hexagonal_surface[29][16] = 0
579     hexagonal_surface[30][16] = 0
580     #hexagonal_surface[31][17] = 0
```

```
581     hexagonal_surface[32][17] = 0
582     #hexagonal_surface[33][18] = 0
583     hexagonal_surface[34][18] = 0
584     #hexagonal_surface[35][19] = 0
585     hexagonal_surface[36][19] = 0
586 
587     #hexagonal_surface[26][35] = 0
588     hexagonal_surface[27][35] = 0
589     #hexagonal_surface[28][34] = 0
590     hexagonal_surface[29][34] = 0
591     #hexagonal_surface[30][33] = 0
592     hexagonal_surface[31][33] = 0
593     #hexagonal_surface[32][32] = 0
594     hexagonal_surface[33][32] = 0
595     #hexagonal_surface[34][31] = 0
596     hexagonal_surface[35][31] = 0
597 
598     return(hexagonal_surface)
599 
600 
601 
602 def create_plot(hexagonal_surface, name):
603 
604     ############################################ create hexagonal surface
        ↪  for the plot
605 
606 
607     a = 1
608 
609     XCoordinates = []
610     YCoordinates = []
611     ZCoordinates = []
612 
613     for i in range(len(hexagonal_surface)):
614         for j in range(len(hexagonal_surface[i])):
615 
616 
617             # either even or uneven row
```

```
618             # for each row define the starting point and go to the right
619             if i%2 == 0:
620                 XCoordinates.append(0+j*a)
621                 YCoordinates.append(0-i*(math.sqrt(3)/2)*a)
622                 ZCoordinates.append(hexagonal_surface[i][j])
623             elif i%2 != 0:
624                 XCoordinates.append(-a/2+j*a)
625                 YCoordinates.append(0-i*(math.sqrt(3)/2)*a)
626                 ZCoordinates.append(hexagonal_surface[i][j])
627             else:
628                 print('Something went terribly wrong')
629                 sys.exit(0)
630
631
632
    ↪  ##########################################################################
633
634     # define new lists for use in plot in one plain
635
636     X_Mo = []
637     Y_Mo = []
638     Z_Mo = []
639
640     X_Ta = []
641     Y_Ta = []
642     Z_Ta = []
643
644     X_vacancy = []
645     Y_vacancy = []
646     Z_vacancy = []
647
648     for i in range(len(ZCoordinates)):
649         # sort the data by z-height into type-specific lists
650         if ZCoordinates[i] == 0:
651             X_vacancy.append(XCoordinates[i])
652             Y_vacancy.append(YCoordinates[i])
653             Z_vacancy.append(ZCoordinates[i])
654
```

```
655         elif ZCoordinates[i] == 1:
656             X_Mo.append(XCoordinates[i])
657             Y_Mo.append(YCoordinates[i])
658             Z_Mo.append(ZCoordinates[i])
659 
660         elif ZCoordinates[i] == 2:
661             X_Ta.append(XCoordinates[i])
662             Y_Ta.append(YCoordinates[i])
663             Z_Ta.append(ZCoordinates[i])
664 
665         else:
666             print('Unexpected Z-height')
667             sys.exit(0)
668 
669 
670 
671     # create meshgrid an interpolation
672     x, y = np.meshgrid(np.linspace(min(XCoordinates), max(XCoordinates),
    ↪  200), np.linspace(min(YCoordinates), max(YCoordinates), 200))
673     # adjust between nearest, linear and cubic as desired
674     z = griddata((XCoordinates,YCoordinates), ZCoordinates, (x,y),
    ↪  method='linear')
675 
676 
677 
678 
    ↪  ##########################################################################
679     # 3D plots
680 
    ↪  ##########################################################################
681 
682 
683     fig = go.Figure()
684     fig.add_trace((go.Scatter3d(x = X_Mo, y = Y_Mo, z = Z_Mo,
    ↪  mode='markers', marker = dict(size=5, color='red', opacity=1))))
685     fig.add_trace((go.Scatter3d(x = X_Ta, y = Y_Ta, z = Z_Ta,
    ↪  mode='markers', marker = dict(size=5, color='blue', opacity=1))))
```

```
686     fig.add_trace((go.Scatter3d(x = X_vacancy, y=Y_vacancy, z = Z_vacancy,
        ↪  mode='markers', marker = dict(size=5, color='white', opacity=1))))
687     fig.update_layout(scene=dict(
688         xaxis=dict(backgroundcolor = 'gray', title = dict(text =
            ↪  'X-Coordinate [#]', font = dict(size = 20)), tickfont =
            ↪  dict(size = 14), range = [-35,70]),
689         yaxis=dict(backgroundcolor = 'gray', title = dict(text =
            ↪  'Y-Coordinate [#]', font = dict(size = 20)), tickfont =
            ↪  dict(size = 14), range = [-80,40]),
690         zaxis=dict(backgroundcolor = 'gray', title = dict(text = 'Z-height
            ↪  of material [a.u.]', font = dict(size = 20)), tickfont =
            ↪  dict(size = 14), range = [-1,15]),
691         aspectmode="manual",
692         aspectratio =dict(x=1,y=120/105,z=0.5)
693         ))
694
695
696
697     fig.write_html(file = name + '_HexagonalSurface_out_of_plane.html',
        ↪  auto_open = False)
698
699
700
701     fig = go.Figure()
702     fig.add_trace((go.Scatter3d(x = X_Mo, y = Y_Mo, z =
        ↪  np.zeros(len(X_Mo)), mode='markers', marker = dict(size=5,
        ↪  color='red', opacity=1))))
703     fig.add_trace((go.Scatter3d(x = X_Ta, y = Y_Ta, z =
        ↪  np.zeros(len(X_Ta)), mode='markers', marker = dict(size=5,
        ↪  color='blue', opacity=1))))
704     fig.add_trace((go.Scatter3d(x = X_vacancy, y=Y_vacancy, z =
        ↪  np.zeros(len(X_vacancy)), mode='markers', marker = dict(size=5,
        ↪  color='white', opacity=1))))
705     fig.update_layout(scene=dict(
706         xaxis=dict(backgroundcolor = 'gray', title = dict(text =
            ↪  'X-Coordinate [#]', font = dict(size = 20)), tickfont =
            ↪  dict(size = 14), range = [-35,70]),
```

```
707         yaxis=dict(backgroundcolor = 'gray', title = dict(text =
            ↪  'Y-Coordinate [#]', font = dict(size = 20)), tickfont =
            ↪  dict(size = 14), range = [-80,40]),
708         zaxis=dict(backgroundcolor = 'gray', title = dict(text = 'Z-height
            ↪  of material [a.u.]', font = dict(size = 20)), tickfont =
            ↪  dict(size = 14), range = [-1,15]),
709         aspectmode="manual",
710         aspectratio =dict(x=1,y=120/105,z=0.5),
711
712         ),
713
714         )
715
716
717
718     fig.write_html(file = name + '_HexagonalSurface_in_plane.html',
        ↪  auto_open = False)
719
720
721
722     fig = go.Figure()
723     fig.add_trace(go.Surface(x=x, y=y, z=z))
724     fig.update_layout(scene=dict(
725         xaxis=dict(backgroundcolor = 'gray', title = dict(text =
            ↪  'X-Coordinate [#]', font = dict(size = 20)), tickfont =
            ↪  dict(size = 14), range=[-35,70]),
726         yaxis=dict(backgroundcolor = 'gray', title = dict(text =
            ↪  'Y-Coordinate [#]', font = dict(size = 20)), tickfont =
            ↪  dict(size = 14),range=[-80,40]),
727         zaxis=dict(backgroundcolor = 'gray', title = dict(text = 'Z-height
            ↪  of material [a.u.]', font = dict(size = 20)), tickfont =
            ↪  dict(size = 14),range=[-1,15]),
728         aspectmode="manual",
729         aspectratio =dict(x=1,y=120/105,z=0.5)
730         ))
731
732
733
```

```
734     fig.write_html(file = name + 'HexagonalSurfaceInterpolated.html',
        ↪  auto_open = False)
735
736
737
738 def create_matplotlib_plot(hexagonal_surface, name):
739
740     a = 1
741
742     XCoordinates = []
743     YCoordinates = []
744     ZCoordinates = []
745
746     for i in range(len(hexagonal_surface)):
747         for j in range(len(hexagonal_surface[i])):
748
749
750             # either even or uneven row
751             # for each row define the starting point and go to the right
752             if i%2 == 0:
753                 XCoordinates.append(0+j*a)
754                 YCoordinates.append(0-i*(math.sqrt(3)/2)*a)
755                 ZCoordinates.append(hexagonal_surface[i][j])
756             elif i%2 != 0:
757                 XCoordinates.append(-a/2+j*a)
758                 YCoordinates.append(0-i*(math.sqrt(3)/2)*a)
759                 ZCoordinates.append(hexagonal_surface[i][j])
760             else:
761                 print('Something went terribly wrong')
762                 sys.exit(0)
763
764     XCoordinates = np.array(XCoordinates)
765     YCoordinates = np.array(YCoordinates)
766     ZCoordinates = np.array(ZCoordinates)
767
768
769
        ↪  ##########################################################################
```

```
770
771     # define new lists for use in plot in one plain
772
773     X_Mo = []
774     Y_Mo = []
775     Z_Mo = []
776
777     X_Ta = []
778     Y_Ta = []
779     Z_Ta = []
780
781     X_vacancy = []
782     Y_vacancy = []
783     Z_vacancy = []
784
785     for i in range(len(ZCoordinates)):
786         # sort the data by z-height into type-specific lists
787         if ZCoordinates[i] == 0:
788             X_vacancy.append(XCoordinates[i])
789             Y_vacancy.append(YCoordinates[i])
790             Z_vacancy.append(ZCoordinates[i])
791
792         elif ZCoordinates[i] == 1:
793             X_Mo.append(XCoordinates[i])
794             Y_Mo.append(YCoordinates[i])
795             Z_Mo.append(ZCoordinates[i])
796
797         elif ZCoordinates[i] == 2:
798             X_Ta.append(XCoordinates[i])
799             Y_Ta.append(YCoordinates[i])
800             Z_Ta.append(ZCoordinates[i])
801
802         else:
803             print('Unexpected Z-height')
804             sys.exit(0)
805
806
807
```

```
808
809
810     fig = plt.figure(figsize = (10,7), dpi = 300, constrained_layout =
        ↪  True)
811     gs = gridspec.GridSpec(1,2, width_ratios = [1,1], wspace = 0.1, figure
        ↪  = fig)
812     ax = fig.add_subplot(gs[0], projection = '3d')
813     ax.scatter3D(X_Mo, Y_Mo, Z_Mo, color = 'red')
814     ax.scatter3D(X_Ta, Y_Ta, Z_Ta, color = 'blue')
815     ax.scatter3D(X_vacancy, Y_vacancy, Z_vacancy, color = 'white')
816     ax.xaxis.set_pane_color("gray")
817     ax.yaxis.set_pane_color("gray")
818     ax.zaxis.set_pane_color("gray")
819     ax.view_init(elev = 20, azim = -45)
820     ax.set_xlabel('X-Coordinate [#]')
821     ax.set_ylabel('Y-Coordinate [#]')
822     ax.set_zlabel('Z-height of material [a.u.]')
823
824     ax2 = fig.add_subplot(gs[1])
825     ax2.scatter(X_Mo, Y_Mo, color = 'red', label = 'Mo-atoms', s = 10)
826     ax2.scatter(X_Ta, Y_Ta, color = 'blue', label = 'Ta-atoms', s = 10)
827     ax2.scatter(X_vacancy, Y_vacancy, color = 'white', label = 'vacancies',
        ↪  s = 10)
828     ax2.set_facecolor("gray")
829     ax2.grid(True)
830     ax2.set_aspect('equal')
831     ax2.set_xlabel('X-Coordinate [#]')
832     ax2.set_ylabel('Y-Coordinate [#]')
833
834
835     # place the legend
836     plt.legend(loc = 'upper right', bbox_to_anchor = (1.4,1), facecolor =
        ↪  'gray')
837     fig.canvas.draw()
838     fig.savefig(name + ".png")
839     plt.show()
840
841
```

```
842
843
844 ##############################################################################
845 # Call of functions
846 ##############################################################################
847
848 # ACHTUNG needs to be an even matrix in y length. X length does not matter
    ↪  (except 0 and maybe 1)
849 # check if optimized for EVEN
850 hexagonal_surface = create_hexagonal(50,50)
851 hexagonal_surface = fill_hexagonal(hexagonal_surface)
852
853 # create plot of the surface in starting position
854 create_plot(hexagonal_surface, str(0))
855 create_matplotlib_plot(hexagonal_surface, str(0))
856
857 # create evolutions of the surface
858 for i in range(1,200001):
859     try:
860         # this will fail if there is no more movement
861         hexagonal_surface = create_evolution(hexagonal_surface)
862
863         if i%10000 == 0:
864             # create a snapshot every now and then (define moment in
                ↪  if-statement)
865             create_plot(hexagonal_surface, str(i))
866             create_matplotlib_plot(hexagonal_surface, str(i))
867
868     except Exception as e:
869         if isinstance(e, IndexError):
870             # make an image after no more movement
871             create_plot(hexagonal_surface, str(i) + '_final')
872             create_matplotlib_plot(hexagonal_surface, str(i) + '_final')
873             print('No more movement')
874             sys.exit(0)
875         else:
876             # if other error output
877             print(e)
```

```
878             traceback.print_exc()
879             sys.exit(0)
880         continue
881
```

BIBLIOGRAPHY

[1] Kostya S Novoselov et al. “Electric field effect in atomically thin carbon films”. In: *science* 306.5696 (2004), pp. 666–669.

[2] Ruben Mas-Balleste et al. “2D materials: to graphene and beyond”. In: *Nanoscale* 3.1 (2011), pp. 20–30.

[3] Sajedeh Manzeli et al. “2D transition metal dichalcogenides”. In: *Nature Reviews Materials* 2.8 (2017), pp. 1–15.

[4] V Sorkin et al. “Nanoscale transition metal dichalcogenides: structures, properties, and applications”. In: *Critical reviews in solid state and materials sciences* 39.5 (2014), pp. 319–367.

[5] Agnieszka Kuc, Thomas Heine, and Andras Kis. “Electronic properties of transition-metal dichalcogenides”. In: *MRS bulletin* 40.7 (2015), pp. 577–584.

[6] Xinglin Wen, Zibo Gong, and Dehui Li. “Nonlinear optics of two-dimensional transition metal dichalcogenides”. In: *InfoMat* 1.3 (2019), pp. 317–337.

[7] Shu-Wen Zheng et al. “Observation of quantum-confined exciton states in monolayer WS_2 quantum dots by ultrafast spectroscopy”. In: *Nanoscale* 13.40 (2021), pp. 17093–17100.

[8] Chris A Mack. “Fifty years of Moore’s law”. In: *IEEE Transactions on semiconductor manufacturing* 24.2 (2011), pp. 202–207.

[9] Kuan-Chang Chiu et al. “Synthesis and application of monolayer semiconductors (June 2015)”. In: *IEEE Journal of Quantum Electronics* 51.10 (2015), pp. 1–10.

[10] Bin Amin, Nirpendra Singh, and Udo Schwingenschlögl. “Heterostructures of transition metal dichalcogenides”. In: *Physical review B* 92.7 (2015), p. 075439.

[11] JP Wilcoxon and GA Samara. "Strong quantum-size effects in a layered semiconductor: MoS_2 nanoclusters". In: *Physical Review B* 51.11 (1995), p. 7299.

[12] Chun-Yan Luan et al. "Elucidation of luminescent mechanisms of size-controllable $MoSe_2$ quantum dots". In: *Applied Physics Letters* 111.7 (2017).

[13] Liangxu Lin et al. "Fabrication of luminescent monolayered tungsten dichalcogenides quantum dots with giant spin-valley coupling". In: *ACS nano* 7.9 (2013), pp. 8214–8223.

[14] Albert Bruix et al. "Single-layer MoS_2 on Au (111): Band gap renormalization and substrate interaction". In: *Physical Review B* 93.16 (2016), p. 165422.

[15] Qichao Tian et al. "Electronic structures and Mott state of epitaxial TaS_2 monolayers". In: *Science China Physics, Mechanics & Astronomy* 67.5 (2024), p. 256811.

[16] Bilu Liu et al. "Chemical vapor deposition growth of monolayer WSe_2 with tunable device characteristics and growth mechanism study". In: *ACS nano* 9.6 (2015), pp. 6119–6127.

[17] Signe S Grønborg et al. "Synthesis of epitaxial single-layer MoS_2 on Au(111)". In: *Langmuir* 31.35 (2015), pp. 9700–9706.

[18] Ana Senkić et al. "Effects of CVD growth parameters on global and local optical properties of MoS_2 monolayers". In: *Materials chemistry and physics* 296 (2023), p. 127185.

[19] Zahra Hemmat et al. "Quasi-Binary Transition Metal Dichalcogenide Alloys: Thermodynamic Stability Prediction, Scalable Synthesis, and Application". In: *Advanced Materials* 32.26 (2020), p. 1907041.

[20] Appu Kumar Singh et al. "Review of strategies toward the development of alloy two-dimensional (2D) transition metal dichalcogenides". In: *Iscience* 24.12 (2021).

[21] Didhiti Bhattacharya et al. "TMDC ternary alloy–based triboelectric nanogenerators with giant photo-induced enhancement". In: *Nanoscale* 15.43 (2023), pp. 17398–17408.

[22] Shubhrasish Mukherjee et al. "High-Performance Broad-Band Photodetection Based on Graphene–$MoS_{2x}Se_{2(1-x)}$ Alloy Engineered Phototransistors". In: *ACS applied materials & interfaces* 14.30 (2022), pp. 34875–34883.

[23] Gerd Binnig et al. “Surface studies by scanning tunneling microscopy”. In: *Physical review letters* 49.1 (1982), p. 57.

[24] Nobel Prize Outreach AB 2024. *All Nobel Prizes*. URL: `https://www.nobelprize.org/prizes/lists/all-nobel-prizes/` (visited on 11/10/2024).

[25] PA Christensen. “Electrochemical aspects of STM and related techniques”. In: *Chemical Society Reviews* 21.3 (1992), pp. 197–208.

[26] Kai Mehlich. “In-plane heterostructures in transition metal dichalcogenide monolayers”. Master’s thesis. Universität Münster, 2019.

[27] Edward L Wolf. *Principles of electron tunneling spectroscopy*. Vol. 152. Oxford University Press, 2012, p. 2.

[28] Gernot Münster. “Quantentheorie”. In: 2nd. Walter de Gruyter GmbH & Co KG, 2020, p. 10.

[29] Gernot Münster. “Quantentheorie”. In: 2nd. Walter de Gruyter GmbH & Co KG, 2020, p. 32.

[30] C.J. Chen. “Introduction to Scanning Tunneling Microscopy”. In: 2nd. Oxford University Press, 2008, pp. 52–54.

[31] C.J. Chen. “Introduction to Scanning Tunneling Microscopy”. In: 2nd. Oxford University Press, 2008, pp. 54–56.

[32] Günter Gottstein. “Materialwissenschaft und Werkstofftechnik: Physikalische Grundlagen”. In: 4. Auflage. Springer Vieweg, 2014, pp. 37–41.

[33] William Hallowes Miller. *A treatise on crystallography*. Printed at the Pitt Press, for J. & JJ Deighton, 1839.

[34] Royal Society of Chemnistry. *Periodic Table*. `https://periodic-table.rsc.org/element/79/gold`. Accessed:13.08.2025. 2025.

[35] The Engineering ToolBox (2005). *Thermal Conductivity of Metals and Alloys: Data Table Reference Guide*. `https://www.engineeringtoolbox.com/thermal-conductivity-metals-d_858.html`. Accessed:13.08.2025. 2025.

[36] Raymond A Serway and John W Jewett. *Principles of physics*. Vol. 2. Saunders College Pub. Fort Worth, TX, 1998.

[37] Hongxia Zhong et al. “Interfacial properties of monolayer and bilayer MoS_2 contacts with metals: beyond the energy band calculations”. In: *Scientific reports* 6.1 (2016), p. 21786.

[38] Mojtaba Farmanbar and Geert Brocks. “First-principles study of van der Waals interactions and lattice mismatch at MoS_2/metal interfaces”. In: *Physical Review B* 93.8 (2016), p. 085304.

[39] Luka Pirker et al. “When 2D materials meet metals”. In: *2D Materials* 11.2 (2024), p. 022003.

[40] Caio C Silva et al. “Structure of monolayer 2H-TaS_2 on Au (111)”. In: *Physical Review B* 104.20 (2021), p. 205414.

[41] M.Y. Gokhale and R.V. Mantri. “Chapter 4 - API Solid-Form Screening and Selection”. In: *Developing Solid Oral Dosage Forms (Second Edition)*. Ed. by Yihong Qiu et al. Second Edition. Boston: Academic Press, 2017, pp. 85–112. DOI: https://doi.org/10.1016/B978-0-12-802447-8.00004-2. URL: https://www.sciencedirect.com/science/article/pii/B9780128024478000042.

[42] Alfa Chemistry. *Single Crystals*. https://www.alfa-chemistry.com/products/single-crystals-121.htm. Accessed:14.08.2025. 2025.

[43] D Phil Woodruff. “Modern techniques of surface science”. In: 3rd. Cambridge university press, 2016, p. 28.

[44] M El-Batanouny et al. “Double-sine-Gordon solitons: A model for misfit dislocations on the Au (111) reconstructed surface”. In: *Physical review letters* 58.26 (1987), p. 2762.

[45] Claudia E Bach et al. “Stress relief in reconstruction”. In: *Physical review letters* 78.22 (1997), p. 4225.

[46] Andrew Zangwill. “Physics at surfaces”. In: Cambridge university press, 1988, pp. 111–113.

[47] Norman Charles Bartelt and Konrad Thürmer. “Structure and energetics of the elbows in the Au (111) herringbone reconstruction”. In: *Physical Review B* 104.16 (2021), p. 165425.

[48] JA Meyer et al. “Preferential island nucleation at the elbows of the Au (111) herringbone reconstruction through place exchange”. In: *Surface science* 365.1 (1996), pp. L647–L651.

[49] DD Chambliss, RJ Wilson, and S Chiang. "Nucleation of ordered Ni island arrays on Au (111) by surface-lattice dislocations". In: *Physical review letters* 66.13 (1991), p. 1721.

[50] Bert Voigtländer, Gerhard Meyer, and Nabil M Amer. "Epitaxial growth of thin magnetic cobalt films on Au (111) studied by scanning tunneling microscopy". In: *Physical Review B* 44.18 (1991), p. 10354.

[51] Ch Wöll et al. "Determination of atom positions at stacking-fault dislocations on Au (111) by scanning tunneling microscopy". In: *Physical Review B* 39.11 (1989), p. 7988.

[52] Johannes V Barth et al. "Scanning tunneling microscopy observations on the reconstructed Au (111) surface: Atomic structure, long-range superstructure, rotational domains, and surface defects". In: *Physical Review B* 42.15 (1990), p. 9307.

[53] V Repain et al. "Reconstruction, step edges and self-organization on the Au (111) surface". In: *Applied surface science* 162 (2000), pp. 30–36.

[54] Quanmin Guo, Feng Yin, and Richard E Palmer. "Beyond the herringbone reconstruction: magic gold fingers". In: *Small* 1.1 (2005), pp. 76–79.

[55] John E Ayers et al. "Heteroepitaxy of semiconductors: theory, growth, and characterization". In: 2nd. CRC press, 2016, pp. 181–184.

[56] John E Ayers et al. "Heteroepitaxy of semiconductors: theory, growth, and characterization". In: CRC press, 2016, p. 182.

[57] Alexander V Kolobov and Junji Tominaga. "Two-dimensional transition-metal dichalcogenides". In: vol. 239. Springer, 2016, p. 15.

[58] Alexander V Kolobov and Junji Tominaga. "Two-dimensional transition-metal dichalcogenides". In: vol. 239. Springer, 2016, pp. 29–33.

[59] Luojun Du et al. "Engineering symmetry breaking in 2D layered materials". In: *Nature Reviews Physics* 3.3 (2021), pp. 193–206.

[60] Narayanasamy Sabari Arul and Vellalapalayam Devaraj Nithya. "Two Dimensional Transition Metal Dichalcogenides". In: Springer, 2019, pp. 21–22.

[61] Narayanasamy Sabari Arul and Vellalapalayam Devaraj Nithya. "Two Dimensional Transition Metal Dichalcogenides". In: Springer, 2019, p. 3.

[62] Péter Vancsó et al. “The intrinsic defect structure of exfoliated MoS_2 single layers revealed by Scanning Tunneling Microscopy”. In: *Scientific reports* 6.1 (2016), p. 29726.

[63] Alexander V Kolobov and Junji Tominaga. “Two-dimensional transition-metal dichalcogenides”. In: vol. 239. Springer, 2016, pp. 109–119.

[64] Caio C Silva et al. “Spatial variation of geometry, binding, and electronic properties in the moiré superstructure of MoS_2 on Au (111)”. In: *2D Materials* 9.2 (2022), p. 025003.

[65] Daniela Dombrowski et al. “Phase engineering in tantalum sulfide monolayers on Au (111)”. In: *2D Materials* 10.2 (2023), p. 025005.

[66] Fang Cheng et al. “Epitaxial Growth of Single-Layer Niobium Selenides with Controlled Stoichiometric Phases”. In: *Advanced Materials Interfaces* 5.15 (2018), p. 1800429.

[67] Zhihong Zhang et al. “Epitaxy of 2D materials toward single crystals”. In: *Advanced Science* 9.8 (2022), p. 2105201.

[68] Kai Mehlich et al. “Dislocation-free two-dimensional concentric lateral heterostructures: MoS_2–TaS_2/Au(111)”. In: *2D Materials* 11.3 (2024), p. 035035.

[69] Rui Dong and Irma Kuljanishvili. “Progress in fabrication of transition metal dichalcogenides heterostructure systems”. In: *Journal of Vacuum Science & Technology B* 35.3 (2017).

[70] Yu Kobayashi et al. “Continuous heteroepitaxy of two-dimensional heterostructures based on layered chalcogenides”. In: *ACS nano* 13.7 (2019), pp. 7527–7535.

[71] Danliang Zhang et al. “Near-unity polarization of valley-dependent second-harmonic generation in stacked TMDC layers and heterostructures at room temperature”. In: *Advanced Materials* 32.29 (2020), p. 1908061.

[72] Weijun Ren et al. “Impact of moiré superlattice on atomic stress and thermal transport in van der Waals heterostructures”. In: *Applied Physics Reviews* 10.4 (2023).

[73] Stephen Carr, Shiang Fang, and Efthimios Kaxiras. “Electronic-structure methods for twisted moiré layers”. In: *Nature Reviews Materials* 5.10 (2020), pp. 748–763.

[74] Isaac Amidror. "The Theory of the Moiré Phenomenon: Volume I: Periodic Layers". In: vol. 38. Springer Science & Business Media, 2009, pp. 9–17.

[75] Isaac Amidror. "The Theory of the Moiré Phenomenon: Volume I: Periodic Layers". In: vol. 38. Springer Science & Business Media, 2009, p. 14.

[76] Ronald Newbold Bracewell and Ronald N Bracewell. *The Fourier transform and its applications*. Vol. 31999. McGraw-hill New York, 1986.

[77] Isaac Amidror. "The Theory of the Moiré Phenomenon: Volume I: Periodic Layers". In: vol. 38. Springer Science & Business Media, 2009, p. 469.

[78] Isaac Amidror. "The Theory of the Moiré Phenomenon: Volume I: Periodic Layers". In: vol. 38. Springer Science & Business Media, 2009, p. 474.

[79] Isaac Amidror. "The Theory of the Moiré Phenomenon: Volume I: Periodic Layers". In: vol. 38. Springer Science & Business Media, 2009, p. 409.

[80] Wikipedia authors. URL: `https://en.wikipedia.org/wiki/Ernest_Kirkendall` (visited on 11/12/2024).

[81] Michigan Engineering; Gabe Cherry. *Kicking the hornet's nest: the Kirkendall Effect*. Accessed: 2025-11-09. 2017-06-16. URL: `https://news.engin.umich.edu/2017/06/kicking-the-hornets-nest-the-kirkendall-effect/`.

[82] Hideo Nakajima. "The discovery and acceptance of the Kirkendall Effect: The result of a short research career". In: *JoM* 49 (1997), pp. 15–19.

[83] EO Kirkendall and AD Smigelskas. "Zinc diffusion in alpha brass". In: *Aime Trans* 171 (1947), pp. 130–142.

[84] Günter Gottstein. "Materialwissenschaft und Werkstofftechnik: Physikalische Grundlagen". In: 4. Auflage. Springer Vieweg, 2014, p. 163.

[85] Lawrence S Darken. "Diffusion, mobility and their interrelation through free energy in binary metallic systems". In: *Trans. Aime* 175 (1948), pp. 184–201.

[86] RW Balluffi and LL Seigle. "Growth of voids in metals during diffusion and creep". In: *Acta metallurgica* 5.8 (1957), pp. 449–454.

[87] JA Brinkmanf. "Mechanism of pore formation associated with the Kirkendall effect". In: *Acta metallurgica* 3.2 (1955), pp. 140–145.

[88] Daniela Dombrowski. "Epitaxial 2D Materials: Analysis, Utilization and Elimination of Layer-Substrate Interaction". PhD thesis. Universität Münster, 2021.

[89] David Nečas and Petr Klapetek. "Gwyddion: an open-source software for SPM data analysis". In: *Central European Journal of Physics* 10 (1 2012), pp. 181–188. ISSN: 1895-1082. DOI: 10.2478/s11534-011-0096-2. URL: http://gwyddion.net/ (visited on 06/15/2023).

[90] Eric Weisstein. *Affine Transformation*. URL: https://mathworld.wolfram.com/AffineTransformation.html (visited on 12/15/2023).

[91] Günter Gottstein. *Materialwissenschaft und Werkstofftechnik: Physikalische Grundlagen*. 4. Auflage. Springer Vieweg, 2014, p. 171.

[92] *COMSOL Multiphysics® v. 6.0.* www.comsol.com. COMSOL AB, Stockholm, Sweden.

[93] Steve Plimpton. "Fast parallel algorithms for short-range molecular dynamics". In: *Journal of computational physics* 117.1 (1995), pp. 1–19.

[94] Francis H Davies et al. "What governs the atomic structure of the interface between 2D transition metal dichalcogenides in lateral heterostructures?" In: *2D Materials* 11.1 (2024), p. 015003.

[95] Alexander Stukowski. "Visualization and analysis of atomistic simulation data with OVITO–the Open Visualization Tool". In: *Modelling and simulation in materials science and engineering* 18.1 (2009), p. 015012.

[96] Signe G Sørensen et al. "Structure and electronic properties of in situ synthesized single-layer MoS_2 on a gold surface". In: *ACS nano* 8.7 (2014), pp. 6788–6796.

[97] Daniela Dombrowski et al. "Two phases of monolayer tantalum sulfide on Au (111)". In: *ACS nano* 15.8 (2021), pp. 13516–13525.

[98] Charlotte E Sanders et al. "Crystalline and electronic structure of single-layer TaS_2". In: *arXiv preprint arXiv:1606.05856* (2016).

[99] Ming-Yang Li et al. "Heterostructures based on two-dimensional layered materials and their potential applications". In: *Materials Today* 19.6 (2016), pp. 322–335.

[100] Hao-Wei Guo et al. "Stacking of 2D materials". In: *Advanced Functional Materials* 31.4 (2021), p. 2007810.

[101] Shixuan Wang et al. "Stacking-engineered heterostructures in transition metal dichalcogenides". In: *Advanced Materials* 33.16 (2021), p. 2005735.

[102] Removal of TaS_2, MoS_2 tags. URL: **https://creativecommons.org/licenses/by/4.0/** (visited on 03/19/2026).

[103] MV Bollinger et al. "One-dimensional metallic edge states in MoS_2". In: *Physical review letters* 87.19 (2001), p. 196803.

[104] Jeppe Vang Lauritsen et al. "Chemistry of one-dimensional metallic edge states in MoS_2 nanoclusters". In: *Nanotechnology* 14.3 (2003), p. 385.

[105] Iaroslav Lutsyk et al. "Influence of structural defects on charge density waves in 1T-TaS_2". In: *Nano Research* 16.8 (2023), pp. 11528–11539.

[106] Image as is. URL: **https://creativecommons.org/licenses/by/4.0/** (visited on 03/19/2026).

[107] Table design changed. URL: **https://creativecommons.org/licenses/by/4.0/** (visited on 03/19/2026).

[108] Jichen Dong et al. "Edge reconstruction-dependent growth kinetics of MoS2". In: *ACS nano* 17.1 (2022), pp. 127–136.

[109] Nils Krane, Christian Lotze, and Katharina J Franke. "Moiré structure of MoS_2 on Au (111): Local structural and electronic properties". In: *Surface Science* 678 (2018), pp. 136–142.

[110] Jane Hvolbæk Nielsen et al. "Combined spectroscopy and microscopy of supported MoS_2 nanoparticles". In: *Surface science* 603.9 (2009), pp. 1182–1189.

[111] Jeppe Vang Lauritsen. "Atomic-scale study of a hydrodesulfurization model catalyst". In: *PhD degree Thesis, Department of Physics and Astronomy, University of Aarhus* 5 (2002), pp. 47–57.

[112] Image labels adjusted. URL: **https://creativecommons.org/licenses/by/4.0/** (visited on 03/19/2026).

[113] Alpha T N'Diaye et al. "Structure of epitaxial graphene on Ir (111)". In: *New Journal of Physics* 10.4 (2008), p. 043033.

[114] Martin H Müser, Sergey V Sukhomlinov, and Lars Pastewka. "Interatomic potentials: Achievements and challenges". In: *Advances in Physics: X* 8.1 (2023), p. 2093129.

[115] KT Jacob, Shubhra Raj, and L Rannesh. "Vegard's law: a fundamental relation or an approximation?" In: *International Journal of Materials Research* 98.9 (2007), pp. 776–779.

[116] Peter Remmert, Edmund Fischer, and Hans-Ulrich Hummel. "Phasenuntersuchungen im System 2 Ha–TaS_2–2Hc–MoS_2 / Investigations on Phases in the System 2 Ha-TaS_2-2Hc-MoS_2". In: *Zeitschrift für Naturforschung B* 49.9 (1994), pp. 1175–1178.

[117] Image as is. URL: `https://creativecommons.org/licenses/by-nc-nd/3.0/` (visited on 03/19/2026).

[118] Shanshan Wang et al. "Detailed atomic reconstruction of extended line defects in monolayer MoS_2". In: *ACS nano* 10.5 (2016), pp. 5419–5430.

[119] Qu Chen et al. "Ultralong 1D vacancy channels for rapid atomic migration during 2D void formation in monolayer MoS_2". In: *ACS nano* 12.8 (2018), pp. 7721–7730.

[120] Kai Mehlich et al. "Kirkendall Voids in Monolayer $Mo_xTa_yS_2$ Alloys on Au(111)". In: *The Journal of Physical Chemistry Letters* (2025).

[121] Wouter Jolie et al. "Tomonaga-Luttinger liquid in a box: electrons confined within MoS_2 mirror-twin boundaries". In: *Physical Review X* 9.1 (2019), p. 011055.

[122] Günter Gottstein. "Materialwissenschaft und Werkstofftechnik: Physikalische Grundlagen". In: 4. Auflage. Springer Vieweg, 2014, p. 135.

[123] Christian Ratsch and Matthias Scheffler. "Density-functional theory calculations of hopping rates of surface diffusion". In: *Physical Review B* 58.19 (1998), p. 13163.

[124] S Shahab Naghavi, Vinay I Hegde, and C Wolverton. "Diffusion coefficients of transition metals in fcc cobalt". In: *Acta Materialia* 132 (2017), pp. 467–478.

[125] Hannu-Pekka Komsa and Arkady V Krasheninnikov. "Native defects in bulk and monolayer MoS_2 from first principles". In: *Physical Review B* 91.12 (2015), p. 125304.

[126] Mamoru Mekata. "Kagome: The story of the basketweave lattice". In: *Physics Today* 56.2 (2003), pp. 12–13.

[127] JV Lauritsen et al. "Atomic-scale insight into structure and morphology changes of MoS_2 nanoclusters in hydrotreating catalysts". In: *Journal of Catalysis* 221.2 (2004), pp. 510–522.

[128] Maciej Dendzik et al. "Growth and electronic structure of epitaxial single-layer WS_2 on Au (111)". In: *Physical Review B* 92.24 (2015), p. 245442.

[129] Qi Zhang et al. “Doping-Modulated Semiconductor-to-Metal Transformation in a Low-Band-Gap Two-Dimensional Material”. In: *ACS nano* (2026).

[130] A Chaves et al. “Bandgap engineering of two-dimensional semiconductor materials”. In: *npj 2D Materials and Applications* 4.1 (2020), p. 29.

CHAPTER 8

AKNOWLEDGEMENTS

Beginning this section I would like to thank my parents Monika and Andreas for giving me the opportunity to study physics and supporting me on this long journey of study and discovery. It has been a pleasure. In addition to this, I would like to thank the following people and apologize for tending to turn to lightheartedness in doing so:

- **Prof. Dr. Carsten Busse** for supervising this thesis, always having time and an open ear for discussions of its topics, and a lot of patience while I finished writing the dissertation itself;
- **Prof. Dr. Thomas Michely** for accepting to be second supervisor of this thesis;
- **Dr. Arkady Krasheninnikov, Dr. Mahdi Ghorbani-Asl, Dr. Francis Davies** for the nice collaborations and theoretical parts in our shared publications;
- **Dr. Daniel Sahm** for the nice collaboration on the simulation of CLHs with Comsol and our shared publication;
- **Dr. Robin Ohmann** for being a nice colleague and great cooperation on planning the students courses;
- **Dr. Daniela Dombrowski** for teaching me TUMA III and being amazing to work with and be around;
- **Dr. Jiaqi Cai** for always being helpful from Münster to Siegen (and even once Cologne!);
- **Dr. Paul*i*us Aleksa** for being the best Paul*i*us, awesome to hang out with, and generally being a very pleasant person to be around;

- **Dr. Thaís Chagas Peixoto Silva** for being a great person and beating me in chess;
- **Dr. Madad Abbasli** for being a nice colleague;
- **Dennis Rybakowski** for being a nice colleague, his technical support, renting me home in his house, and liking the best video games and music;
- **Christine Zizka** for all the organizational help in handing in this dissertation;
- **Kerstin Semma** for the organizational help during my years in Siegen;
- **Daniel Weber** for his help in the lab and being an overall great student to work with;
- **Dina Wilks** for proofreading this thesis, being a very pleasant person to be around and reminding everyone to go on regular mental-health (Starbucks) trips;
- **Alice Bremerich** for being a pleasant colleague and valuing the right flavor of the Kirmes-Candy. Also: What is up with those books you read??;
- **Catherine Grover** for being loud. And, of course, for proofreading this thesis and being a very pleasant and helpful colleague. I believe you will do great in your future;
- **Stefan Schürrer** a writer way more prolific than I could ever be, whose ability to focus on writing in good and bad times motivated me to also finish my writing;
- **Toni Lange** for proofreading this thesis and, in opposition to me, actually knowing math;
- **Dr. Arne Behrens** also for proofreading this thesis, and always having *fundamental questions*;
- **Dr. Eric (or was it Kai?) Görlitzer, Dr. Pascal Büttner** and all the other dorks (with the exception of my "arch-nemesis" of whom I would never speak badly) who reminded me *regularly* to finally finish this project ;) ;
- **Matthias Thimm** for proofreading this thesis and overall awesomeness from day one in Münster "Lok'tar Ogar!";

- **Bernd Scharlau** whose well designed physics lessons motivated and prepared me in equal measure to study physics;
- **Alexander Löbker** for an email so legendary, it makes me think about this particular physics lesson to this day;
- **Mettie** for trying to teach me how hyphens work in english;
- **Philipp, Johanna and Gustav Jackisch** for being the best throughout all those years and Philipp for travelling to the North Sea with me to start writing this dissertation;
- **Lotte Mehlich** for being tiny and cute. I hope you grow up to be a great scientist or whatever you then wish to be;
- **Die Gummibärenbande** for always being there. You will always be close to my heart, no matter how many miles apart. Also: ヘンネにキスを送ります.

Additionally, I want to thank my grandparents Rita and Michael, my brother Tim, my sister-in-law Vivien, and my whole family. I want to thank the other members from AG Busse, the members of the dissertation committee, my new colleagues at Carl Zeiss SMT, and all those people I surely forgot in this long list.

And, as a very important last thing, a special thanks to my D&D group for understanding that I could not play while I finished this dissertation.
AELIN SMASH!!!